COol Companions ON Ultrawide orbiTS (COCONUTS). I. A high-gravity T4 benchmark around an Old White Dwarf and a re-examination of the surface-gravity dependence of the L/T transition

The Astrophysical Journal, 891:171 (32pp), 2020 March 10 https://doi.org/10.3847/1538-4357/ab765c

COol Companions ON Ultrawide orbiTS (COCONUTS). I. A High-gravity T4 Benchmark around an Old White Dwarf and a Re-examination of the Surface-gravity Dependence of the L/T Transition

Zhoujian Zhang (张周健)[1,5], Michael C. Liu[1], J. J. Hermes[2], Eugene A. Magnier[1], Mark S. Marley[3], Pier-Emmanuel Tremblay[4], Michael A. Tucker[1], Aaron Do[1], Anna V. Payne[1], and Benjamin J. Shappee[1]
[1] Institute for Astronomy, University of Hawaii at Manoa, Honolulu, HI 96822, USA
[2] Department of Astronomy, Boston University, Boston, MA 02215, USA
[3] NASA Ames Research Center, Mail Stop 245-3, Moffett Field, CA 94035, USA
[4] Department of Physics, University of Warwick, Coventry CV4 7AL, UK
Received 2019 September 27; revised 2020 February 9; accepted 2020 February 11; published 2020 March 17

Abstract

We present the first discovery from the COol Companions ON Ultrawide orbiTS (COCONUTS) program, a large-scale survey for wide-orbit planetary and substellar companions. We have discovered a comoving system COCONUTS-1, composed of a hydrogen-dominated white dwarf (PSO J058.9855+45.4184; $d = 31.5$ pc) and a T4 companion (PSO J058.9869+45.4296) at a 40.″6 (1280 au) projected separation. We derive physical properties for COCONUTS-1B from (1) its near-infrared spectrum using cloudless Sonora atmospheric models, and (2) its luminosity and the white dwarf's age ($7.3^{+2.8}_{-1.6}$ Gyr) using Sonora evolutionary models. The two methods give consistent temperatures and radii, but atmospheric models infer a lower surface gravity and therefore an unphysically young age. Assuming evolutionary model parameters ($T_{\rm eff} = 1255^{+6}_{-8}$ K, $\log g = 5.44^{+0.02}_{-0.03}$ dex, $R = 0.789^{+0.011}_{-0.005}\ R_{\rm Jup}$), we find that cloudless model atmospheres have brighter Y- and J-band fluxes than the data, suggesting that condensate clouds have not fully dispersed around 1300 K. The $W2$ flux (4.6 μm) of COCONUTS-1B is fainter than models, suggesting non-equilibrium mixing of CO. To investigate the gravity dependence of the L/T transition, we compile all 60 known L6−T6 benchmarks and derive a homogeneous set of temperatures, surface gravities, and masses. As is well known, young, low-gravity late-L dwarfs have significantly fainter, redder near-infrared photometry and ≈200–300 K cooler temperatures than old, high-gravity objects. Our sample now reveals such gravity dependence becomes weaker for T dwarfs, with young objects having comparable near-infrared photometry and ≈100 K cooler temperatures compared to old objects. Finally, we find that young objects have a larger amplitude J-band brightening than old objects, and also brighten at H band as they cross the L/T transition.

Unified Astronomy Thesaurus concepts: White dwarf stars (1799); Brown dwarfs (185); Substellar companion stars (1648)

Supporting material: data behind figures

1. Introduction

Over the past decade, direct imaging has invigorated the field of extrasolar planetary systems by revealing a population of giant planets and brown dwarf companions with orbital distances beyond ∼10 au (e.g., Bowler 2016). Among this population, companions on ultrawide orbits (≳500 au) are especially appealing, as they can be very well characterized. Compared to closer companions, for which spectroscopic follow up is complicated by the contaminating light of the primary star (e.g., 51 Eri b; Samland et al. 2017), wide-orbit companions can, in principle, have their physical properties robustly estimated via direct spectroscopic analysis, with the assistance of atmospheric models (e.g., Morley et al. 2012; Allard 2014). Compared to free-floating objects in the field, whose luminosities, ages, and masses are degenerate and, thus, cannot be determined without independent age or mass measurements (e.g., Dupuy & Liu 2017), wide-orbit companions can have their physical properties established using the evolutionary models (e.g., Saumon & Marley 2008) thanks to ages from their primary stars.

Wide-orbit companions are therefore valuable benchmarks (e.g., Pinfield et al. 2006; Saumon et al. 2006; Liu et al. 2007) to test and improve current models of ultracool atmospheres, which are limited by, e.g., incomplete molecular opacity line lists, assumptions of chemical and radiative-convective equilibria, and patchy and time-evolving clouds (e.g., Marley & Robinson 2015). In addition, novel techniques have been developed for precisely characterizing stars through their interior structures and stellar activity, e.g., asteroseismology (e.g., Chaplin & Miglio 2013) and gyrochronology (e.g., Barnes 2007). Binary systems composed of stellar primaries and ultracool companions can potentially extend these techniques from the relatively well-calibrated stellar regime down to the substellar regime. This would allow us to better understand the evolution of giant planets and brown dwarfs.

Nearly 40 wide-orbit (≳500 au) ultracool companions have been thus far discovered, spanning M6–Y0 spectral types with ages from ≈1 Myr to ≈10 Gyr (see summary in Deacon et al. 2014). However, we lack knowledge of this sample's completeness, given that some were found as by-products from large-area searches for field brown dwarfs (e.g., GJ 570D;

[5] Visiting Astronomer at the Infrared Telescope Facility, which is operated by the University of Hawaii under contract NNH14CK55B with the National Aeronautics and Space Administration.

Burgasser et al. 2000) and some were found from companion searches that focused only on young moving groups (e.g., GU Psc b; Naud et al. 2014). A few dedicated large-scale searches for ultracool companions have been conducted (e.g., Pinfield et al. 2006; Deacon et al. 2014), but their primary star samples were heterogeneous (e.g., not volume-limited) and they relied on 2MASS (Skrutskie et al. 2006), whose sensitivity has now been greatly surpassed by Pan-STARRS1 (PS1; Chambers et al. 2016), the UKIDSS surveys including UKIDSS Hemisphere Survey (UHS; Dye et al. 2018), Large Area Survey (LAS), Galactic Clusters Survey (GCS), and Galactic Plane Survey (GPS; Lawrence et al. 2007), and AllWISE (Wright et al. 2010; Cutri et al. 2014).

To create a larger and more complete catalog of wide-orbit ultracool benchmarks, we are carrying out the COol Companions ON Ultrawide orbiTS (COCONUTS) program. We are targeting a volume-limited sample of primary stars ($\approx 3 \times 10^5$ objects) with reliable distances within 100 pc, selected from *Gaia* DR2 (Gaia Collaboration et al. 2016, 2018) and the extended *Hipparcos* catalog (Anderson & Francis 2012). Using photometry and astrometry from *Gaia* DR2, PS1, 2MASS, UKIDSS, and AllWISE, we are searching for ultracool companions ($\approx$5–70 $M_{\rm Jup}$) with separations beyond $\approx$500 au. Though the occurrence rate of wide-orbit substellar companions (separation >500 au and mass 5–70 $M_{\rm Jup}$) could be as low as $\approx$0.1% (as extrapolated from the Brandt et al. 2014 companion distribution spanning orbital separations of 10–100 au and masses of 5–70 $M_{\rm Jup}$), our target star sample should be large enough to yield many benchmarks. Also, as done for companions on closer orbits (e.g., 10–100 au; Brandt et al. 2014; Nielsen et al. 2019), a well-defined sample of wide-orbit companions from our survey will establish the companion distributions beyond 500 au, which can shed light on the outer architecture of extrasolar planetary systems.

Here, we present the first discovery from COCONUTS: a high-gravity mid-T companion to a white dwarf. We describe the identification of the system in Section 2 and the spectroscopic follow up in Section 3. We then analyze the physical properties of each system component in Sections 4 and 5. In Section 6, we extend our analysis from this high-gravity T4 benchmark to all 60 known L6-T6 benchmarks in order to better understand the gravity dependence of the L/T transition. We provide a brief summary in Section 7.

2. Identifying the Comoving White Dwarf + T Dwarf Pair

We queried the PS1 Processing Version 3 database using the Desktop Virtual Observatory (Magnier & Cuillandre 2004; Magnier et al. 2016) for objects within a projected separation of 10^4 au around each primary star in the COCONUTS sample, and then cross-matched with *Gaia* DR2, 2MASS, UKIDSS, and AllWISE to obtain the objects' multiwavelength photometry and multi-epoch astrometry. We then apply color and magnitude cuts based on the photometry of ultracool dwarfs from Best et al. (2018) and identify comoving candidates if their proper motions are consistent with their primary stars. Finally, we remove previously known objects by cross-matching our candidate list with SIMBAD[6] and existing catalogs of ultracool dwarfs (e.g., Deacon et al. 2014; Best et al. 2018) and remove extended sources and detector artifacts by visually checking PS1 images.

[6] http://simbad.u-strasbg.fr/simbad/

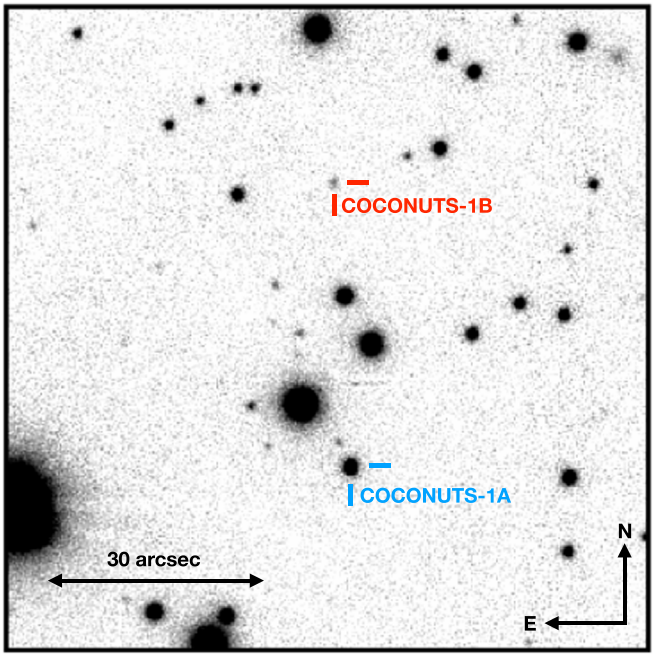

Figure 1. The white dwarf primary COCONUTS-1A and the T dwarf companion COCONUTS-1B in the Pan-STARRS1 $y_{\rm P1}$-band image (size of 90″ on each side). The two objects are separated by 40.″61 ± 0.″04, which corresponds to 1280 ± 4 au at the primary's distance.

The above process yielded our first discovery COCONUTS-1, a T dwarf companion PSO J058.9869+45.4296 to a white dwarf PSO J058.9855+45.4184. We hereafter note the primary star as COCONUTS-1A and the companion as COCONUTS-1B. The *Gaia* DR2 astrometric solutions of the primary are reliable given that they are derived from 14 independent *Gaia* observations (i.e., visibility_periods_used = 14), and are consistent with the *Gaia*'s single-star model given that its renormalized unit weight error (RUWE = 1.05) is smaller than 1.4 (as suggested by Lindegren 2018). The primary has a distance of 31.51 ± 0.09 pc, derived from its *Gaia* DR2 astrometry in a Bayesian fashion by Bailer-Jones et al. (2018). In addition, we note the primary is a white dwarf, primarily based on its *Gaia* DR2 photometry (*G*-band absolute magnitude of 14.681 ± 0.007 mag and $G_{\rm BP} - G_{\rm RP}$ = 1.085 ± 0.010 mag) and its optical and near-infrared spectra (Section 3.1). The A and B components have an angular separation of 40.″61 ± 0.″04 from their PS1 coordinates, which is then converted into a projected physical separation of 1280 ± 4 au given the primary star's distance. We show the system in Figure 1 and summarize its astrophysical properties in Table 1.

The companion's colors and absolute magnitudes (assuming the white dwarf's *Gaia* DR2 distance) are consistent with a mid-T dwarf located at the distance of the white dwarf (Figure 2). In addition, the PS1 proper motion[7] of the companion, $(\mu_\alpha \cos\delta,\ \mu_\delta) = (28.2 \pm 31.5, -266.2 \pm 31.4)$ mas yr^{-1}, is consistent with the primary, which also shows a significant southward motion of (21.9 ± 2.5, −265.2 ± 1.2) mas yr^{-1} based on PS1 and (19.1 ± 0.2, −263.2 ± 0.1) mas yr^{-1} based on *Gaia* DR2. Their common proper motions are vastly different from the motions of the other stars in the neighborhood (Figure 3), validating the association between the primary and the companion.

[7] Magnier et al. (2016) computed the positions, parallaxes, and proper motions of PS1 objects using iteratively re-weighted least-squares fitting with outlier clipping, and then tied the objects' astrometry to *Gaia* DR1.

Table 1
Properties of COCONUTS-1

Properties	COCONUTS-1A	COCONUTS-1B
Spectral Type	DA	T4 ± 0.5
Age (Gyr)	$7.3^{+2.8}_{-1.6}$	···
Gaia DR2 Astrometry		
Designation	*Gaia* DR2 2442147996896919 04	···
Coordinates (α, δ; hms, dms)	03:55:56.53, +45:25:06.2	···
visibility_periods_used	14	···
astrometric excess noise (mas)	0.12 (0.35σ)	···
Renormalised Unit Weight Error	1.05	···
Proper Motions ($\mu_\alpha \cos\delta$, μ_δ; mas yr^{-1})	19.1 ± 0.2, −263.2 ± 0.1	···
Parallax (mas)	31.71 ± 0.09	···
Distance (pc)	31.51 ± 0.09	31 ± 3[a]
Tangential Velocity (km s^{-1})	39.45 ± 0.11	···
PS1 Astrometry		
Designation	PSO J058.9855+45.4184	PSO J058.9869 +45.4296
Coordinates (α, δ; hms, dms)	03:55:56.53, +45:25:06.4	03:55:56.87, +45:25:46.8
Proper Motions ($\mu_\alpha \cos\delta$, μ_δ; mas yr^{-1})	21.9 ± 2.5, −265.2 ± 1.2	28.2 ± 31.5, −266.2 ± 31.4
Tangential Velocity (km s^{-1})[b]	39.78 ± 0.22	40.01 ± 4.70
Position Angle (East of North; deg)	···	5.13 ± 0.04
Angular Separation (arcsec)	40.61 ± 0.04	
Physical Separation (au)	1280 ± 4	
Photometry		
G (mag)	17.1756 ± 0.0011	···
Absolute G (mag)	14.681 ± 0.007	···
G_{BP} (mag)	17.650 ± 0.009	···
G_{RP} (mag)	16.565 ± 0.005	···
$G_{BP} - G_{RP}$ (mag)	1.085 ± 0.010	···
g_{P1} (AB mag)	17.705 ± 0.006	···
r_{P1} (AB mag)	17.133 ± 0.003	···
i_{P1} (AB mag)	16.904 ± 0.005	···
z_{P1} (AB mag)	16.826 ± 0.004	21.196 ± 0.090
y_{P1} (AB mag)	16.778 ± 0.010	19.471 ± 0.043
J_{MKO} (mag)	15.924 ± 0.010	16.733 ± 0.018
H_{MKO} (mag)	15.645 ± 0.013[c]	16.618 ± 0.020[c]
K_{MKO} (mag)	15.520 ± 0.015[c]	16.578 ± 0.022[c]
J_{2MASS} (mag)	16.053 ± 0.102	···
H_{2MASS} (mag)	15.730 ± 0.164	···
K_{2MASS} (mag)	>15.625[d]	···
$W1$ (mag)	···	16.466 ± 0.074
$W2$ (mag)	···	15.427 ± 0.105
$W3$ (mag)	···	>12.183[c]
$W4$ (mag)	···	>8.719[c]

Notes.
[a] The spectrophotometric distance of the companion.
[b] The PS1 tangential velocities are computed using the white dwarf's *Gaia* DR2 distance and uncertainties.
[c] The H_{MKO} and K_{MKO} photometry of COCONUTS-1AB are synthesized using J_{MKO} from their near-infrared spectra. We do not use these photometry to (1) conduct the SED analysis of COCONUTS-1A (Section 4), and (2) flux-calibrate the near-infrared spectrum of COCONUTS-1B for the atmospheric model analysis (Section 5.3).
[d] The K_{2MASS} magnitude of COCONUTS-1A and the $W3$ and $W4$ magnitudes of COCONUTS-1B are 95% upper limits.

3. Observations

3.1. Spectroscopy of the Primary: UH 2.2 m/SNIFS and IRTF/SpeX

We obtained an optical spectrum of the white dwarf primary COCONUTS-1A using the SuperNova Integral Field Spectrograph (SNIFS; Aldering et al. 2002; Lantz et al. 2004) mounted on the University of Hawaii 2.2 m telescope on Maunakea. SNIFS is a $6'' \times 6''$ Integral Field Unit (IFU) with a moderate spectral resolution of $R \approx 1200$, providing simultaneous coverage from 3300 to 9700 Å. Our observations were conducted on two consecutive nights (2018 December 11–12 UT), with total exposure times of 2700 s and 1800 s, respectively. The SNIFS data reduction followed the pipeline as described in Bacon et al. (2001), which extracted the object's one-dimensional (1D) spectrum incorporated with dark, bias, and flat-field corrections, wavelength calibration, and sky subtraction. The dispersion in wavelength calibration is ≈0.38 Å for wavelength <4700 Å and ≈2.11 Å for wavelength >5300 Å. We flux-calibrated the 1D spectrum from each night using spectrophotometric standard stars observed in the same night (GD 71 and GD 153 for December 11; Feige 34 and HD 93521 for December 12). We combined both nights with a weighted average. The reduced SNIFS spectrum is in air wavelength and has signal-to-noise ratio (S/N) ≈ 20 per pixel at 6000 Å.

We also obtained a near-infrared spectrum of COCONUTS-1A using the NASA Infrared Telescope Facility (IRTF) on 2018 October 23 UT with clear skies and ≈0.″9 seeing. We used the facility spectrograph SpeX (Rayner et al. 2003) in prism mode with the $0.''8 \times 15''$ slit ($R \approx 50$–160) and the wavelength coverage of 0.7–2.52 μm and took 10 exposures with 60 s each in a standard ABBA pattern. We observed the A0V standard star HD 23452 within 20 minutes and 0.05 airmass of the primary star for telluric correction. We reduced the data using version 4.1 of the Spextool software package (Cushing et al. 2004). The reduced SpeX spectrum is in vacuum wavelength and has S/N ≈ 40 per pixel in J band.

3.2. Spectroscopy of the Companion: IRTF/SpeX

The companion COCONUTS-1B was observed using IRTF/SpeX in prism mode on 2018 October 22 (UT), with clear skies and ≈0.″8 seeing. We used the $0.''8 \times 15''$ slit and took 18 exposures with 120 s each in a standard ABBA pattern. The A0 V standard star HD 21038 was observed within 1 hr and 0.1 airmass of the companion. The dispersion in wavelength calibration of the prism data is 5.9 Å (M. Cushing, private communication). The reduced SpeX spectrum is in vacuum wavelength and has S/N ≈ 40 per pixel in J band.

4. The White Dwarf Primary

We present the spectrum of the white dwarf primary in Figure 4. The white dwarf is mostly featureless except for the Hα line, suggesting COCONUTS-1A is a hydrogen-dominated (DA) white dwarf. The UH 2.2 m/SNIFS spectrum has a relatively low S/N of ≈10 at ⩽4800 Å, lacks strong Balmer lines, and has a wavelength gap at 4800–5300 Å. We therefore do not derive physical properties from a spectroscopic analysis (e.g., Bergeron et al. 1992, 1995; Liebert et al. 2005). As a robust alternative (e.g., Bédard et al. 2017; Hollands et al. 2018), we conduct a photometric analysis by fitting its spectral energy distribution (SED) from optical to near-infrared wavelengths (e.g., Bergeron et al. 1997; Giammichele et al. 2012). We have only used the observed spectrum to confirm our SED-based model fits.

We follow Bergeron et al. (1997) to perform our SED analysis (also see Gentile Fusillo et al. 2019). We first construct the SED of the white dwarf using photometry from *Gaia* DR2,

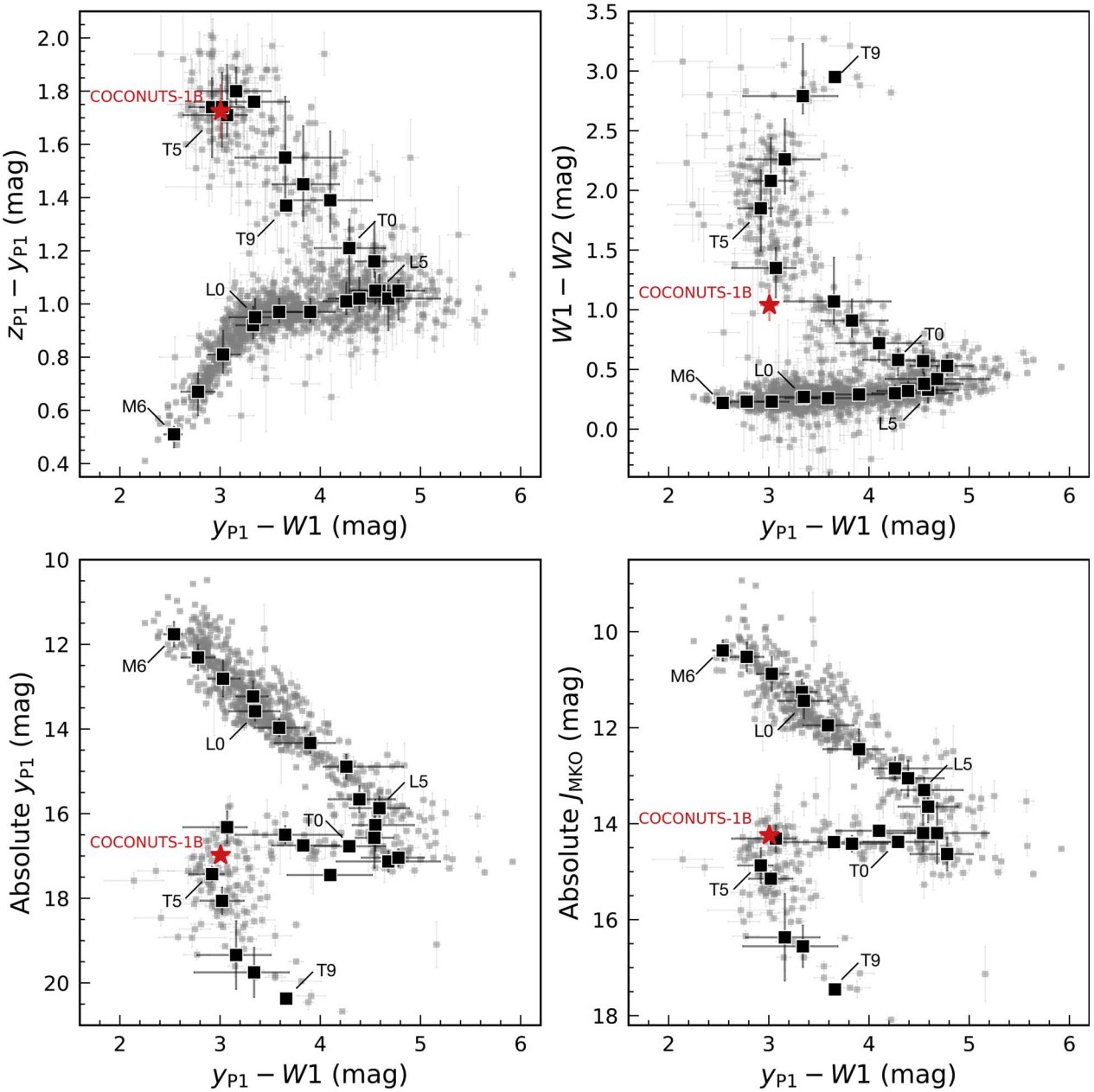

Figure 2. Color–color/magnitude diagrams for the companion COCONUTS-1B (red). We use gray squares to show known field M6–T9 dwarfs from Best et al. (2018) and W.M.J. Best et al. (2020, in preparation), which have infrared absolute magnitudes with S/N > 5 and are not young, binaries, or subdwarfs. We use black squares and black error bars to show the typical photometry and 1σ confidence limits of these field dwarfs in each spectral type bin. The y_{P1} and J_{MKO} absolute magnitudes of COCONUTS-1B are computed by assuming its primary star's *Gaia* DR2 parallax. The companion's colors and magnitudes both suggest a mid-T dwarf located at the distance of the white dwarf primary.

PS1, and the UKIDSS Hemisphere Survey (Table 1), and convert magnitudes into fluxes using zero-point fluxes from Evans et al. (2018), Tonry et al. (2012), and Lawrence et al. (2007), respectively. We do not include 2MASS photometry, whose uncertainties are too large to constrain models. We assume reddening is negligible given the system's distance (31.51 pc). We then fit the white dwarf's SED using hydrogen-dominated atmospheric models from Tremblay et al. (2011), which span 1.5×10^3–1.4×10^5 K in effective temperature $T_{\rm eff}$ and 6.0–10.0 dex in logarithmic surface gravity $\log g$. For a given choice of $\{T_{\rm eff}, \log g\}$, we obtain a model spectrum by linearly interpolating the Tremblay et al. (2011) models and then synthesize photometry by convolving this model spectrum with the corresponding filter response curves,[8] scaled by the *Gaia* DR2 distance and white dwarf radius (i.e., Equations (2)–(3) of Bergeron et al. 1997). The radius is not a free parameter but rather is derived from the $\{T_{\rm eff}, \log g\}$ values using the Fontaine et al. (2001) evolutionary sequences, which assume C/O-cores (where carbon and oxygen are mixed uniformly with equal mass) and thick hydrogen layers (where the hydrogen envelope constitutes 10^{-4} of the total white dwarf mass).

[8] The filter response in the J_{MKO} band from the UKIDSS Hemisphere Survey is provided by Hewett et al. (2006), and the filters of the other bands are from the same aforementioned references that provide the zero-point fluxes.

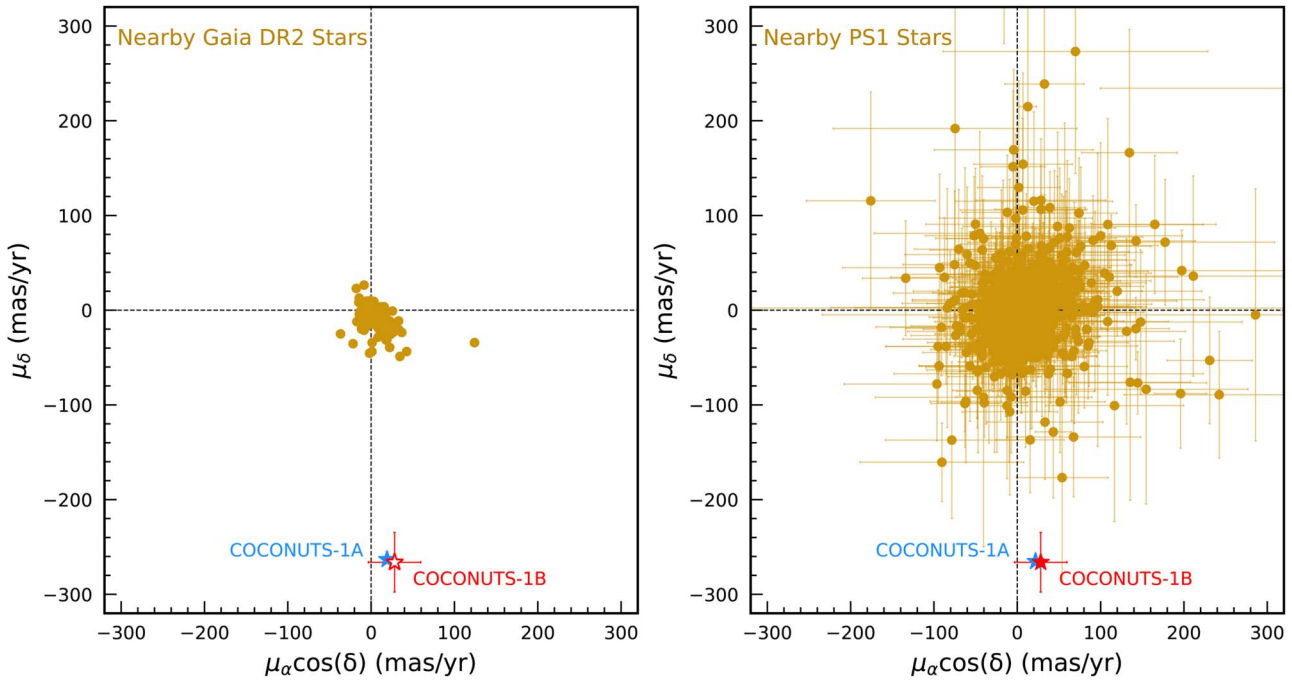

Figure 3. Left panel: *Gaia* DR2 proper motions of the primary star (blue) and stars within a radius of 10′ (brown), compared with the PS1 proper motion of the companion (since it has no *Gaia* DR2 detection) shown as a red open symbol. The nearby *Gaia* DR2 stars are all background with parallaxes smaller than the primary by at least 14 mas. Right panel: PS1 proper motions of the primary, the companion, and stars within a radius of 10′. These two diagrams validate the association between the primary and the companion, as they both have significant southward motion as opposed to the other stars in the field.

We derive $\{T_{\rm eff}, \log g\}$ and uncertainties using the nonlinear least-squares method (Press et al. 1992), where the χ^2 values are computed by summing the difference between observed and synthetic fluxes in all bands, weighted by errors that incorporate the parallax and magnitude uncertainties. Finally, we obtain $T_{\rm eff} = 5115 \pm 61$ K and $\log\ g = 7.945 \pm 0.038$. Here, we adopt external uncertainties of 1.2% on effective temperature and 0.038 dex on surface gravity, as derived from the spectroscopic analysis by Liebert et al. (2005), to account for the underestimated error budget of physical parameters. We present our best-fit model spectra in Figure 5. The agreement between the model and the observed Hα line confirms the almost pure-hydrogen atmosphere interpretation.

Using the SED-derived $\{T_{\rm eff}, \log g\}$ and uncertainties, we interpolate the Fontaine et al. (2001) isochrones and obtain a white dwarf mass as $0.548 \pm 0.023\ M_\odot$. These models suggest the star has been cooling as a white dwarf for 4.6 ± 0.6 Gyr. While we do not attempt a correction, we note that cool white dwarfs ($T_{\rm eff} \lesssim 6000$ K) appear over-luminous compared to astrophysical expectations (cooling at constant mass), leading to an underestimated mass by ≈5% (e.g., Hollands et al. 2018; Bergeron et al. 2019; Blouin et al. 2019).

We derive the mass of the zero-age-main-sequence white dwarf progenitor to be $1.54 \pm 0.20\ M_\odot$ using a mean of three cluster-calibrated initial-to-final mass relations (IFMRs; Kalirai et al. 2008; Casewell et al. 2009; Williams et al. 2009). Using the MIST isochrones (Choi et al. 2016), we can convert this progenitor mass into a main-sequence lifetime of $2.7^{+1.4}_{-0.8}$ Gyr. Unfortunately, IFMRs are poorly calibrated for low-mass ($<0.6\ M_\odot$) white dwarfs. However, theoretical IFMRs also do not accurately match higher-mass stars, which could be related to the adopted efficiency of convective overshoot (e.g., Salaris et al. 2009; Fields et al. 2016). Without detailed calibrations for the theoretical IFMRs, we adopt our progenitor mass from the empirical, cluster-calibrated IFMRs.

Combining the cooling age of the white dwarf and the main-sequence lifetime of its progenitor, we derive a total age of the white dwarf to be $7.3^{+2.8}_{-1.6}$ Gyr. Here, the age uncertainties are doubled from those of the white dwarf progenitor's main-sequence lifetime in order to account for errors from the white dwarf's cooling age and the IFMR systematics. We assume the T dwarf companion and white dwarf are coeval, given that the A and B components of the system are comoving and associated (Section 2).

5. The T Dwarf Companion

5.1. Spectral Type

We calculate the spectral type for the companion using the Burgasser (2007) polynomial fits for the five spectral indices defined by Burgasser et al. (2006a), which trace CH_4 and H_2O absorption in ultracool atmospheres. We obtain spectral types of T3.9 from its H_2O-J index of 0.377, T1.3 from its CH_4-J index of 0.604, T4.0 from its H_2O-H index of 0.417, T4.3 from its CH_4-H index of 0.534, and T4.7 from its CH_4-K index of 0.248. The final index-based spectral type is T3.6 ± 1.4, computed as the average and the standard deviation over all five indices.

We also compare the companion's spectrum with T-type spectral standards (Burgasser et al. 2006a) (Figure 6). As suggested by Liu et al. (2010), we use SDSS J1206+2813 as the T3 spectral standard, given that both the original Burgasser et al. (2006a) standard 2MASS J12091004 (T2.0+T7.5; Liu et al. 2010) and the alternative Burgasser et al. (2006a) standard SDSS J10210304AB (T1+T5; Burgasser et al. 2006b) are binaries. We derive a visual spectral type of T4 with an

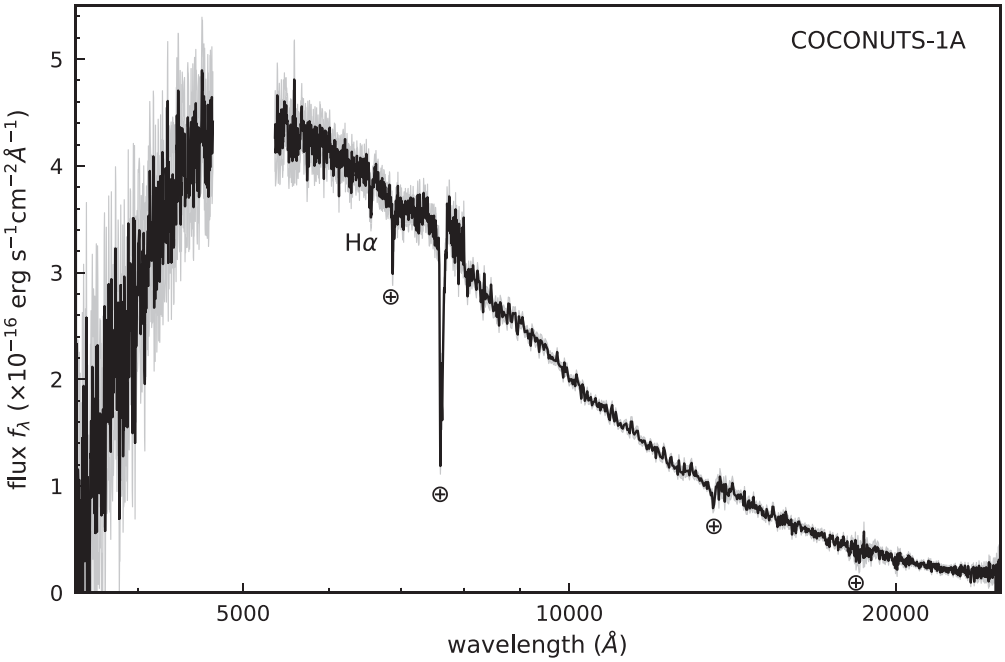

Figure 4. The flux-calibrated UH 2.2 m/SNIFS and IRTF/SpeX spectra of the white dwarf primary COCONUTS-1A. Flux uncertainties are shown as the gray shadow, and prominent telluric absorption features are noted by "⊕." Here, we convert the wavelength of the white dwarf's SpeX spectrum from vacuum to air based on Ciddor (1996) to match the wavelength of the SNIFS spectrum, as well as the Tremblay et al. (2011) model spectrum shown in Figure 5. The white dwarf is mostly featureless except for the Hα line, suggesting COCONUTS-1A is hydrogen-dominated (DA).

(The data used to create this figure are available.)

uncertainty of 0.5 subtype. We notice that the companion's spectrum around the *Y*-band peak is relatively suppressed compared to the T4 spectral standard.

Both the index-based and visual spectral types are consistent with the companion's colors and absolute magnitudes (Figure 2), and we adopt the visual type of T4 ± 0.5 as the final spectral type. In addition, we find the companion is unlikely an unresolved binary based on criteria suggested by Burgasser et al. (2010).

5.2. Companionship Assessment

We use the observed space density of ultracool dwarfs to estimate the probability that our T dwarf discovery is a field interloper not bound to the white dwarf. Precise estimates of the space densities of L/T transition (≈L6−T6) objects have been difficult because of their short-lived nature in this evolutionary stage (e.g., Day-Jones et al. 2013; Marocco et al. 2015). Recently, Best (2018) have compiled a volume-limited sample of L0-T8 field dwarfs within 25 pc and derived precise space densities. We adopt their results for T4 dwarfs of $(4.5 \pm 1.1) \times 10^{-4}$ pc^{-3}.

We then derive the spectrophotometric distance of COCONUTS-1B by comparing its observed photometry in $z_{\rm P1}$, $y_{\rm P1}$, $J_{\rm MKO}$, *W*1, and *W*2 bands, to the absolute magnitudes of T3−T5 field dwarfs (excluding binaries, subdwarfs, and young objects) from the Best et al. (2018) catalog. We obtain typical absolute magnitudes of $M_{z_{\rm P1}} = 18.7 \pm 0.3$ mag, $M_{y_{\rm P1}} = 17.0 \pm 0.4$ mag, $M_{J_{\rm MKO}} = 14.4 \pm 0.4$ mag, $M_{W1} = 14.0 \pm 0.6$ mag, and $M_{W2} = 12.5 \pm 0.3$ mag using 13, 14, 23, 21, and 21 field dwarfs, respectively. We thereby derive spectrophotometric distances of $d_{z_{\rm P1}} = 32 \pm 5$ pc, $d_{y_{\rm P1}} = 31 \pm 6$ pc, $d_{J_{\rm MKO}} = 29 \pm 5$ pc, $d_{W1} = 31 \pm 8$ pc, and $d_{W2} = 39 \pm 6$ pc. We note spectrophotometric distances from all bands except for *W*2[9] are consistent with the *Gaia* DR2 distance 31.51 ± 0.09 pc of the white dwarf, again supporting the common distance between the T dwarf and the white dwarf. We adopt a spectrophotometric distance of 31 ± 3 pc by averaging all of the bands except *W*2 with the uncertainties propagated.

We use the aforementioned space density to compute the expected number of the T4-type field interloper in a volume approximated as a circular region with a generous radius of 10^4 au (Section 2) and a depth of 6 pc (i.e., two times the uncertainty of the companion's photometric distance), leading to $(2.6 \pm 0.6) \times 10^{-6}$ objects. Considering that our T dwarf discovery also has a common proper motion with the white dwarf (Figure 3), the contamination probability will be even lower. Thus, we conclude that the white dwarf and the T dwarf form a physical pair.

5.3. Atmospheric Model Analysis

5.3.1. Model Atmospheres

We model the near-infrared spectrum of COCONUTS-1B using the cloudless Sonora grids (Marley et al. 2017; M. Marley et al. 2019, in preparation). The models are generated over 0.4–50 μm in wavelength assuming chemical equilibrium, a helium abundance of $Y = 0.28$, and a solar carbon-to-oxygen ratio. The model grids span 200–2400 K in effective temperature ($T_{\rm eff}$; with spacing of 25 K in 200–600 K, 50 K in 600–1000 K, and 100 K in 1000–2400 K) and 3.25–5.5 dex

[9] The relatively farther photometric distance from *W*2 may be intriguing. Using the white dwarf's distance, the T dwarf's *W*2-band absolute magnitude is 12.93 ± 0.11 mag, which, compared with the typical M_{W2} value, suggests that its emergent flux around ≈4.6 μm is fainter than other T3–T5 dwarfs by a factor of 1.5 ± 0.4 (or equivalently fainter by 0.4 ± 0.3 mag).

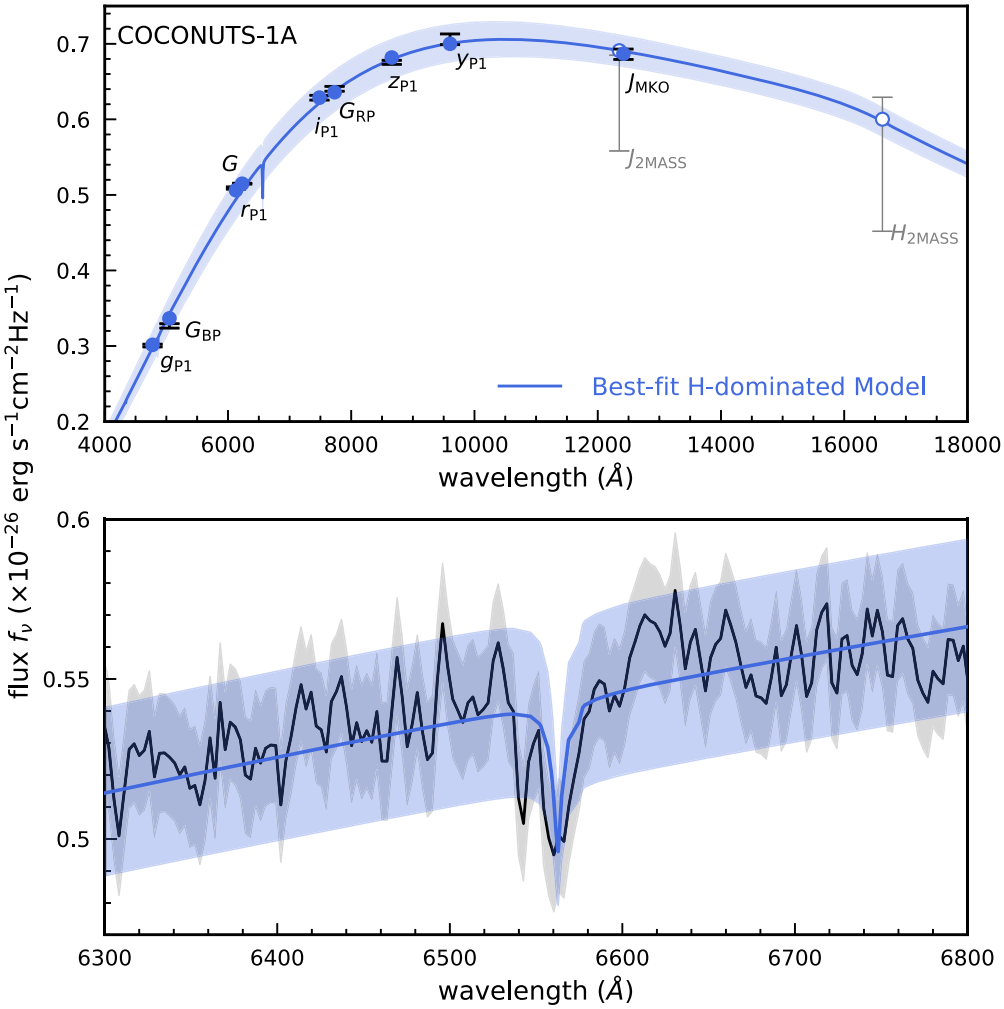

Figure 5. The upper panel presents the best-fit hydrogen-dominated model spectrum (blue line) with 1σ model uncertainties (computed from the parameter errors; blue shadow) for the SED of the white dwarf primary COCONUTS-1A. The observed fluxes and uncertainties from *Gaia* DR2, PS1, UHS, and 2MASS are shown as error bars, and the 2MASS photometry are plotted in gray since they are not included in our SED analysis (Section 4). The synthesized broadband fluxes using the best-fit model spectrum are consistent with observations and are shown as blue circles (solid circles for *Gaia* DR2, PS1, and UHS, and open circles for 2MASS). The lower panel compares the best-fit model spectrum (blue) with the flux-calibrated UH 2.2 m/SNIFS spectrum (black) and flux uncertainties (gray shadow) near the Hα line. The model spectrum is convolved at the SNIFS resolution. We note a possible spectral feature around 6540 Å, but a higher S/N is needed to assess the reality of this feature. The agreement between the SED-derived model and the observed Hα line confirms the hydrogen-dominated atmosphere of COCONUTS-1A.

in logarithmic surface gravity (log g; cgs units; with spacing of 0.25 dex). The grids include three metallicities (Z): sub-solar (-0.5 dex), solar (0 dex), and super-solar ($+0.5$ dex).

Are cloudless models suitable for our companion? While clouds play a crucial role shaping the emergent spectra of ultracool dwarfs, they become less significant as brown dwarfs evolve through the L/T transition to cooler temperatures ($T_{\rm eff} \lesssim 1400$ K; e.g., Kirkpatrick 2005; Saumon & Marley 2008; Marley et al. 2010). This process results in clearer atmospheres at the near-infrared wavelengths. Therefore, the early- to mid-T dwarfs, such as our T4 companion discovery, have relatively brighter J-band emission and bluer $J-K$ colors than earlier-type L/T transition objects (e.g., Dupuy & Liu 2012, also see Figures 2 and 14). We can test the influence of clouds by comparing our available set of models to COCONUTS-1B. If its observed spectrum significantly deviates from the model atmospheres or implies unphysical properties for an object given the age of its white dwarf primary, then we can gain insights about cloud formation in ultracool atmospheres during the mid-T evolutionary stage.

5.3.2. Forward Modeling

We fit our SpeX spectrum using the Sonora model grids over 0.9–2.3 μm in wavelength, where the companion's spectrum has S/N $\gtrsim 5$ per pixel. We convolve each model spectrum with the instrumental profile corresponding to the SpeX prism with the 0.″8 slit (Rayner et al. 2003), including the wavelength-dependent spectral resolution in the convolution process (using scripts of the Starfish package by Czekala et al. 2015). The convolved model spectra therefore match the spectral resolution of the observed data. We also incorporate the radial velocity v_r, the projected rotational velocity $v \sin i$, and the solid angle $\Omega = (R/d)^2$, where R is the object's radius and d is distance, into the model spectra when comparing with data.

We then flux-calibrate the observed spectrum by using the companion's J-band magnitude from the UKIDSS Hemisphere Survey, which provides the only observed near-infrared photometry for this object. We use the WFCAM J-band filter from Hewett et al. (2006) and obtain the zero-point flux from Lawrence et al. (2007).

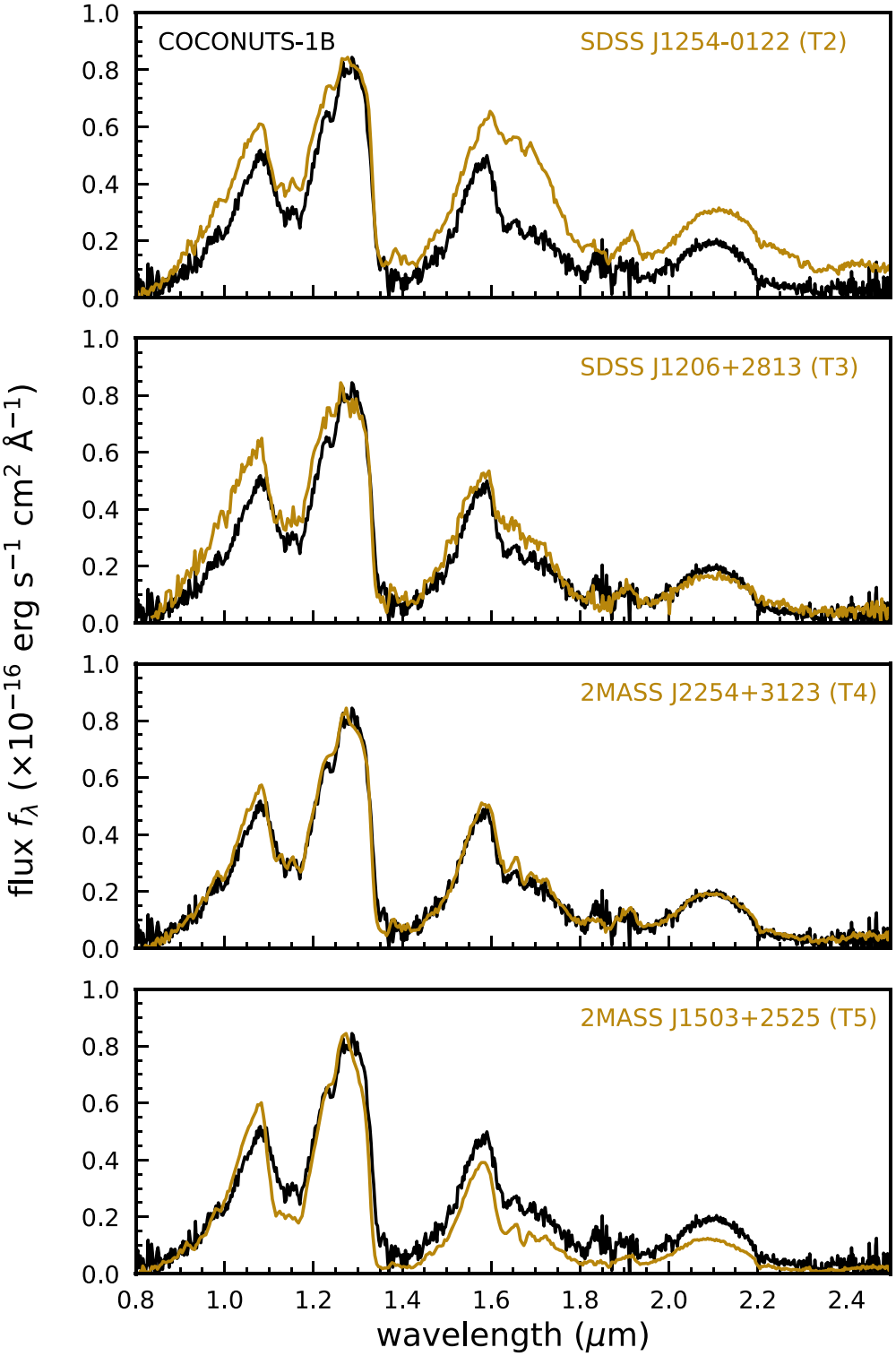

Figure 6. The IRTF/SpeX near-infrared spectra of the companion COCONUTS-1B (black), as well as the T2–T5 spectral standards (brown; Burgasser et al. 2006a; Liu et al. 2010). The spectrum of COCONUTS-1B is flux-calibrated using its $J_{\rm MKO}$ magnitude from UHS (Section 5.3.2), and the other spectral standards are normalized by their peak fluxes. We thereby derive a visual type of T4 $\pm$ 0.5 for COCONUTS-1B, although its *Y*-band emission is relatively suppressed compared to the T4 standard.

(The data used to create this figure are available.)

We then use the Markov chain Monte Carlo (MCMC) algorithm *emcee* (Foreman-Mackey et al. 2013) with 24 walkers to determine the posteriors for the six physical parameters $\{T_{\rm eff}, \log g, Z, v_r, v \sin i, \log \Omega\}$. We use linear interpolation to construct model spectra with $\{T_{\rm eff}, \log g, Z\}$ between the Sonora grid points, with the interpolation

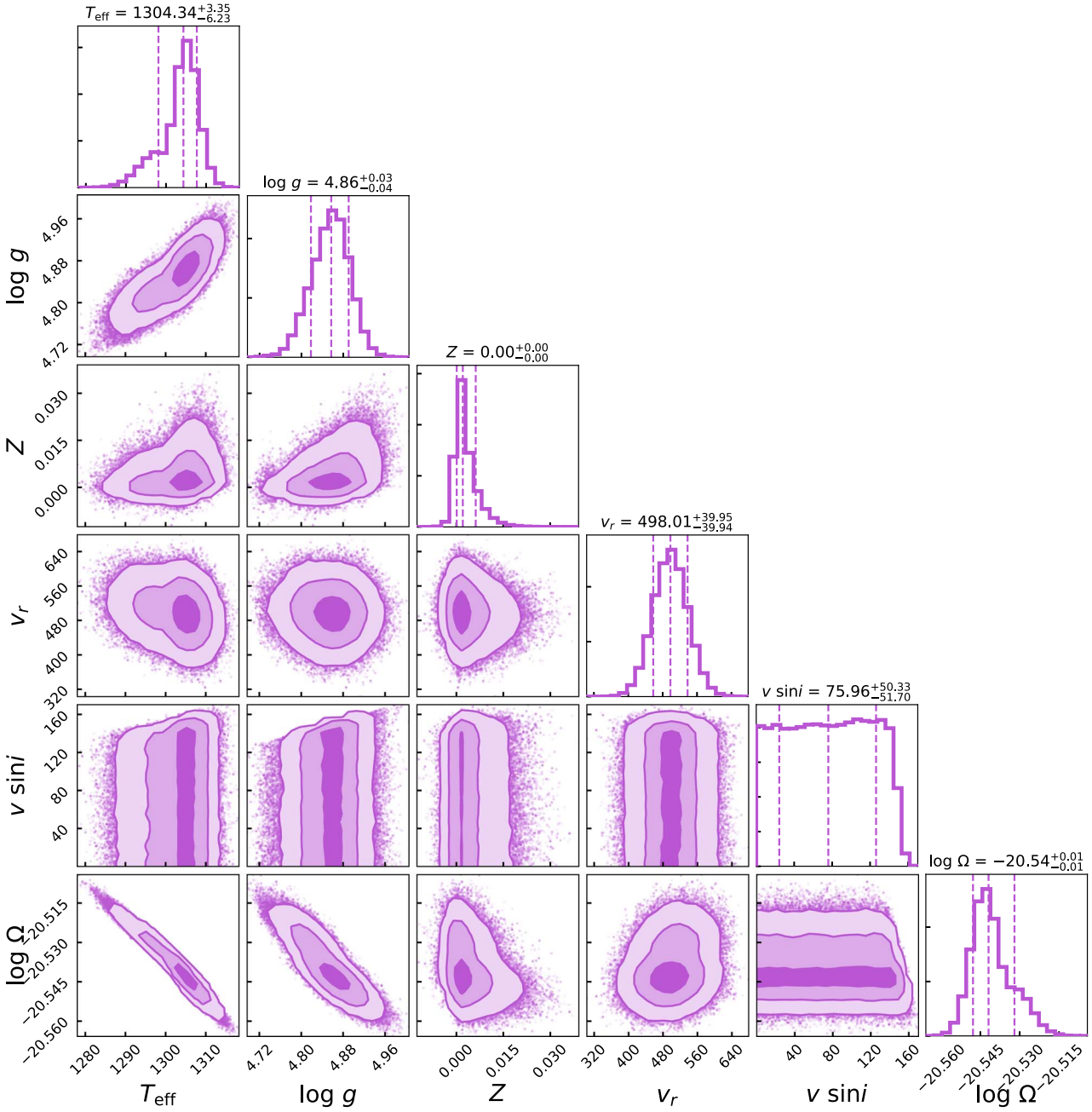

Figure 7. Posterior distributions of COCONUTS-1B properties derived using the Sonora atmospheric models. The physical parameters plotted are effective temperature ($T_{\rm eff}$; in units of K), logarithmic surface gravity (log g), metallicity (Z), radial velocity (v_r; in units of km s^{-1}), projected rotational velocity (v sin i; in units of km s^{-1}), and the logarithmic solid angle log Ω.

conducted in logarithmic units for $T_{\rm eff}$. To evaluate model parameters, we construct the covariance matrix by placing the squared measurement uncertainties along the diagonal axis.

We assume uniform priors for $T_{\rm eff}$ between 200 K and 2400 K, log g between 3.25 and 5.5, Z between −0.5 and +0.5, and v sin i between 0 and $v_{\rm max}$. The maximum rotational velocity $v_{\rm max}$ is determined based on the object's oblateness, expressed as $f = 2Cv_{\rm rot}^2/3gd\sqrt{\Omega}$ (Barnes & Fortney 2003; Marley & Sengupta 2011), where $v_{\rm rot}$ is the equatorial rotational velocity, d is the *Gaia* DR2 distance of the white dwarf primary, and $C = 0.9669$ (Chandrasekhar 1939) corresponds to the $n = 1.5$ polytropic index, which well approximates fully convective brown dwarfs (e.g., Burrows & Liebert 1993). Requiring the object's oblateness to be below the stability limit for the $n = 1.5$ polytope, i.e., $f \leqslant 0.385 \equiv f_{\rm crit}$ (James 1964), we therefore derive the following constraints on $v_{\rm rot}$ and v sin i:

$$0 \leqslant v \sin i \leqslant v_{\rm rot} \leqslant \Omega^{1/4}\left(\frac{3f_{\rm crit}\, gd}{2C}\right)^{1/2} \equiv v_{\rm max}. \quad (1)$$

For each step of each *emcee* walker, we thus compute $v_{\rm max}$ and assume a uniform prior between 0 and $v_{\rm max}$ for the projected rotational velocity v sin i. In addition, we assume uniform priors for both v_r and log Ω between $-\infty$ and $+\infty$.

Table 2
Model-derived Physical Properties of COCONUTS-1B

Properties	Atmospheric Models[a]	Evolutionary Models
Bolometric Luminosity ($\log(L_{\rm bol}/L_\odot)$)	...	-4.832 ± 0.007
Effective Temperature ($T_{\rm eff}$; K)	1304^{+3}_{-6} (± 50)	1255^{+6}_{-8}
Logarithmic Surface Gravity ($\log g$; cgs)	$4.86^{+0.03}_{-0.04}$ (± 0.13)	$5.44^{+0.02}_{-0.03}$
Metallicity (Z)	$0.002^{+0.004}_{-0.002}$ (± 0.250)	0
Radial Velocity (v_r; km s^{-1})	498^{+40}_{-40} (± 200)	...
Projected Rotational Velocity ($v \sin i$; km s^{-1})	76^{+50}_{-52}	...
Logarithmic Solid Angle ($\log \Omega$)	$-20.542^{+0.010}_{-0.006}$ (± 0.067)	$-20.474^{+0.013}_{-0.006}$
Radius (R; $R_{\rm Jup}$)	$0.730^{+0.009}_{-0.006}$ (± 0.056)	$0.789^{+0.011}_{-0.005}$
Mass (M; $M_{\rm Jup}$)	$15.4^{+0.9}_{-0.8}$ (± 5.2)	$69.3^{+1.6}_{-3.4}$

Note.
[a] Values inside parentheses are the final adopted uncertainties as discussed in Section 5.3.3.

5.3.3. Results

We present the posteriors of the six physical parameters in Figure 7, with results summarized in Table 2. Using the *Gaia* DR2 distance 31.51 ± 0.09 pc of the white dwarf primary, we convert the best-fit $\log \Omega = -20.542^{+0.010}_{-0.006}$ dex into the companion's radius of $R = 0.730^{+0.009}_{-0.006}$ $R_{\rm Jup}$. We further use $\log g$ and R and compute the companion's mass as $M = 15.4^{+0.9}_{-0.8}$ $M_{\rm Jup}$. Neither the radius nor the mass are plausible, which we discuss in Section 5.5.

We test the convergence of the resulting MCMC chains based on their integrated autocorrelation time, following the *emcee* documentation.[10] As we increase the number of iterations, we estimate the average autocorrelation time for each physical parameter based on the Goodman & Weare (2010) method and the revised version suggested by Daniel Foreman-Mackey.[11] The chains are supposed to converge once their lengths exceed 50 times the average autocorrelation time. As shown in Figure 8, all of our chains have converged after 2.5×10^4 iterations. We run the fitting process with 6×10^4 iterations and use the second half of the chains to produce parameter posteriors.

Figure 9 compares the observed data with Sonora model spectra interpolated at physical parameters drawn from the MCMC chains. While the model spectra match the overall observed spectral morphology, the residuals in several wavelength ranges are much larger than the measurement uncertainties. At the blue wing of the Y band (<1 μm), the models over-predict the emergent flux. The flux in this region is a sensitive function of both the potassium abundance and the pressure-broadened red wing of the potassium doublet at 0.77 μm (e.g., Tsuji et al. 1999; Burrows & Volobuyev 2003; Allard et al. 2007a). In addition, the models over-predict the emergent flux around the J-band peak while under-predicting the H-band peak. The excess J-band flux from models likely arises from the lack of a deep cloud deck in these models, which would attenuate the flux emerging from the deep atmosphere. The underpredicted H-band flux from models could well be a consequence of the fitting procedure responding to the overestimate of the J-band flux by choosing models that under-predict the H-band flux.

Our derived physical parameters all have very small uncertainties, likely because model systematics and uncertainties from the linear interpolation of the model grid are not accounted for. Also, the posteriors of $T_{\rm eff}$ and Z are close to the model grid point of $T_{\rm eff} = 1300$ K and $Z = 0$ dex, respectively (Figure 7). This is likely due to the sparsely sampled atmospheric models (the $T_{\rm eff}$ spacing is 100 K and the Z spacing is 0.5 dex), where linear interpolation may bias the posteriors toward model grid points (e.g., Cottaar et al. 2014; Czekala et al. 2015). A more sophisticated analysis is beyond the scope of this paper. Given the artificially small parameter errors, we inflate the uncertainties of $\{T_{\rm eff}, \log g, Z\}$ by adopting halves of the local grid spacing, namely 50 K, 0.13 dex, and 0.25 dex, respectively. These then lead to inflated errors of 0.056 $R_{\rm Jup}$ in radius and 5.2 $M_{\rm Jup}$ in mass (Table 2).

As a result of the fitting process, we note that the companion's radial velocity v_r and projected rotational velocity $v \sin i$ might behave like nuisance parameters aiming for better fitting results rather than preserving their physical meaning, given that the main differences between data and models result from model systematics. We adjust the error of v_r by incorporating the dispersion in wavelength calibration of the prism data (5.9 Å; Section 3.2), which corresponds to a velocity of 200–80 km s^{-1} in the 0.9–2.3 μm wavelength. We thus adopt a v_r uncertainty of 200 km s^{-1}. We keep the uncertainty of $v \sin i$, which has a significance of only 1.5σ from our forward modeling analysis (76^{+52}_{-50} km s^{-1}; Table 2).

5.4. Evolutionary Model Analysis

We also use the hot-start cloudless Sonora evolutionary models with solar metallicity (Marley et al. 2017; M. Marley et al. 2019, in preparation) to derive the companion's $T_{\rm eff}$, $\log g$, and R. These evolutionary-derived parameters can be directly compared to the atmospheric modeling results, as the best-fit metallicity from our atmospheric models is $Z = 0$ (Figure 7). We adapt the method of Saumon et al. (2006) for the evolutionary model analysis. The Saumon et al. (2006) method aims to determine the $\{T_{\rm eff}, \log g\}$ values, where the bolometric luminosity $L_{\rm bol}$ is the same between the one derived using the object's near-infrared spectrum and the atmospheric model-based bolometric correction, and the one derived using evolutionary models. Here, we adapt this method in a Bayesian framework.

We first calculate the companion's near-infrared luminosity $L_{0.9-2.3\,\mu{\rm m}}$ by integrating its flux-calibrated IRTF/SpeX spectrum in 0.9–2.3 μm and using the *Gaia* DR2 distance of the primary, with uncertainties in flux and distance incorporated. We then initiate an MCMC process with free parameters

[10] https://emcee.readthedocs.io/en/latest/tutorials/autocorr/
[11] https://github.com/dfm/emcee/issues/209

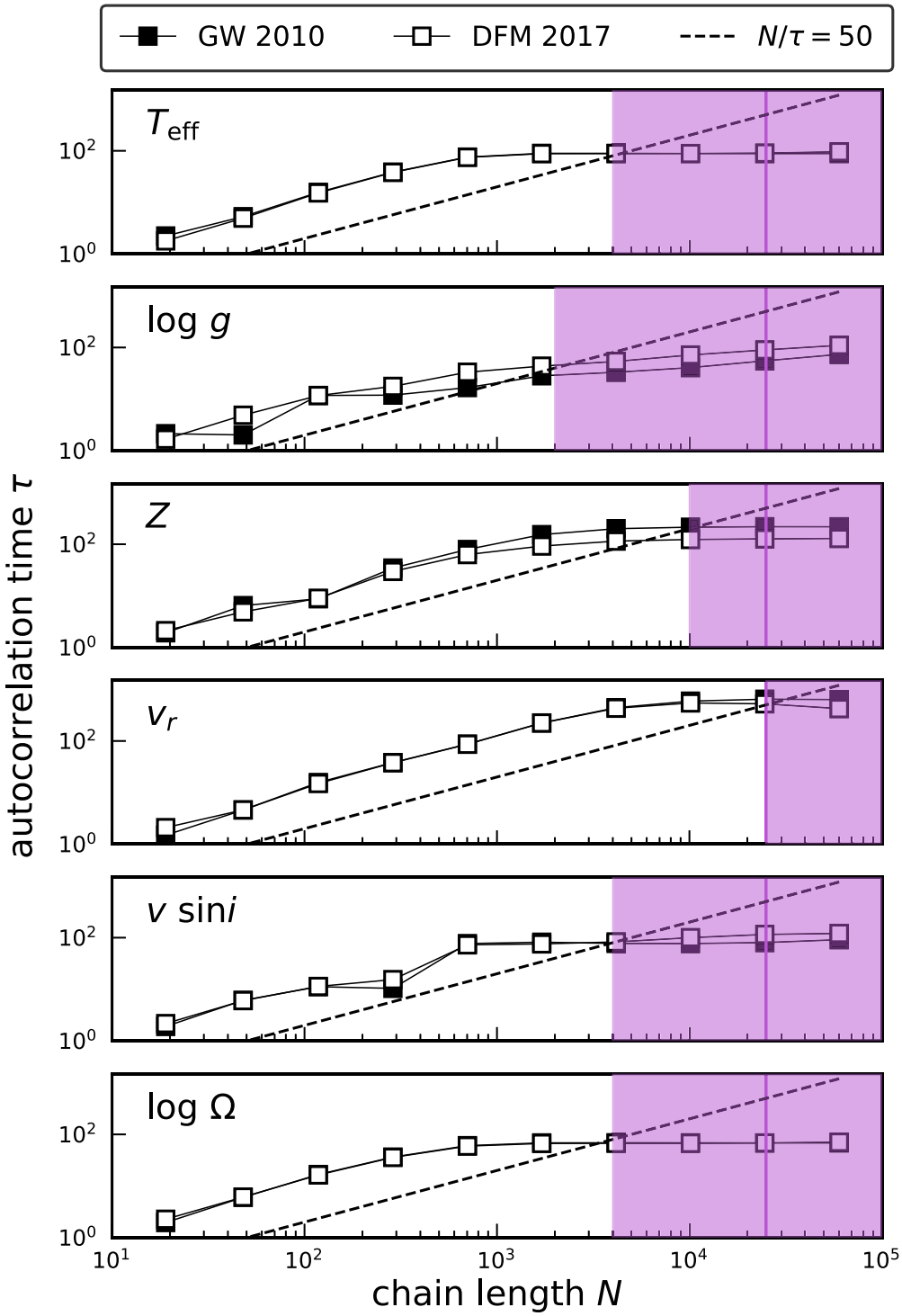

Figure 8. The integrated autocorrelation time for the MCMC chains of each physical parameter from our atmospheric model analysis, computed with different chain lengths based on the Goodman & Weare (2010) method (GW2010; solid squares) and the revised version suggested by Foreman-Mackey (DFM 2017; open squares), both of which produce consistent estimates. As suggested by the *emcee* documentation, the chains are supposed to converge once their lengths exceeds 50 times the estimated autocorrelation time from both (dashed line). While the chains for different parameters require different chain lengths (purple shadows), all of our chains converge after 2.5×10^4 samples (purple vertical lines).

being $T_{\rm eff}$ and $\log g$. For a given choice of $\{T_{\rm eff}, \log g\}$, we construct a model spectrum by linearly interpolating the Sonora atmospheric models. We then use the interpolated model spectrum to compute a bolometric correction, defined as the ratio between its integrated fluxes between 0.9 and 2.3 μm and between 0.4 and 50 μm. We find that this ratio ranges from 0.6 to 0.72 for the cloudless Sonora models of $T_{\rm eff} > 1200$ K, with changes of $\lesssim$0.008 across halves of the grid spacing. We thus assign an uncertainty of 0.01 to the computed flux ratio to account for variations in the model-based bolometric correction. We then apply the ratio to the companion's measured $L_{0.9-2.3\ \mu{\rm m}}$ to derive its atmospheric-based bolometric luminosity $L_{\rm bol,atm}$, with uncertainties propagated from $L_{0.9-2.3\ \mu{\rm m}}$ and the bolometric correction.

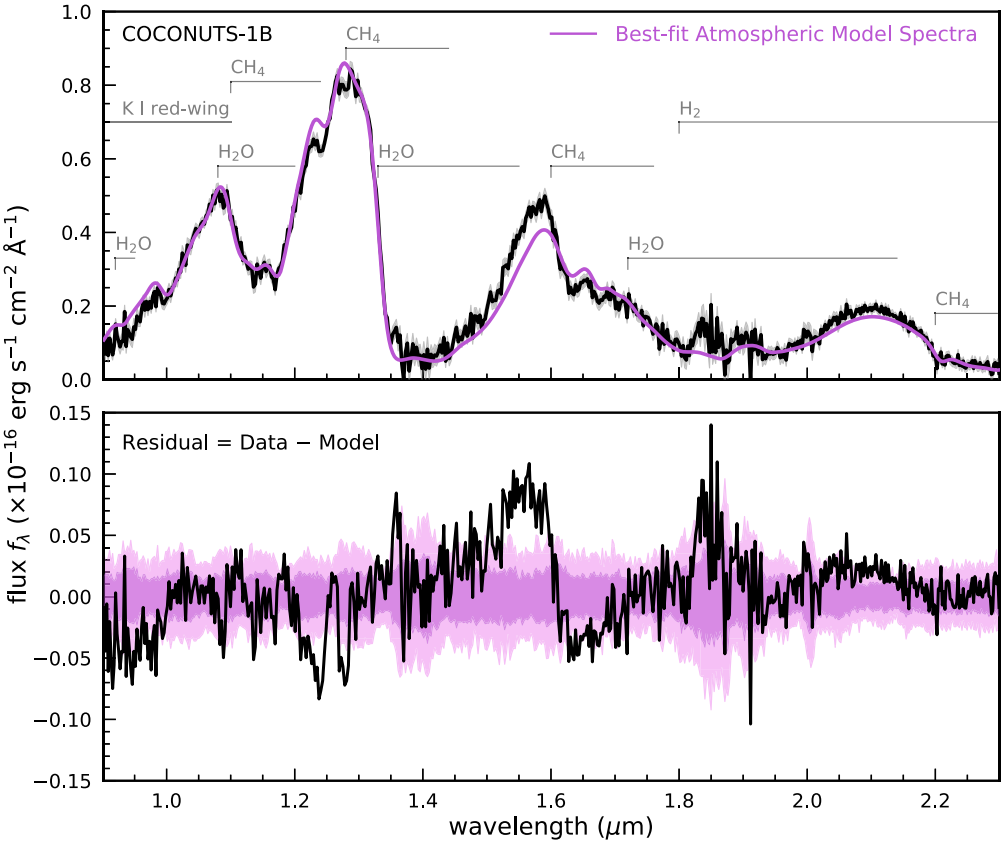

Figure 9. The upper panel presents the observed spectra of COCONUTS-1B (black) with 1σ measurement uncertainties (gray shadow) and the Sonora atmospheric model spectra interpolated at the parameters drawn from the MCMC chains (purple). The lower panel shows the fitting residual (data–model; black), and the purple shadows are the 1σ and 2σ dispersions of 50,000 random draws from the covariance matrix, composed of measurement uncertainties along the diagonal axis.

In addition, with the same $\{T_{\rm eff}, \log g\}$ values, we interpolate the Sonora evolutionary models, in logarithmic units for $T_{\rm eff}$ and age, to derive the companion's predicted bolometric luminosity $L_{\rm bol,evo}$ and age $t_{\rm evo}$. We evaluate $\{T_{\rm eff}, \log g\}$ using the following likelihood function

$$\mathcal{L} = p(L_{\rm bol,atm} \mid L_{\rm bol,evo}) \times p(t_{\rm WD} \mid t_{\rm evo}) \times p(T_{\rm eff}) \times p(\log g) \quad (2)$$

where $t_{\rm WD} = 7.3^{+2.8}_{-1.6}$ Gyr is the age of the white dwarf primary. To compute $p(L_{\rm bol,atm} \mid L_{\rm bol,evo})$, we assume that the bolometric luminosity follows a normal distribution with mean and standard deviation corresponding to the value and uncertainty of $L_{\rm bol,atm}$, respectively. To compute $p(t_{\rm WD} \mid t_{\rm evo})$, we assume the age follows a distribution composed of two half-Gaussians joined at 7.3 Gyr and extending from 0 to 12 Gyr. We assign standard deviations of 1.6 Gyr and 2.8 Gyr to the Gaussians younger and older than 7.3 Gyr, respectively, to account for asymmetric error bars. Priors of $T_{\rm eff}$ and $\log g$ are assumed to be uniform distributions within the parameter space of the Sonora models, as done in Section 5.3.2. We use *emcee* to execute the above process and derive posteriors of $\{T_{\rm eff}, \log g\}$ as $T_{\rm eff} = 1255^{+6}_{-8}$ K and $\log g = 5.44^{+0.02}_{-0.03}$ dex. We then use the resulting chains of $\{T_{\rm eff}, \log g\}$ with the interpolated Sonora evolutionary models to obtain $\log(L_{\rm bol}/L_\odot) = -4.832 \pm 0.007$, $R = 0.789^{+0.011}_{-0.005}$ $R_{\rm Jup}$, and $M = 69.3^{+1.6}_{-3.4}$ $M_{\rm Jup}$. We present posteriors for the evolutionary model parameters in Figure 10, with the best-fit values summarized in Table 2.

We also try alternative methods to determine the companion's properties, which first calculate the companion's bolometric luminosity $L_{\rm bol}$ from its observed spectrum and then combine it with the white dwarf's age to use the interpolated Sonora evolutionary models. We use two approaches to compute $L_{\rm bol}$. Our first approach directly integrates the best-fit atmospheric model spectra over 0.4–50 μm and uses the *Gaia* DR2 distance of the primary, with parameter uncertainties incorporated. We derive $\log(L_{\rm bol}/L_\odot) = -4.84 \pm 0.03$, which is consistent with our method adapted from Saumon et al. (2006). The relatively larger uncertainty from this approach results from the inflated uncertainties of atmospheric-derived parameters (Section 5.3.3).

Our second approach follows Golimowski et al. (2004), which combines the 0.9–2.3 μm IRTF/SpeX spectrum with the observed broadband fluxes converted from $z_{\rm P1}$, $W1$, and $W2$ magnitudes, using the filter responses and zero-point fluxes from Tonry et al. (2012) and Jarrett et al. (2011). We linearly interpolate fluxes between the spectrum and broadband fluxes. At shorter wavelength, we linearly extrapolate fluxes to zero, and at longer wavelengths, we assume a Rayleigh–Jeans tail longword of $W2$. We integrate the spectrum constructed as above and derive the $L_{\rm bol}$ as $\log(L_{\rm bol}/L_\odot) = -4.901 \pm 0.003$. Compared to our adopted method based on Saumon et al. (2006), the $L_{\rm bol}$ estimated from this approach is a factor of $\approx$1.17 fainter, which is close to the correction factor of 1.2 suggested by Golimowski et al. (2004). Given that the aforementioned extrapolation process is inadequate to account for CH_4 and CO absorption of mid-to-late T dwarfs in the $\approx$3–5 μm range, Golimowski et al. (2004) determined such a correction based on the observed L- and M-band spectra

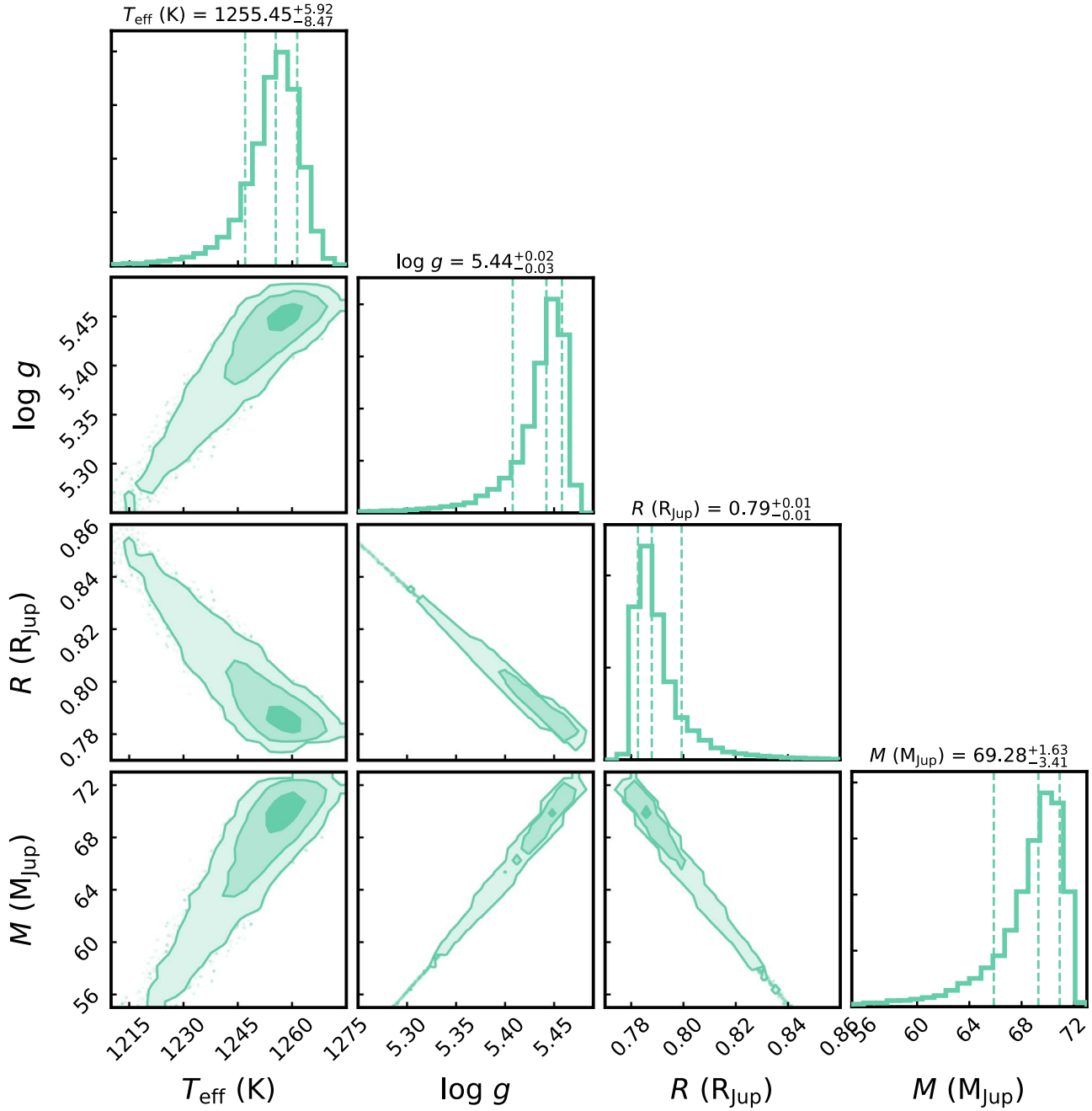

Figure 10. Posterior distributions of COCONUTS-1B properties derived from evolutionary models and the age of the white dwarf primary. The parameters plotted are effective temperature ($T_{\rm eff}$), logarithmic surface gravity (log g), radius (R), and mass (M).

of Gl 229B (T7). In conclusion, both of our alternative approaches can produce consistent $L_{\rm bol}$ and, thereby, evolutionary model parameters, with our adopted method.

5.5. Benchmarking

Having derived the companion's properties using both atmospheric models (Section 5.3) and evolutionary models (Section 5.4), we now compare the physical parameters derived from these two model sets, an approach often referred to as "benchmarking" (e.g., Pinfield et al. 2006; Liu et al. 2008). Figure 11 compares the posteriors of effective temperature, surface gravity, radius, and mass derived from atmospheric models and evolutionary models. The posteriors of the atmospheric-derived parameters are not directly from the MCMC chains of our forward modeling analysis but are rather those derived from inflating the uncertainties to halves of the model grid spacing (Section 5.3). Specifically, we generate Gaussian posteriors for $T_{\rm eff}$ and $\log g$, assuming the mean values are their best-fit values from our atmospheric model analysis, and the standard deviation is 50 K and 0.13 dex, respectively. We then generate the radius R posterior using the new $T_{\rm eff}$ posterior and the $R^2T_{\rm eff}^4$ chain values from the original atmospheric model analysis (i.e., the Stefan–Boltzmann law). We generate the mass M posterior using the $\log g$ and R posteriors. We note that the atmospheric and evolutionary

models predict consistent $T_{\rm eff}$ and R values, with insignificant differences of 49 ± 51 K and 0.06 ± 0.06 $R_{\rm Jup}$, respectively.

However, the log g values are vastly different from the atmospheric and evolutionary models, with the former predicting a lower value by 0.58 ± 0.13 dex, leading to a ≈5× lower mass estimate. Also, based on the Sonora evolutionary models, the $T_{\rm eff}$ and log g of COCONUTS-1B derived from the atmospheric models correspond to an unphysically young age of ≈380 ± 230 Myr, which is in direct contradiction to our age estimate of $7.3^{+2.8}_{-1.6}$ Gyr for the white dwarf[12] (Section 4). We conclude that for COCONUTS-1, the old white dwarf age is more reliable than the much younger age of the brown dwarf companion derived from Sonora atmospheric models, especially since our white dwarf analysis is based on high-S/N photometry and spectroscopy spanning from optical to near-infrared, with systematics in white dwarf model atmospheres and IFMRs carefully incorporated (Section 4). The unphysically young age of the brown dwarf companion based on atmospheric models is likely due to shortcomings of these cloudless models. Therefore, we adopt the Sonora evolutionary model parameters as the characteristics of the brown dwarf companion. We also note that the companion's $\log g = 5.44^{+0.02}_{-0.03}$ dex is among the highest surface gravity that brown dwarfs can reach over cosmic time.

Here, we explore the possible shortcomings of the cloudless Sonora model atmospheres. We interpolate and scale the Sonora atmospheric model spectra using the $\{T_{\rm eff}, \log g, R\}$ values inferred from the evolutionary model analysis and the white dwarf's distance. Then we compare these evolutionary-based model spectra to the best-fit atmospheric model spectra, as well as the observed data. As shown in Figure 12, the evolutionary-based model spectra do not match the observed spectrum, as the former are much bluer and have higher flux in the Y and J bands. In these cloudless models, the flux at Y- and J-band peaks emerges from ≈30 bar where the atmospheric temperature is about 1900 K (with the J band probing a few bars deeper and ≈50 K warmer than the Y band). Most of the large peak flux differences arises because of the great wavelength sensitivity of the Planck function on the Wien tail.

Two different opacity sources could be responsible for the mismatch between the evolutionary-based model spectra and the data. First, silicate clouds condense at somewhat lower temperatures (e.g., Figure 3 of Marley et al. 2013) and, thus, can be expected to limit the depth from which flux emerges, conceptually shaving off the peaks of the Y and J bands (e.g., Morley et al. 2012), which might result in the evolutionary-based model spectra that better match the data. Such a comparison suggests that the silicate clouds still influence the emitted flux at 1300 K, and cloudy models should provide a more accurate interpretation of the observed spectrum.

The second opacity that could play a role in the mismatch is the highly pressure-broadened wings of the K resonance lines at 0.77 μm (Burrows et al. 2000). The Sonora grid uses a line shape theory by Allard et al. (2007b) that is valid to molecular hydrogen densities up to 10^{20} cm^{-3}. These authors have recently developed a newer theory (Allard et al. 2016), superseding their previous work, valid to higher densities. At 30 bar and 1900 K, the molecular hydrogen densities in the atmosphere of our companion are just above the upper limit of the previous Allard et al. (2007b) theory, and the strength of the broadened wing is uncertain, particularly in the Y band.

In Figure 13, we plot both the atmospheric and evolutionary-based model spectra to a wider wavelength range of 0.7–6.0 μm and compare with the companion's broadband photometry. We synthesize broadband fluxes from the models and compute fluxes from the companion's observed $z_{\rm P1}$, $y_{\rm P1}$, $J_{\rm MKO}$, $W1$, and $W2$ magnitudes, using the filter responses and zero-point fluxes from Tonry et al. (2012) for Pan-STARRS1, Hewett et al. (2006) and Lawrence et al. (2007) for UKIDSS Hemisphere Survey, and Jarrett et al. (2011) for *WISE*. We also synthesize the $H_{\rm MKO}$ and $K_{\rm MKO}$ photometry of COCONUTS-1B using $J_{\rm MKO}$ from the observed near-infrared spectrum and compare to the synthesized values from models. We note that the broadband photometry is consistent with the atmospheric model spectra and/or the evolutionary-based model spectra, except for $W2$, where the observed magnitude is much fainter than the model spectra. Such a mismatch around 4.6 μm can be caused by the absorption from CO when it is dredged up from deeper, warmer layers of atmospheres into the photosphere through non-equilibrium mixing (e.g., Marley et al. 2002; Stephens et al. 2009; Zahnle & Marley 2014). Therefore, non-equilibrium models are probably needed to better understand the atmosphere processes of COCONUTS-1B.

6. The Surface-gravity Dependence of the L/T Transition

Spectrophotometric observations of benchmark planets and brown dwarfs have suggested a surface-gravity dependence of the L/T transition. Younger, lower-gravity L/T dwarfs tend to have fainter, redder near-infrared photometry (e.g., Marois et al. 2008; Barman et al. 2011; Faherty et al. 2016; Liu et al. 2016), higher variability amplitudes (e.g., Biller et al. 2015; Gagné et al. 2017; Vos et al. 2019), and cooler effective temperatures (e.g., Metchev & Hillenbrand 2006; Luhman et al. 2007; Dupuy et al. 2009; Bowler et al. 2013; Liu et al. 2013; Gagné et al. 2018) compared to their older, higher-gravity counterparts. Such gravity dependence is significant especially for the transition L dwarfs (L6–L9). Less is known for the transition T dwarfs (T0–T5) due to the small number of such objects with low surface gravities discovered thus far, but it appears that the gravity dependence is less pronounced than for L dwarfs (e.g., Filippazzo et al. 2015; Gagné et al. 2015; Faherty et al. 2016; Liu et al. 2016).

To better understand the role that gravity plays in the L/T transition, a large sample of benchmarks spanning a wide range in surface gravities (or equivalently ages) is essential. Since the most recent large photometric analyses (e.g., Faherty et al. 2016; Liu et al. 2016), the census of planetary and substellar benchmarks has been expanded, as (1) new young moving group members and companions to stars or white dwarfs have been discovered, whose ages can be determined from their host associations or primary stars (e.g., COCONUTS-1 in this work; Bowler et al. 2017; Deacon et al. 2017; Gagné et al. 2017, 2018; Gauza et al. 2019), and (2) more substellar binaries and companions have measured dynamical masses thanks to ongoing astrometric monitoring programs (e.g., Dupuy & Liu 2017; Dupuy et al. 2019). In

[12] Age discrepancies have been previously found in binary systems composed of white dwarfs and main-sequence stars with projected separations ⩽60 au (e.g., Lagrange et al. 2006; Zurlo et al. 2013; Matthews et al. 2014). In these systems, the age of the stellar component, derived from gyrochronology and/or chromospheric activities, is notably younger than that of the white dwarf, derived from its cooling age and the progenitor's main-sequence lifetime. One likely explanation is that the angular momentum lost during white dwarf formation is transferred to the stellar component, causing the star to spin up and thereby appear younger when using rotation-based age-dating techniques (e.g., Jeffries & Stevens 1996; Karovska et al. 1997; Desidera & Barbieri 2007). However, these systems are not analogs of COCONUTS-1, where the white dwarf and the brown dwarf are widely separated (≈1280 au; Section 2) and, therefore, likely have evolved in isolation.

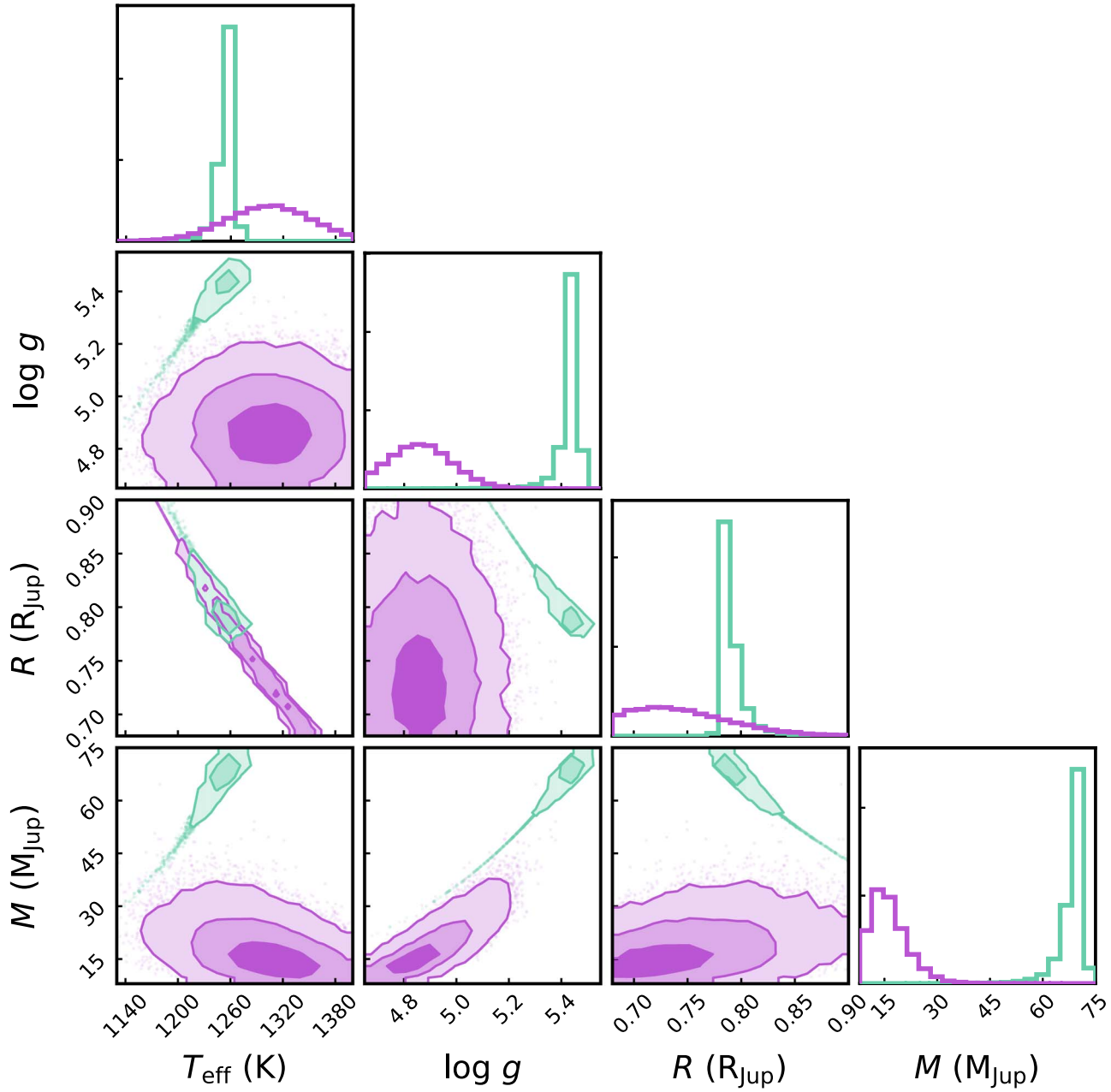

Figure 11. Posterior distributions of the COCONUTS-1B physical properties derived from both atmospheric models (purple) and evolutionary models (green). The physical parameters plotted are effective temperature ($T_{\rm eff}$), logarithmic surface gravity (log g), radius (R), and mass (M). The posteriors of atmospheric-derived parameters are not from the MCMC chains of our forward modeling shown in Figure 7 but are rather re-generated using the adjusted uncertainties as described in Section 5.5. We note that $T_{\rm eff}$ and R derived from the two models are consistent within 50 K and 0.06 $R_{\rm Jup}$, but the atmospheric models produce a much lower log g by ≈0.6 dex and, thus, a ≈5× lower M estimate.

addition, the current census of benchmarks can now have very precise absolute magnitudes and physical properties (e.g., bolometric luminosities and effective temperatures), as a result of the high-precision parallaxes from *Gaia* DR2 (Gaia Collaboration et al. 2016, 2018).

6.1. A Sample of L/T Transition Benchmarks

We have combined COCONUTS-1B with all known L6−T6 planetary and substellar benchmarks (Table 3). Our sample contains 9 free-floating members of stellar associations (nearby young moving groups, the Pleiades, and the Hyades), 38 single/binary companions to stars or white dwarfs, and 8 field substellar binaries, leading to a total of 60 objects in 50 systems. The ages of free-floating objects and companions to stars or white dwarfs in the literature have been determined from their host associations or primary stars (except for WISE J072003.20−084651.2B [WISE 0720B]; Burgasser et al. 2015; Dupuy et al. 2019). The ages of field substellar binaries and WISE 0720B in the literature have been determined from evolutionary models using their measured dynamical masses and bolometric luminosities. In order to investigate the impact of surface gravity on L/T transition properties, we divide our sample into "young" (20 objects) and "old" (40 objects) subsets using a dividing line of 300 Myr. After ∼300 Myr, the radii of

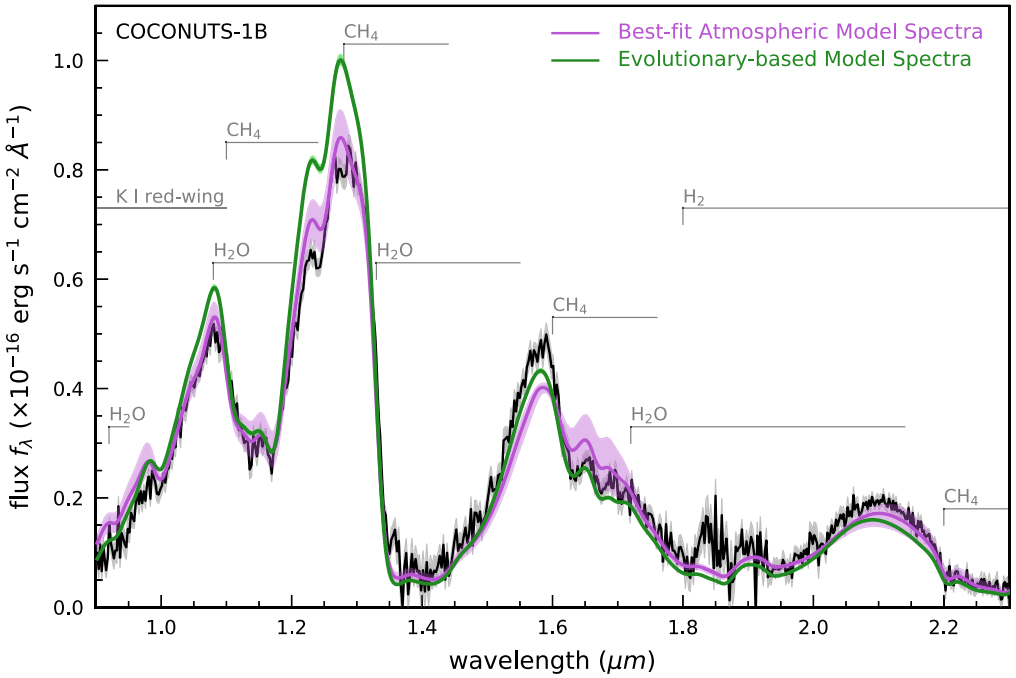

Figure 12. The atmospheric model spectra interpolated at the parameters derived from the evolutionary model analysis of COCONUTS-1B (green) with 1σ uncertainties (green shadows). Overlaid are the observed spectra of COCONUTS-1B (black) and the Sonora atmospheric model spectra interpolated from the posteriors shown in Figure 11, using the same format as in Figure 9.

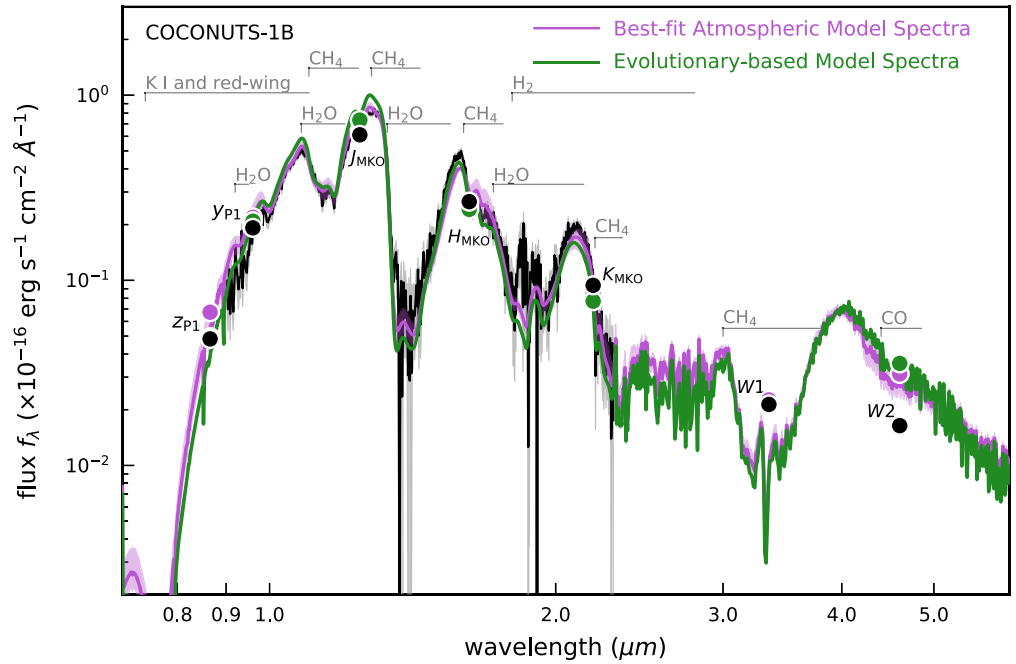

Figure 13. The evolutionary-based model spectra (green), the best-fit atmospheric model spectra (purple), and the observed spectra (black), using the same format as in Figure 12. Circles mark the fluxes derived from the observed z_{P1}, y_{P1}, J_{MKO}, $W1$, and $W2$ photometry (black), synthesized H_{MKO} and K_{MKO} photometry from the observed spectrum (black), and those synthesized from model spectra (purple and green).

ultracool dwarfs contract notably slowly, weakening the correlation between surface gravities and ages (e.g., Burrows et al. 2001; Kirkpatrick et al. 2008; Allers & Liu 2013).

6.1.1. Bolometric Luminosities, Effective Temperatures, Surface Gravities, and Masses

Table 4 collects bolometric luminosities and effective temperatures for our sample from the literature. Bolometric luminosities of objects were computed mainly from three approaches:[13] (1) integrating SEDs, (2) applying empirical relations between bolometric luminosities and infrared absolute magnitudes (e.g., Dupuy & Liu 2017), or (3) applying

[13] The only object in our sample whose L_{bol} was not derived from these three approaches is CFBDS J111807−064016, for which Reylé et al. (2014) interpolated the Baraffe et al. (2003) evolutionary models using the age of the primary star and the object's T_{eff} derived from atmospheric models (Allard et al. 2012, 2013) to compute the L_{bol}.

Table 3
L/T Transition Benchmarks: Spectral Type, Photometry, Parallax, and Age

Object	Type[a]	SpT[b]	J_{MKO} (mag)	H_{MKO} (mag)	K_{MKO} (mag)	Parallax (mas)	Age (Gyr)	Primary SpT	Separation[c] (″)	References[d] Discovery; SpT; Phot.; π; Age; P.SpT
Young Benchmarks (⩽0.3 Gyr)										
HIP 65426 b	A[e]+C	L6 ± 1	19.39 ± 0.40[f]	⋯	⋯	9.16 ± 0.06	0.014 ± 0.004	A2 V	0.83	109; 109; 1,109; 105,118; 109; 4
LP 261−75B	C	L6 ± 0.5	17.10 ± 0.21	15.94 ± 0.14	15.08 ± 0.13	29.45 ± 0.14	0.1−0.2	M4.5 V	13.6	11,37; 11; 75; 105,118; 37; 37
2MASS J2244316+204343	A[e]	L6.5 ± 0.5	16.33 ± 0.03	15.06 ± 0.03	13.90 ± 0.03	58.70 ± 1.00	$0.149^{+0.051}_{-0.019}$	⋯	⋯	17,104; 49; 106; 106; 92; ...
Calar 21	A	L6.5 ± 0.5	20.23 ± 0.08	18.74 ± 0.03	17.58 ± 0.07	7.34 ± 0.06	0.112 ± 0.005	⋯	⋯	90; 121; 45,90; 86; 97; ...
Calar 22	A	L6.5 ± 0.5	20.29 ± 0.07	18.92 ± 0.02	17.80 ± 0.09	7.34 ± 0.06	0.112 ± 0.005	⋯	⋯	90; 121; 45,90; 86; 97; ...
PSO J318.5338−22.8603	A[e]	L7 ± 1	17.15 ± 0.04	15.68 ± 0.02	14.41 ± 0.02	45.14 ± 1.73	0.024 ± 0.003	⋯	⋯	82; 82; 82; 106; 92; ...
WISE J004701.06+680352.1	A[e]	L7 ± 1 pec	15.49 ± 0.07	14.04 ± 0.04	13.01 ± 0.03	82.30 ± 1.80	$0.149^{+0.051}_{-0.019}$	⋯	⋯	76,98; 98; 106; 106; 92; ...
HD 203030B	C	L7.5 ± 0.5	18.77 ± 0.08	17.57 ± 0.08	16.16 ± 0.10	25.45 ± 0.06	0.03−0.15	G8 V	11.92	35; 35; 75,114; 105,118; 114; 5
VHS J125601.92−125723.9 b	C	L8 ± 2	17.14 ± 0.02	15.78 ± 0.02	14.67 ± 0.01[f]	58.50 ± 8.60	0.15−0.3	M7.5 V	8.06	99; 99; 99; 107; 99; 99
2MASS J22362452 +4751425 b	A[e]+C	L5−T0	19.97 ± 0.11	18.54 ± 0.18	17.28 ± 0.04	14.34 ± 0.03	$0.149^{+0.051}_{-0.019}$	K7 V[g]	3.7	108; 1,108; 108; 105,118; 92; 108
HR 8799 b	A[e]+C	L5−T2	19.46 ± 0.18	18.09 ± 0.12	16.99 ± 0.06	25.38 ± 0.70[h]	$0.06^{+0.10}_{-0.03}$	F0 V	1.73	51; 56; 106; 47,71; 51; 21
HR 8799 c	A[e]+C	L2−T0	17.63 ± 0.21	17.18 ± 0.15	16.14 ± 0.07	25.38 ± 0.70[h]	$0.06^{+0.10}_{-0.03}$	F0 V	0.95	51; 1,119; 106; 47,71; 51; 21
HR 8799 d	A[e]+C	L2−T0	18.24 ± 0.43	16.67 ± 0.19	16.05 ± 0.12	25.38 ± 0.70[h]	$0.06^{+0.10}_{-0.03}$	F0 V	0.63	51; 1,119; 106; 47,71; 51; 21
HR 8799 e	A[e]+C	L2−T0	⋯	16.28 ± 0.27	15.87 ± 0.22	25.38 ± 0.70[h]	$0.06^{+0.10}_{-0.03}$	F0 V	0.37	61; 1,119; 106; 47,71; 61; 21
2MASS J13243553+6358281	A[e]	T2.5 ± 1 pec	15.44 ± 0.07	14.68 ± 0.06	14.08 ± 0.06	78.70 ± 9.00	$0.149^{+0.051}_{-0.019}$	⋯	⋯	44,117; 58; 124; 117; 92; ...
HN Peg B	C	T2.5 ± 0.5	15.86 ± 0.03	15.40 ± 0.03	15.12 ± 0.03	55.91 ± 0.45[h]	0.3 ± 0.2	G0 V	43.2	43; 43; 43; 47,71; 43; 13
SIMP J013656.5+093347.3	A[e]	T2.5 ± 0.5	13.27 ± 0.02	12.81 ± 0.00	12.59 ± 0.00	163.68 ± 0.72	0.20 ± 0.05	⋯	⋯	30,113; 30; 78,124; 105,118; 41; ...
GU Psc b	A[e]+C	T3.5 ± 1	18.12 ± 0.03	17.70 ± 0.03	17.40 ± 0.03	21.00 ± 0.07	$0.149^{+0.051}_{-0.019}$	M3 V	41.97	87; 87; 87; 105,118; 92; 38
SDSS J111010.01+011613.1	A[e]	T5.5 ± 0.5	16.16 ± 0.01	16.20 ± 0.02	16.05 ± 0.03	52.10 ± 1.20	$0.149^{+0.051}_{-0.019}$	⋯	⋯	18,100; 31; 78; 73; 92; ...
51 Eri b	A[e]+C	T6.5 ± 1.5	19.04 ± 0.40	18.99 ± 0.21	18.67 ± 0.19	33.98 ± 0.34[h]	0.024 ± 0.003	F0 IV[i]	0.449	101; 115; 115; 47,71; 92; 7
Old Benchmarks (>0.3 Gyr)										
2MASS J01303563 −4445411B	C	L6 ± 1	17.16 ± 0.06	16.19 ± 0.10[f]	15.32 ± 0.05[f]	29.06 ± 0.30	0.25−10	M9 V	3.3	52,66; 66; 1,66; 105,118; 66; 66
HIP 9269B	C	L6 ± 1	16.13 ± 0.02	15.08 ± 0.01	14.30 ± 0.02	40.38 ± 0.04	2.2−10	G5 V	52.1	84; 84; 84; 105,118; 29; 21
SDSS J042348.57 −041403.5A	B	L6.5 ± 1.5	14.86 ± 0.04	13.96 ± 0.03	13.28 ± 0.04	71.10 ± 0.80	$0.81^{+0.07}_{-0.09}$	⋯	0.16	27; 73; 73; 110; 110; ...
SDSS J105213.51 +442255.7A	B	L6.5 ± 1.5	16.89 ± 0.06	15.81 ± 0.05	14.99 ± 0.04	38.40 ± 0.70	$1.04^{+0.14}_{-0.15}$	⋯	0.04	32,96; 96; 96; 96; 110; ...
2MASS J1728114+394859B	B	L7 ± 1	16.76 ± 0.08	15.79 ± 0.07	14.97 ± 0.05	38.70 ± 0.70	$3.4^{+2.8}_{-2.1}$	⋯	0.13	11,20; 73; 73; 73; 110; ...
LTT 7251B	C	L7 ± 2	16.93 ± 0.09	16.36 ± 0.11	⋯	26.50 ± 0.07	1−10	G8 V	14.7	120; 120; 120; 105,118; 65; 6
Gl 337D	B+C	L7.5 ± 2	16.25 ± 0.08	15.53 ± 0.08	14.93 ± 0.07	49.10 ± 0.50	0.6−3.4	G8 V + K1 V	43	15,28; 73; 73; 73; 15; 8,10,12
Luhman 16A	B	L7.5 ± 1	11.53 ± 0.04	10.37 ± 0.04	9.44 ± 0.07	500.51 ± 0.11	0.6−0.8	⋯	1.5	81; 79; 79; 102; 112; ...
Gl 584C	C	L8 ± 0.5	16.05 ± 0.01	15.08 ± 0.01	14.38 ± 0.01	55.98 ± 0.78	1.0−2.5	G1 V + G3 V	194	11,14; 11; 78; 47; 14; 2,3
PHL 5038B	C	L8 ± 1	⋯	17.90 ± 0.08[f]	17.16 ± 0.08[f]	13.71 ± 0.23	1.9−2.7	DA	0.94	54; 54; 1,54; 105,118; 54; 33
2MASS J2132114+134158B	B	L8.5 ± 1.5	16.97 ± 0.07	15.96 ± 0.07	15.09 ± 0.07	36.00 ± 0.70	$1.44^{+0.26}_{-0.37}$	⋯	0.066	42,46; 73; 73; 73; 110; ...
Gl 337C	B+C	L8.5 ± 1	16.07 ± 0.08	15.33 ± 0.08	14.67 ± 0.06	49.10 ± 0.50	0.6−3.4	G8 V + K1 V	43	15,28; 73; 73; 73; 15; 8,10,12
2MASS J14044948 −3159330A	B	L9 ± 1	16.47 ± 0.08	15.54 ± 0.07	14.83 ± 0.10	42.10 ± 1.10	$3.0^{+0.8}_{-1.3}$	⋯	0.13	44,50; 110; 73; 73; 110; ...
HD 46588B	C	L9 ± 1	16.11 ± 0.09[f]	15.14 ± 0.09[f]	14.62 ± 0.10[f]	54.93 ± 0.11	$3.04^{+1.26}_{-1.65}$	F7 V	79.2	68; 68; 1,39; 105,118; 65; 53

Table 3
(Continued)

Object	Type[a]	SpT[b]	J_{MKO} (mag)	H_{MKO} (mag)	K_{MKO} (mag)	Parallax (mas)	Age (Gyr)	Primary SpT	Separation[c] ($''$)	References[d] Discovery; SpT; Phot.; π; Age; P.SpT
Luhman 16B	B	T0.5 ± 1	11.22 ± 0.04	10.39 ± 0.04	9.73 ± 0.09	500.51 ± 0.11	0.6−0.8	⋯	1.5	81; 79; 79; 102; 112; ...
ϵ Indi Ba	B+C	T1 ± 0.5	12.20 ± 0.03	11.60 ± 0.02	11.42 ± 0.02	274.80 ± 0.25	3.7−4.3	K5 V	402.3	22,26; 26; 59; 105,118; 59; 40
SDSS J105213.51 +442255.7B	B	T1.5 ± 1	16.44 ± 0.05	15.87 ± 0.05	15.50 ± 0.04	38.40 ± 0.70	$1.04^{+0.14}_{-0.15}$	⋯	0.04	32,96; 96; 96; 96; 110; ...
SDSS J042348.57 −041403.5B	B	T2 ± 0.5	15.28 ± 0.05	14.68 ± 0.04	14.46 ± 0.07	71.10 ± 0.80	$0.81^{+0.07}_{-0.09}$	⋯	0.16	27; 73; 73; 110; 110; ...
CFHT-Hy-20	A[e]	T2.5 ± 1	17.02 ± 0.05	16.51 ± 0.05	16.08 ± 0.05	30.80 ± 1.50	0.75 ± 0.1	⋯	⋯	48; 106; 106; 106; 94; ...
2MASS J02132062 +3648506C	C	T3 ± 0.5	15.16 ± 0.01	14.89 ± 0.02	14.93 ± 0.02	70.02 ± 0.20	1−10	M4.5 V + M6.5 V	16.4	111; 111; 111; 105,118; 111; 38,77
DENIS J225210.73 −173013.4B	B	T3.5 ± 0.5	15.36 ± 0.06	14.90 ± 0.07	14.82 ± 0.07	63.20 ± 1.60	$1.11^{+0.19}_{-0.22}$	⋯	0.13	24,36; 110; 73; 73; 110; ...
COCONUTS-1B	C	T4 ± 0.5	16.73 ± 0.02	16.62 ± 0.02	16.58 ± 0.02	31.71 ± 0.09	$7.3^{+2.8}_{-1.6}$	DA	40.61	1; 1; 1,116; 105,118; 1; 1
2MASS J15344984 −2952274A	B	T4.5 ± 0.5	15.27 ± 0.03	15.36 ± 0.03	15.53 ± 0.03	62.40 ± 1.30	$3.0^{+0.4}_{-0.5}$	⋯	0.065	16,19; 73; 73; 73; 110; ...
HIP 38939B	C	T4.5 ± 0.5	15.90 ± 0.08	16.03 ± 0.08	16.22 ± 0.08	54.10 ± 0.04	$0.9^{+1.9}_{-0.6}$	K4 V	88	72; 72; 72; 105,118; 72; 34
2MASS J14044948 −3159330B	B	T5 ± 0.5	15.93 ± 0.07	16.05 ± 0.07	16.16 ± 0.10	42.10 ± 1.10	$3.0^{+0.8}_{-1.3}$	⋯	0.13	44,50; 110; 73; 73; 110; ...
2MASS J15344984 −2952274B	B	T5 ± 0.5	15.44 ± 0.03	15.64 ± 0.03	15.82 ± 0.03	62.40 ± 1.30	$3.0^{+0.4}_{-0.5}$	⋯	0.065	16,19; 73; 73; 73; 110; ...
ULAS J133943.79+010436.4	C	T5 ± 0.5	18.10 ± 0.02	18.20 ± 0.04	18.39 ± 0.05	16.45 ± 0.06	$3.23^{+1.24}_{-1.59}$	F7 V	148	80; 80; 80,103; 105,118; 65; 9
HD 19467B	C	T5.5 ± 1	17.36 ± 0.11[f]	17.96 ± 0.11[f]	18.09 ± 0.09[f]	31.23 ± 0.04	4.6−10	G3 V	1.65	83; 95; 1,83; 105,118; 95; 6
LHS 2803B	C	T5.5 ± 0.5	16.39 ± 0.02	16.57 ± 0.04	16.90 ± 0.08	55.00 ± 0.08	3.5−10	M4.5 V	67.6	74; 74; 74; 105,118; 74; 74
WISE J072003.20 −084651.2B	C	T5.5 ± 0.5	13.26 ± 0.04	13.24 ± 0.04	13.31 ± 0.07	147.10 ± 1.20	$6.8^{+2.2}_{-3.1}$	M9.5 V	0.197	93; 93; 122,124; 122; 122; 89
ϵ Indi Bb	B+C	T6 ± 0.5	12.96 ± 0.03	13.40 ± 0.03	13.64 ± 0.02	274.80 ± 0.25	3.7−4.3	K5 V	402.3	22,26; 26; 59; 105,118; 59; 40
HIP 73786B	C	T6 ± 1 pec	16.59 ± 0.02	17.05 ± 0.04	17.41 ± 0.09	52.59 ± 0.07	1.6−10	K8 V	63.8	63,69; 69; 78; 105,118; 69; 60
SDSS J175805.46+463311.9	C	T6.5 ± 0.5	15.86 ± 0.03	16.20 ± 0.03	16.12 ± 0.03	71.48 ± 0.04	0.5−3.0	M2.5 V	198	25,57; 31; 25; 105,118; 57; 91
IR-Bright Old Benchmarks (>0.3 Gyr)										
NLTT 31450B	C	L6 ± 1	15.97 ± 0.02	15.08 ± 0.02	14.29 ± 0.06	25.89 ± 0.05	0.3−10	M4 V	12.3	84; 84; 84,124; 105,118; 84; 84
2MASS J00150206+2959323	C	L7 ± 0.5	16.16 ± 0.03	15.22 ± 0.03	14.58 ± 0.06	28.61 ± 0.07	3−10	M4 V	233.6	58,84; 58; 84,124; 105,118; 84; 84
PM I23492+3458B	C	L9 ± 0.5	16.39 ± 0.03	15.47 ± 0.02	14.87 ± 0.06	32.76 ± 0.04	0.3−10	M2 V	34.9	84; 84; 84,124; 105,118; 84; 84
SDSS J213154.43−011939.3	C	L9 ± 1	17.23 ± 0.01	16.42 ± 0.02	15.54 ± 0.06[f]	21.46 ± 0.61	1−10	M3 V + M6 V[g]	82.27	32,123; 123; 1,123; 105,118; 123; 123

Table 3
(Continued)

Object	Type[a]	SpT[b]	J_{MKO} (mag)	H_{MKO} (mag)	K_{MKO} (mag)	Parallax (mas)	Age (Gyr)	Primary SpT	Separation[c] ($''$)	References[d] Discovery; SpT; Phot.; π; Age; P.SpT
CFBDS J111807−064016	C	T2.5 ± 0.5	18.86 ± 0.03[f]	18.64 ± 0.02[f]	18.32 ± 0.04[f]	9.90 ± 0.15	6−10	M4.5 V	7.7	88; 88; 1,88; 105,118; 88; 88
HIP 70849B	C	T4.5 ± 0.5	15.54 ± 0.01	⋯	⋯	41.54 ± 0.04	1−5	K7 V	378	85; 85; 23; 105,118; 70; 34
LSPM J1459+0857B	C	T4.5 ± 0.5	17.93 ± 0.02	17.94 ± 0.05	17.92 ± 0.08	13.79 ± 0.35	4.8−10	DA	385	55,64,67; 62; 67; 105,118; 67; 67

Notes.
[a] "A": Association or young moving group members; "B": Binaries composed of substellar components; "C": Companions to stars or white dwarfs.
[b] We adopt the object's near-infrared spectral type if it is T type or if the object's optical spectral type is lacking, otherwise, we adopt the object's optical spectral type.
[c] Angular separations were reported in the literature at the epoch of their discoveries. For companions that are themselves are binaries (Type "B+C"), Gl 337 CD and ϵ Indi Bab, the tabulated separations are between binary components. Gl 337 CD is separated from Gl 337 AB (a double-lined spectroscopic and visual binary with orbital period of 2.7 yr; Mason 1996) by 43$''$ when discovered by Wilson et al. (2001), and ϵ Indi Bab is separated from ϵ Indi A by $402\overset{''}{.}3$ when discovered by Scholz et al. (2003).
[d] Reference of the object's discovery, spectral type, photometry, parallax, age, and the primary star's spectral type (if companion). References for the different properties are separated by semicolons and multiple references for the same property are separated by commas.
[e] The object is a member of a young moving group or association. AB Doradus: 2MASS J2244316+204343 (Faherty et al. 2016), WISE J004701.06+680352.1 (Gizis et al. 2015), 2MASS J22362452+4751425 b (Bowler et al. 2017), 2MASS J13243553+6358281 (Gagné et al. 2018), GU Psc b (Naud et al. 2014), SDSSp J111010.01+011613.1 (Gagné et al. 2015). β Pictoris: PSO J318.5338−22.8603 (Liu et al. 2013), 51 Eri b (Zuckerman et al. 2001). Carina-Near: SIMP J013656.5+093347.3 (Gagné et al. 2017). Columba: HR 8799 (Zuckerman et al. 2011). Hyades: CFHT−Hy−20 (Bouvier et al. 2008). Lower Centaurus-Crux: HIP 65426 b (Chauvin et al. 2017).
[f] The MKO photometry is converted from 2MASS photometry. For HIP 65426 b, we derive the *J*-band MKO−2MASS conversion from three young or dusty objects that have similar *J*-band appearances: (Chauvin et al. 2017), including 2MASS J03552337+1133437 (L5; Reid et al. 2006a), 2MASS J21481628+4003593 (L6; Looper et al. 2008b), and PSO J057.2893+15.2433 (L7; Best et al. 2015). We adopt the MKO−2MASS relation from Dupuy & Liu (2017) for remaining objects.
[g] Spectral type is derived based on photometry.
[h] While both *Gaia* DR2 and *Hipparcos* parallaxes exist for the primary star, we adopt the *Hipparcos* parallax given that the primary star's *Gaia* DR2 *G*-band photometry saturate, thereby making its *Gaia* DR2 astrometry suspicious.
[i] The primary star also has an M-dwarf binary companion GJ 3305 AB (Feigelson et al. 2006) at a separation of 66$''$. GJ 3305 AB has an unresolved spectral type of M1.1 ± 0.5 (Shkolnik et al. 2009) with a separation of $\approx 0\overset{''}{.}3$ (Janson et al. 2014).

References. (1) This work, (2) Struve & Franklin (1955), (3) Edwards (1976), (4) Houk (1978), (5) Jaschek (1978), (6) Houk & Smith-Moore (1988), (7) Abt & Morrell (1995), (8) Mason (1996), (9) Houk & Swift (1999), (10) Barnaby et al. (2000), (11) Kirkpatrick et al. (2000), (12) Richichi et al. (2000), (13) Gray et al. (2001), (14) Kirkpatrick et al. (2001), (15) Wilson et al. (2001), (16) Burgasser et al. (2002), (17) Dahn et al. (2002), (18) Geballe et al. (2002), (19) Burgasser et al. (2003), (20) Gizis et al. (2003), (21) Gray et al. (2003), (22) Scholz et al. (2003), (23) Emerson et al. (2004), (24) Kendall et al. (2004), (25) Knapp et al. (2004), (26) McCaughrean et al. (2004), (27) Burgasser et al. (2005b), (28) Burgasser et al. (2005a), (29) Valenti & Fischer (2005), (30) Artigau et al. (2006), (31) Burgasser et al. (2006a), (32) Chiu et al. (2006), (33) Eisenstein et al. (2006), (34) Gray et al. (2006), (35) Metchev & Hillenbrand (2006), (36) Reid et al. (2006b), (37) Reid & Walkowicz (2006), (38) Riaz et al. (2006), (39) Skrutskie et al. (2006), (40) Torres et al. (2006), (41) Zuckerman et al. (2006), (42) Cruz et al. (2007), (43) Luhman et al. (2007), (44) Looper et al. (2007), (45) Lawrence et al. (2007), (46) Siegler et al. (2007), (47) van Leeuwen (2007), (48) Bouvier et al. (2008), (49) Kirkpatrick et al. (2008), (50) Looper et al. (2008a), (51) Marois et al. (2008), (52) Reid et al. (2008), (53) Abt (2009), (54) Steele et al. (2009), (55) Burningham et al. (2010), (56) Bowler et al. (2010), (57) Faherty et al. (2010), (58) Kirkpatrick et al. (2010), (59) King et al. (2010), (60) Koen et al. (2010), (61) Marois et al. (2010), (62) Reylé et al. (2010), (63) Scholz (2010), (64) Albert et al. (2011), (65) Casagrande et al. (2011), (66) Dhital et al. (2011), (67) Day-Jones et al. (2011), (68) Loutrel et al. (2011), (69) Murray et al. (2011), (70) Ségransan et al. (2011), (71) Anderson & Francis (2012), (72) Deacon et al. (2012a), (73) Dupuy & Liu (2012), (74) Deacon et al. (2012b), (75) Faherty et al. (2012), (76) Gizis et al. (2012), (77) Janson et al. (2012), (78) Lawrence et al. (2012), (79) Burgasser et al. (2013), (80) Burningham et al. (2013), (81) Luhman (2013), (82) Liu et al. (2013), (83) Crepp et al. (2014), (84) Deacon et al. (2014), (85) Lodieu et al. (2014), (86) Melis et al. (2014), (87) Naud et al. (2014), (88) Reylé et al. (2014), (89) Scholz (2014), (90) Zapatero Osorio et al. (2014), (91) Alonso-Floriano et al. (2015), (92) Bell et al. (2015), (93) Burgasser et al. (2015), (94) Brandt & Huang (2015), (95) Crepp et al. (2015), (96) Dupuy et al. (2015), (97) Dahm (2015), (98) Gizis et al. (2015), (99) Gauza et al. (2015), (100) Gagné et al. (2015), (101) Macintosh et al. (2015), (102) Sahlmann & Lazorenko (2015), (103) Edge et al. (2016), (104) Faherty et al. (2016), (105) Gaia Collaboration et al. (2016), (106) Liu et al. (2016), (107) Stone et al. (2016), (108) Bowler et al. (2017), (109) Chauvin et al. (2017), (110) Dupuy & Liu (2017), (111) Deacon et al. (2017), (112) Garcia et al. (2017), (113) Gagné et al. (2017), (114) Miles-Páez et al. (2017), (115) Rajan et al. (2017), (116) Dye et al. (2018), (117) Gagné et al. (2018), (118) Gaia Collaboration et al. (2018), (119) Greenbaum et al. (2018), (120) Smith et al. (2018), (121) Zapatero Osorio et al. (2018), (122) Dupuy et al. (2019), (123) Gauza et al. (2019), (124) W. M. J. Best et al. (2020, in preparation).

bolometric corrections based on the objects' spectral types to infrared absolute magnitudes (e.g., Golimowski et al. 2004; Liu et al. 2010; Filippazzo et al. 2015). These methods usually produce consistent results, with the first method having the best precision. Results from the third method can have large uncertainties because spectral types of some L/T dwarfs (e.g., 2MASS J22362452+4751425 b [2MASS 2236 b] in Bowler et al. 2017; the HR 8799 planets in Greenbaum et al. 2018) are not well-determined.

For objects whose literature $L_{\rm bol}$ values are either lacking or derived from bolometric corrections (method 3), we have (re-) computed their $L_{\rm bol}$ using the empirical relations between $L_{\rm bol}$ and H- or K-band absolute magnitudes from Dupuy & Liu (2017). These relations are based on field dwarfs with ages $\gtrsim$0.5 Gyr from Filippazzo et al. (2015), who derived the objects' bolometric luminosities from a uniform SED analysis. We use the objects' H-band absolute magnitudes to compute their $L_{\rm bol}$ and switch to the K band when their H-band absolute magnitudes are fainter than 13.3 mag, as suggested by Dupuy & Liu (2017).

HIP 65426 b (L6 ± 1; Chauvin et al. 2017), VHS J125601.92−125723.9 b (VHS 1256 b; L8 ± 2; Gauza et al. 2015), LTT 7251B (L7 ± 2; Smith et al. 2018), and HIP 70849B (T4.5 ± 0.5; Lodieu et al. 2014) are four exceptions to our re-calculation. HIP 65426 b is too young (14 ± 4 Myr; Chauvin et al. 2017) for the Dupuy & Liu (2017) relations to be applied ($\geqslant$0.5 Gyr). Chauvin et al. (2017) derived $L_{\rm bol}$ of HIP 65426 b by using the *Gaia* DR1 parallax (8.98 ± 0.30 mas) of the primary and a bolometric correction from four dusty L5–L7.5 dwarfs (Filippazzo et al. 2015). Here, we update the $L_{\rm bol}$ of HIP 65426 b by using the *Gaia* DR2 parallax (9.16 ± 0.06 mas) of the primary star, the companion's estimated $J_{\rm 2MASS}$ magnitude (19.50 ± 0.40 mag; computed from the primary star's $J_{\rm 2MASS}$ and the photometric contrast in Chauvin et al. 2017), and the J-band bolometric correction for young L6 dwarfs from Filippazzo et al. (2015).

VHS 1256 b also has a very young age (0.15–0.3 Gyr; Gauza et al. 2015) that prevents the application of the Dupuy & Liu (2017) relations. Gauza et al. (2015) derived $L_{\rm bol}$ of VHS 1256 b using their own preliminary parallax of 78.8 ± 6.4 mas (12.7 ± 1.0 pc) and the bolometric correction for PSO J318.5338−22.8603 (Liu et al. 2013). After the discovery of VHS 1256 b, Stone et al. (2016) found that the primary is a 0.″1-wide, equal-brightness binary, with a spectrophotometric distance of 17.1 ± 2.5 pc. Such a distance is in tension with the Gauza et al. (2015) parallactic distance, but is more consistent with the parallax measured by the Hawaii Infrared Parallax Program (T. Dupuy, private communication). We thus adopt a parallax of 58.5 ± 8.6 mas based on the Stone et al. (2016) spectrophotometric distance. We then use the object's measured $K_{\rm 2MASS}$ magnitude (14.57 ± 0.12 mag Cutri et al. 2003) and the K-band bolometric correction for young L8 dwarfs from Filippazzo et al. (2015) to update the $L_{\rm bol}$ of VHS 1256 b.

LTT 7251B is an L7 companion to a G8 dwarf star found by Smith et al. (2018) using their infrared astrometric catalog of the VISTA Variables in the Via Lactea (VVV) survey (Minniti et al. 2010; Sutherland et al. 2015). Its H-band absolute magnitude is too faint to use the Dupuy & Liu (2017) relations and has a K-band magnitude from VVV, which is in neither the 2MASS nor MKO photometric systems (e.g., González-Fernández et al. 2018). We therefore compute the companion's $L_{\rm bol}$ from its estimated $J_{\rm 2MASS}$ magnitude (17.02 ± 0.13; converted from its $J_{\rm MKO}$ based on known L5–L9 dwarfs in W. M. J. Best et al. 2020, in preparation) and the J-band bolometric correction for field L7 dwarfs from Filippazzo et al. (2015).

HIP 70849B is a T4.5 companion to a K7 dwarf star found by Lodieu et al. (2014). The primary star also hosts a close-in (P = 5–90 yr) giant planet ($M \sin i$ = 3–15 $M_{\rm Jup}$) detected via radial velocity (Ségransan et al. 2011). Similar to LTT 7251B, HIP 70849B has a too faint H-band absolute magnitude and a K-band magnitude from the VISTA Hemisphere Survey (VHS; McMahon et al. 2013). We therefore compute the object's $L_{\rm bol}$ by using its measured $J_{\rm 2MASS}$ magnitude (15.89 ± 0.07; Cutri et al. 2003) and the J-band bolometric correction for field T4.5 dwarfs from Filippazzo et al. (2015).

Effective temperatures of objects have been computed in the literature mainly from two approaches:[14] (1) fitting the objects' near-infrared spectra using atmospheric models, or (2) interpolating hot-start evolutionary models using the objects' $L_{\rm bol}$ and independent ages or dynamical masses. Ideally, the two methods should produce consistent results, although the evolutionary model parameters are usually more robust and less vulnerable to well-noted shortcomings of atmospheric models (Section 5.5). In addition, three groups of evolutionary models have been used in the literature: (1) the Saumon & Marley (2008) models and Sonora models (Marley et al. 2017; Marley et al. 2019, in preparation), (2) the Burrows et al. (1997) models, and (3) the Lyon group's models (Baraffe et al. 2003, 2015). These three sets of models have made different assumptions about initial interior composition, atmosphere boundary conditions, and electron conduction, but are generally consistent (Saumon & Marley 2008).

Similar to $L_{\rm bol}$, we have (re-)computed $T_{\rm eff}$ for most of our sample. We have also computed the objects' surface gravities and masses. We adopt the existing effective temperatures, surface gravities, and dynamical masses for the substellar binary components and WISE 0720B from Dupuy & Liu (2017) and Dupuy et al. (2019), respectively. The $T_{\rm eff}$ and $\log g$ values of these objects were determined from interpolating the Saumon & Marley (2008) hybrid evolutionary models using their measured $L_{\rm bol}$ and dynamical masses. For the remaining objects, we compute $T_{\rm eff}$, $\log g$, and M by interpolating the same Saumon & Marley (2008) hybrid models using the objects' $L_{\rm bol}$ and ages. We assume the objects' bolometric luminosities follow a normal distribution and assume their ages follow a uniform distribution (if the object's age is given as a range in the literature) or a Gaussian distribution (if the age is given with an error bar in the literature)[15] truncated within 0–10 Gyr. The evolutionary model parameters for COCONUTS-1B derived from the Saumon & Marley (2008) hybrid models are consistent with our analysis using the cloudless Sonora models (Section 5.4), so we keep the Sonora-based results. For 51 Eri b, we also compute physical parameters

[14] Objects in our sample whose $T_{\rm eff}$ were not derived from these two approaches are PHL 5038B (Steele et al. 2009), LSPM J1459+0857B (Day-Jones et al. 2011), WISE J004701.06+680352.1 (Gizis et al. 2012, 2015), and Luhman 16AB (Luhman 2013). $T_{\rm eff}$ of the first two objects were converted from spectral types based on temperature scales (Golimowski et al. 2004; Vrba et al. 2004), and the $T_{\rm eff}$ of the latter two were estimated from the measured $L_{\rm bol}$ by assuming a radii from evolutionary models (e.g., Burrows et al. 1997; Baraffe et al. 1998; Chabrier et al. 2000).

[15] For ages with asymmetric errors, we assume a distribution composed of two half-Gaussians, with upper and lower uncertainties corresponding to standard deviations of the two Gaussians, similar to our Section 5.4.

Table 4
L/T Transition Benchmarks: Bolometric Luminosity, Effective Temperature, Surface Gravity, and Mass

Object	SpT	Literature					Adopted				
		log ($L_{bol}/L_{\odot}$) (dex)	L_{bol} Method[a]	T_{eff} (K)	T_{eff} Method[b]	References	log ($L_{bol}/L_{\odot}$) (dex)	T_{eff} (K)	log g (dex)	M (M_{Jup})	References[c] L_{bol}; Phys.
Young Benchmarks (≤0.3 Gyr)											
HIP 65426 b	L6 ± 1	−4.06 ± 0.10	BC −SpT (34)	1500^{+100}_{-200}	Evo−Age (4,7)	39	$-4.136^{+0.177}_{-0.177}$	1359^{+126}_{-105}	$3.99^{+0.11}_{-0.13}$	$8.7^{+2.7}_{-2.5}$	1; 1
LP 261 − 75B	L6 ± 0.5	−4.43 ± 0.09	SED	…	…	28	−4.430 ± 0.090	1264^{+75}_{-49}	$4.44^{+0.13}_{-0.09}$	$16.3^{+5.4}_{-2.2}$	28; 1
2MASS J2244316+204343	L6.5 ± 0.5	−4.503 ± 0.007	SED	1184 ± 10[d]	Evo−Age (11)	37	−4.503 ± 0.007	1228^{+24}_{-10}	$4.42^{+0.13}_{-0.04}$	$15.5^{+3.9}_{-1.1}$	37; 1
Calar 21	L6.5 ± 0.5	−4.29 ± 0.10	SED	1350^{+100}_{-80}	Evo−Age (30,33)	48	−4.290 ± 0.100	1352^{+97}_{-72}	$4.44^{+0.16}_{-0.08}$	$17.9^{+6.7}_{-3.1}$	48; 1
Calar 22	L6.5 ± 0.5	−4.33 ± 0.10	SED	1350^{+100}_{-80}	Evo−Age (30,33)	48	−4.330 ± 0.100	1322^{+69}_{-68}	$4.40^{+0.11}_{-0.06}$	$16.9^{+3.8}_{-3.0}$	48; 1
PSO J318.5338−22.8603	L7 ± 1	−4.42 ± 0.06	SED	1160^{+30}_{-40}[d]	Evo−Age (11)	29	−4.420 ± 0.060	1210^{+36}_{-37}	$4.00^{+0.04}_{-0.04}$	$7.5^{+0.7}_{-0.6}$	29; 1
WISE J004701.06 +680352.1	L7 ± 1 pec	−4.45 ± 0.04	SED	1270−1300[d]	Radius (3,4)	35	−4.450 ± 0.040	1256^{+39}_{-19}	$4.42^{+0.12}_{-0.06}$	$15.8^{+4.1}_{-1.4}$	35; 1
HD 203030B	L7.5 ± 0.5	−4.75 ± 0.04	SED	1040 ± 50	Evo−Age (7,11,33)	44	−4.750 ± 0.040	1053^{+26}_{-27}	$4.25^{+0.06}_{-0.14}$	$10.8^{+1.3}_{-2.3}$	44; 1
VHS J125601.92 −125723.9 b	L8 ± 2	−5.05 ± 0.22	BC −SpT (29)	880^{+140}_{-110}	Evo−Age (3,4,7,11)	36	$-4.731^{+0.149}_{-0.140}$	1105^{+99}_{-94}	$4.44^{+0.14}_{-0.08}$	$15.1^{+4.3}_{-2.2}$	1; 1
2MASS J22362452 +4751425 b	L5−T0	−4.57 ± 0.06	SED	1170 ± 40[d]	Evo−Age (11)	38	−4.570 ± 0.060	1189^{+40}_{-42}	$4.41^{+0.10}_{-0.05}$	$14.8^{+2.8}_{-1.4}$	38; 1
HR 8799 b	L5−T2	−4.95 ± 0.06	SED	1000	Atm (24)	24	−4.950 ± 0.060	937^{+38}_{-37}	$4.12^{+0.20}_{-0.18}$	$8.2^{+3.4}_{-2.3}$	24; 1
HR 8799 c	L2−T0	−4.72 ± 0.15	SED	1100	Atm (18)	47	−4.720 ± 0.150	1064^{+96}_{-87}	$4.18^{+0.19}_{-0.18}$	$9.8^{+3.6}_{-2.9}$	47; 1
HR 8799 d	L2−T0	−4.72 ± 0.15	SED	1100	Atm (18)	47	−4.720 ± 0.150	1064^{+96}_{-87}	$4.18^{+0.18}_{-0.18}$	$9.8^{+3.6}_{-2.9}$	47; 1
HR 8799 e	L2−T0	−4.65 ± 0.15	SED	1100	Atm (18)	47	−4.650 ± 0.150	1107^{+97}_{-92}	$4.19^{+0.19}_{-0.17}$	$10.2^{+4.0}_{-3.0}$	47; 1
2MASS J13243553 +6358281	T2.5 ± 1 pec	−4.72 ± 0.10	SED	1080 ± 60	Evo−Age (11)	46	−4.720 ± 0.100	1093^{+65}_{-63}	$4.36^{+0.07}_{-0.05}$	$13.2^{+1.8}_{-1.3}$	46; 1
HN Peg B	T2.5 ± 0.5	−4.77 ± 0.03	SED	1130 ± 70	Evo−Age (2,7)	10	−4.770 ± 0.030	1098^{+37}_{-51}	$4.60^{+0.15}_{-0.27}$	$19.3^{+5.2}_{-7.1}$	10; 1
SIMP J013656.5+093347.3	T2.5 ± 0.5	−4.688 ± 0.005	SED	1098 ± 6	Evo−Age (11)	42	−4.688 ± 0.005	1126^{+16}_{-15}	$4.46^{+0.09}_{-0.08}$	$15.6^{+2.4}_{-2.1}$	42; 1
GU Psc b	T3.5 ± 1	−4.87 ± 0.10	SED	981 ± 57[d]	Evo−Age (11)	34	−4.870 ± 0.100	1002^{+59}_{-54}	$4.32^{+0.05}_{-0.04}$	$11.9^{+1.3}_{-0.8}$	34; 1
SDSS J111010.01 +011613.1	T5.5 ± 0.5	−4.97 ± 0.02	SED	926 ± 18[d]	Evo−Age (11)	34	−4.970 ± 0.020	948^{+12}_{-11}	$4.30^{+0.04}_{-0.03}$	$11.3^{+0.9}_{-0.5}$	34; 1
51 Eri b (hot-start)	T6.5 ± 1.5	−5.87 ± 0.15	SED	650−737	Atm (16,25)	45	−5.870 ± 0.150	588^{+35}_{-25}	$3.55^{+0.05}_{-0.03}$	$2.3^{+0.3}_{-0.2}$	45; 1
51 Eri b (cold-start)							−5.870 ± 0.150	548^{+9}_{-42}	$3.86^{+0.23}_{-0.28}$	$4.4^{+2.5}_{-1.9}$	45; 1
Old Benchmarks (>0.3 Gyr)											
2MASS J01303563 −4445411B	L6 ± 1	…	…	…	…	...	−4.437 ± 0.053	1478^{+45}_{-48}	$5.36^{+0.00}_{-0.06}$	$71.9^{+0.9}_{-5.5}$	1; 1
HIP 9269B	L6 ± 1	…	…	…	…	...	−4.328 ± 0.023	1574^{+19}_{-19}	$5.36^{+0.00}_{-0.01}$	$73.5^{+0.3}_{-0.6}$	1; 1
SDSS J042348.57 −041403.5A	L6.5 ± 1.5	−4.41 ± 0.04	BOL −IR (40)	1430^{+30}_{-40}	Evo−Mass (11)	40	−4.410 ± 0.040	1430^{+30}_{-40}	$5.13^{+0.03}_{-0.03}$	$51.7^{+2.4}_{-2.3}$	40; 40
SDSS J105213.51 +442255.7A	L6.5 ± 1.5	−4.51 ± 0.04	BOL −IR (40)	1366^{+25}_{-29}	Evo−Mass (11)	40	−4.510 ± 0.040	1366^{+25}_{-29}	5.12 ± 0.04	51.0 ± 3.0	40; 40
2MASS J1728114 +394859B	L7 ± 1	−4.49 ± 0.04	BOL −IR (40)	1440 ± 40	Evo−Mass (11)	40	−4.490 ± 0.040	1440 ± 40	$5.35^{+0.02}_{-0.02}$	67.0 ± 5.0	40; 40
LTT 7251B	L7 ± 2	…	…	…	…	...	$-4.341^{+0.085}_{-0.085}$	1561^{+71}_{-70}	$5.36^{+0.00}_{-0.02}$	$73.0^{+1.2}_{-2.1}$	1; 1
Gl 337D	L7.5 ± 2	…	…	…	…	...	−4.638 ± 0.053	1307^{+46}_{-53}	$5.23^{+0.09}_{-0.21}$	$55.0^{+8.8}_{-15.5}$	1; 1

Table 4
(Continued)

Object	SpT	Literature					Adopted				
		log ($L_{bol}/L_{\odot}$) (dex)	L_{bol} Method[a]	T_{eff} (K)	T_{eff} Method[b]	References	log ($L_{bol}/L_{\odot}$) (dex)	T_{eff} (K)	log g (dex)	M (M_{Jup})	References[c] L_{bol}; Phys.
Luhman 16A	L7.5 ± 1	−4.67 ± 0.04	SED	1310 ± 30	Radius (9)	31	−4.670 ± 0.040	1217^{+28}_{-27}	$4.88^{+0.03}_{-0.03}$	$30.9^{+2.0}_{-1.7}$	31; 1
Gl 584C	L8 ± 0.5	−4.60 ± 0.01	SED	1295 ± 76[d]	Evo−Age (11)	34	−4.600 ± 0.010	1334^{+16}_{-26}	$5.22^{+0.06}_{-0.11}$	$55.5^{+5.7}_{-9.3}$	34; 1
PHL 5038B	L8 ± 1	…	…	1400−1500	SpT (9)	12	−4.497 ± 0.056	1428^{+44}_{-43}	$5.32^{+0.01}_{-0.02}$	$67.4^{+1.7}_{-2.9}$	1; 1
2MASS J2132114 +134158B	L8.5 ± 1.5	$-4.50^{+0.05}_{-0.04}$	BOL −IR (40)	1400^{+30}_{-40}	Evo−Mass (11)	40	$-4.500^{+0.050}_{-0.040}$	1400^{+30}_{-40}	$5.26^{+0.04}_{-0.06}$	60.0 ± 4.0	40; 40
Gl 337C	L8.5 ± 1	…	…	…	…	...	−4.572 ± 0.053	1356^{+46}_{-53}	$5.27^{+0.06}_{-0.20}$	$60.6^{+6.7}_{-16.4}$	1; 1
2MASS J14044948 −3159330A	L9 ± 1	$-4.52^{+0.06}_{-0.05}$	BOL −IR (40)	1400^{+40}_{-50}	Evo−Mass (11)	40	$-4.520^{+0.060}_{-0.050}$	1400^{+40}_{-50}	$5.34^{+0.03}_{-0.04}$	65.0 ± 6.0	40; 40
HD 46588B	L9 ± 1	−4.68 ± 0.05	BC−SpT (8)	1360^{+50}_{-80}	Evo−Age (2,7)	20	−4.631 ± 0.056	1331^{+42}_{-53}	$5.32^{+0.03}_{-0.17}$	$63.7^{+4.5}_{-15.3}$	1; 1
Luhman 16B	T0.5 ± 1	−4.71 ± 0.10	SED	1280 ± 75	Radius (9)	31	−4.710 ± 0.100	1190^{+69}_{-67}	$4.86^{+0.05}_{-0.04}$	$29.8^{+3.6}_{-2.3}$	31; 1
ϵ Indi Ba	T1 ± 0.5	−4.699 ± 0.017	SED	1352−1385	Evo−Age (7)	14	−4.699 ± 0.017	1304^{+11}_{-11}	$5.34^{+0.00}_{-0.01}$	$64.3^{+0.9}_{-0.9}$	14; 1
SDSS J105213.51 +442255.7B	T1.5 ± 1	−4.64 ± 0.07	BOL −IR (40)	1270 ± 40	Evo−Mass (11)	40	−4.640 ± 0.070	1270 ± 40	$5.02^{+0.05}_{-0.04}$	$39.4^{+2.6}_{-2.7}$	40; 40
SDSS J042348.57 −041403.5B	T2 ± 0.5	−4.72 ± 0.07	BOL −IR (40)	1200 ± 40	Evo−Mass (11)	40	−4.720 ± 0.070	1200 ± 40	4.90 ± 0.03	$31.8^{+1.5}_{-1.6}$	40; 40
CFHT-Hy-20	T2.5 ± 1	…	…		…	...	−4.672 ± 0.058	1220^{+41}_{-40}	$4.90^{+0.05}_{-0.05}$	$32.0^{+3.1}_{-2.6}$	1; 1
2MASS J02132062 +3648506C	T3 ± 0.5	−4.75 ± 0.06	BC −SpT (15)	1641^{+167}_{-167}	Evo−Age (7)	41	−4.824 ± 0.050	1227^{+36}_{-46}	$5.36^{+0.04}_{-0.18}$	$63.6^{+4.0}_{-15.3}$	1; 1
DENIS J225210.73 −173013.4B	T3.5 ± 0.5	$-4.76^{+0.08}_{-0.07}$	BOL −IR (40)	1210^{+50}_{-40}	Evo−Mass (11)	40	$-4.760^{+0.080}_{-0.070}$	1210^{+50}_{-40}	5.08 ± 0.06	41.0 ± 4.0	40; 40
COCONUTS-1B	T4 ± 0.5	−4.832 ± 0.007	SED	1255^{+6}_{-8}	Evo−Age (43)	1	−4.832 ± 0.007	1255^{+6}_{-8}	$5.44^{+0.02}_{-0.03}$	$69.3^{+1.6}_{-3.4}$	1; 1
2MASS J15344984 −2952274A	T4.5 ± 0.5	−4.91 ± 0.07	BOL −IR (40)	1150^{+40}_{-50}	Evo−Mass (11)	40	−4.910 ± 0.070	1150^{+40}_{-50}	5.25 ± 0.06	51.0 ± 5.0	40; 40
HIP 38939B	T4.5 ± 0.5	−4.92 ± 0.072	BC −SpT (15)	1090^{+70}_{-60}	Evo−Age (2)	22	−5.008 ± 0.054	1021^{+64}_{-62}	$4.86^{+0.32}_{-0.24}$	$28.5^{+17.9}_{-9.4}$	1; 1
2MASS J14044948 −3159330B	T5 ± 0.5	$-4.87^{+0.08}_{-0.07}$	BOL −IR (40)	1190 ± 50	Evo−Mass (11)	40	$-4.870^{+0.080}_{-0.070}$	1190 ± 50	5.30 ± 0.08	$55.0^{+6.0}_{-7.0}$	40; 40
2MASS J15344984 −2952274B	T5 ± 0.5	−4.99 ± 0.07	BOL −IR (40)	1100^{+40}_{-50}	Evo−Mass (11)	40	−4.990 ± 0.070	1100^{+40}_{-50}	$5.22^{+0.07}_{-0.06}$	48.0 ± 5.0	40; 40
ULAS J133943.79 +010436.4	T5 ± 0.5	−4.75 ± 0.07	SED	1280 ± 40	Evo−Age (7)	27	−4.750 ± 0.070	1253^{+52}_{-60}	$5.29^{+0.06}_{-0.17}$	$57.6^{+6.8}_{-13.4}$	27; 1
HD 19467B	T5.5 ± 1	…	…	978^{+20}_{-43}	Atm (30)	...	−5.205 ± 0.057	1006^{+34}_{-34}	$5.37^{+0.03}_{-0.06}$	$60.6^{+3.0}_{-5.5}$	1; 1
LHS 2803B	T5.5 ± 0.5	−5.06 ± 0.12	BC −SpT (15)	1120 ± 80	Evo−Age (2)	23	−5.215 ± 0.056	996^{+35}_{-35}	$5.36^{+0.05}_{-0.10}$	$59.1^{+4.2}_{-8.0}$	1; 1
WISE J072003.20 −084651.2B	T5.5 ± 0.5	−4.82 ± 0.07	BOL −IR (40)	1250 ± 40	Evo−Mass (11)	49	−4.820 ± 0.070	1250 ± 40	$5.39^{+0.03}_{-0.02}$	66.0 ± 4.0	49; 49
ϵ Indi Bb	T6 ± 0.5	−5.232 ± 0.020	SED	976−1011	Evo−Age (7)	14	−5.232 ± 0.020	963^{+12}_{-12}	$5.22^{+0.01}_{-0.02}$	$48.2^{+1.1}_{-1.1}$	14; 1
HIP 73786B	T6 ± 1 pec	…	…	…	…	...	−5.345 ± 0.058	910^{+40}_{-48}	$5.29^{+0.09}_{-0.24}$	$52.4^{+7.6}_{-16.1}$	1; 1
SDSS J175805.46 +463311.9	T6.5 ± 0.5	−5.18 ± 0.06	SED (13)	860−1030	Evo−Age (2)	13	−5.180 ± 0.060	944^{+42}_{-42}	$4.99^{+0.12}_{-0.19}$	$34.2^{+6.8}_{-9.0}$	13; 1
IR-Bright Old Benchmarks (>0.3 Gyr)											
NLTT 31450B	L6 ± 1	…	…	…	…	...	−4.009 ± 0.024	1853^{+23}_{-24}	$5.35^{+0.00}_{-0.01}$	$77.6^{+0.4}_{-1.1}$	1; 1

Table 4
(Continued)

Object	SpT	Literature					Adopted				
		log ($L_{bol}/L_{\odot}$) (dex)	L_{bol} Method[a]	T_{eff} (K)	T_{eff} Method[b]	References	log ($L_{bol}/L_{\odot}$) (dex)	T_{eff} (K)	log g (dex)	M (M_{Jup})	References[c] L_{bol}; Phys.
2MASS J00150206 +2959323	L7 ± 0.5	⋯	⋯	⋯	⋯	...	−4.138 ± 0.025	1741^{+23}_{-23}	$5.35^{+0.00}_{-0.00}$	$75.9^{+0.3}_{-0.4}$	1; 1
PM I 23492 + 3458B	L9 ± 0.5	⋯	⋯	⋯	⋯	...	−4.311 ± 0.024	1584^{+22}_{-26}	$5.36^{+0.00}_{-0.04}$	$73.6^{+0.4}_{-3.6}$	1; 1
SDSS J213154.43 −011939.3	L9 ± 1	$-4.4^{+0.1}_{-0.1}$	BC −SpT (34)	1400−1650	Evo−Age (5,17,21)	50	−4.319 ± 0.029	1580^{+25}_{-26}	$5.36^{+0.00}_{-0.02}$	$73.5^{+0.5}_{-1.7}$	1; 1
CFBDS J111807−064016	T2.5 ± 0.5	−4.80 ± 0.15	Evo−T_{eff} (6)	1300 ± 100	Atm (21,26)	32	−4.626 ± 0.051	1356^{+31}_{-29}	$5.37^{+0.01}_{-0.01}$	$70.1^{+0.7}_{-0.8}$	1; 1
HIP 70849B	T4.5 ± 0.5	⋯	⋯	⋯	⋯	...	$-4.673^{+0.074}_{-0.073}$	1304^{+53}_{-57}	$5.30^{+0.05}_{-0.16}$	$61.2^{+5.9}_{-13.9}$	1; 1
LSPM J1459+0857B	T4.5 ± 0.5	⋯	⋯	1200−1500	SpT (8)	19	−4.695 ± 0.055	1316^{+32}_{-31}	$5.38^{+0.01}_{-0.01}$	$68.9^{+1.0}_{-1.7}$	1; 1

Notes.

[a] "BC−SpT": L_{bol} is computed using parallax, near-infrared photometry, and a bolometric correction determined by the object's spectral type. "BOL−IR": L_{bol} is computed using the Dupuy & Liu (2017) relations between bolometric luminosities and near-infrared absolute magnitudes. "Evo−T_{eff}": L_{bol} is computed using evolutionary models and the effective temperatures determined from the atmospheric modeling. "SED": L_{bol} is computed using parallax and the bolometric flux defined by the object's spectra and multiband photometry. The references for bolometric corrections and evolutionary models are indicated by the numbers inside the parentheses.

[b] "Atm": T_{eff} is estimated from the object's near-infrared spectra using atmospheric models. "Evo−Age": T_{eff} is estimated from the object's ages and bolometric luminosities using evolutionary models. "Evo−Mass": T_{eff} is estimated by interpolating evolutionary models using dynamical mass and bolometric luminosity. "Radius": T_{eff} is estimated from bolometric luminosities based on assumptions of radius. "SpT": T_{eff} is estimated from spectral type using empirical effective temperature scales. The references for atmospheric models, evolutionary models, and effective temperature scales are indicated by the numbers inside the parentheses.

[c] Reference of our adopted L_{bol} values and physical properties (T_{eff}, log g, M). References for the different properties are separated by semicolons.

[d] The ages used in the literature to derive T_{eff} of these objects are now updated. We adopt an age of 149^{+51}_{-19} Myr (Bell et al. 2015) for the five AB Doradus members, 2MASS J2244316+204343 (assumed to be 110 −130 Myr in Faherty et al. 2016), WISE J004701.06+680352.1 (assumed to be ∼120 Myr in Gizis et al. 2015), 2MASS J22362452+4751425 b (assumed to be 120 ± 10 Myr in Bowler et al. 2017), GU Psc b and SDSSp J111010.01+011613.1 (both assumed to be 50−120 Myr in Filippazzo et al. 2015). We adopt an age of 24 ± 3 Myr (Bell et al. 2015) for the β Pictoris member, PSO J318.5338−22.8603 (assumed to be 12^{+8}_{-4} Myr in Liu et al. 2013). For Gl 584 C (assumed to be 0.5−10 Gyr in Filippazzo et al. 2015), we adopt an age of 1.0−2.5 Gyr based on the primary stars Gl 584 AB (Kirkpatrick et al. 2001).

References. (1) This work, (2) Burrows et al. (1997), (3) Baraffe et al. (1998), (4) Chabrier et al. (2000), (5) Allard et al. (2001), (6) Baraffe et al. (2003), (7) Baraffe et al. (2003), (8) Golimowski et al. (2004), (9) Vrba et al. (2004), (10) Luhman et al. (2007), (11) Saumon & Marley (2008), (12) Steele et al. (2009), (13) Faherty et al. (2010), (14) King et al. (2010), (15) Liu et al. (2010), (16) Marley et al. (2010), (17) Allard et al. (2011), (18) Barman et al. (2011), (19) Day-Jones et al. (2011), (20) Loutrel et al. (2011), (21) Allard et al. (2012), (22) Deacon et al. (2012a), (23) Deacon et al. (2012b), (24) Marley et al. (2012), (25) Morley et al. (2012), (26) Allard et al. (2013), (27) Burningham et al. (2013), (28) Bowler et al. (2013), (29) Liu et al. (2013), (30) Allard (2014), (31) Faherty et al. (2014), (32) Reylé et al. (2014), (33) Baraffe et al. (2015), (34) Filippazzo et al. (2015), (35) Gizis et al. (2015), (36) Gauza et al. (2015), (37) Faherty et al. (2016), (38) Bowler et al. (2017), (39) Chauvin et al. (2017), (40) Dupuy & Liu (2017), (41) Deacon et al. (2017), (42) Gagné et al. (2017), (43) Marley et al. (2017), (44) Miles-Páez et al. (2017), (45) Rajan et al. (2017), (46) Gagné et al. (2018), (47) Greenbaum et al. (2018), (48) Zapatero Osorio et al. (2018), (49) Dupuy et al. (2019), (50) Gauza et al. (2019).

using the Fortney et al. (2008) cold-start evolutionary models (also see Rajan et al. 2017), which assume objects are formed from core accretion with low initial entropy, whereas all of the aforementioned hot-start models assume that objects are formed with high initial entropy without any subsequent accretion. Finally, we note the young objects ($\leqslant$300 Myr) in our sample have $\log g = 3.5$–4.6 dex and $M = 2$–$20\ M_{\rm Jup}$, and the old ones (>300 Myr) have higher gravities and masses of $\log g = 4.8$–5.5 dex and $M = 25$–$80\ M_{\rm Jup}$.

6.1.2. Infrared-bright Old Benchmarks

Seven old companions (>300 Myr) in our sample have notably brighter ($\approx$0.3–1.0 mag) infrared absolute magnitudes than field dwarfs with similar spectral types. We checked that these companions' proper motions are consistent with the *Gaia* DR2 proper motions of their primary stars, so their companionship remains secure. Based on the literature, the spectra of these companions are mostly normal when compared to spectral standards, except for 2MASS J00150206+2959323 (2MASS J0015+2959; Deacon et al. 2014). This object has a peculiar near-infrared spectrum (L7.5 pec; Kirkpatrick et al. 2010) with a blue $J_{\rm MKO} - K_{\rm MKO} = 1.58 \pm 0.07$ mag, about 0.4 mag bluer than typical field L7 dwarfs (e.g., Best et al. 2020, in preparation). However, this object's *JHK*-band absolute magnitudes are all significantly brighter than other field dwarfs, suggesting its blue color is not the only peculiarity.

Among these seven infrared-bright objects, SDSS J213154.43−011939.3 (SDSS J2131−0119) is an L9 companion to a $0\farcs64$ M3+M6 binary NLTT 51469AB at a projected separation of $82''$ recently found by Gauza et al. (2019). They noted the *Gaia* DR2 parallactic distance (46.6 ± 1.3 pc) and the spectrophotometric distance (34^{+10}_{-13} pc) of the primary stellar binary are only marginally consistent. One explanation is that the *Gaia* DR2 astrometry of the primary might be affected by the orbital motion of the binary, as it is unresolved by *Gaia* (also see Dupuy et al. 2018). Gauza et al. also noted the *Gaia* DR2 astrometry of NLTT 51469AB possess an astrometric excess noise of 2.74 mas with a very high significance (2202σ) and was determined from only eight independent groups of *Gaia* observations (i.e., visibility_periods_used = 8), whereas a larger number (e.g., $\geqslant$10) would result in more reliable astrometry (Lindegren et al. 2018). We find that NLTT 51469 AB has a very large RUWE of 12, indicating that the *Gaia* DR2 astrometry of the primary cannot be well-explained by a single-star model. In addition, the spectrophotometric distance of the L9 companion SDSS J2131−0119 is $\approx 40 \pm 11$ pc, consistent with both parallactic and spectrophotometric distance of the primary star, making the true distance of this comoving system unclear. If we adopt the spectrophotometric distance of the primary, then the companion's near-infrared absolute magnitudes are consistent with field L9 dwarfs.

We find that the primary stars of the remaining six infrared-bright companions all have consistent *Gaia* DR2 parallactic distances and spectrophotometric distances, both of which are farther than the companions' spectrophotometric distances, suggesting that these companions are either unresolved binaries/multiples associated with their primary stars or foreground interlopers. High-precision parallaxes for both companions and primary stars in all seven systems are therefore needed to verify if they are located at the same distance and thus physically associated. Also, high spatial-resolution imaging would be helpful to examine the binarity of these L/T dwarfs. In our subsequent analysis, we simply adopt the primary stars' *Gaia* DR2 distances for these seven objects.

6.2. Discussion

We investigate the photometric and physical properties of L/T benchmarks with different ages (surface gravities) in Figures 14–16. As is well known, going from L6 to L9 spectral types, young benchmark objects ($\leqslant$300 Myr) become gradually fainter in *JHK* absolute magnitudes and redder in $J_{\rm MKO} - K_{\rm MKO}$ (by 0.5–1.0 mag) than old objects (>300 Myr), constituting a natural photometric extension of earlier-type young moving group members and low-gravity field dwarfs (e.g., Faherty et al. 2016; Liu et al. 2016). The difference in near-infrared absolute magnitudes of the four young L7.5–L9 dwarfs (2MASS 2236 b, HD 203030 B, VHS 1256 b, and HR 8799 b) compared to the old benchmarks of same spectral types (excluding infrared-bright old benchmarks discussed in Section 6.1.2) is a function of wavelengths, as has been already noted (e.g., Faherty et al. 2013, 2016; Liu et al. 2016). Compared to field objects, the absolute magnitudes of young L7.5–L9 dwarfs are fainter by 0.8–2.0 mag in $J_{\rm MKO}$, and such magnitude difference between young and old populations decreases to 0.3–1.5 mag in $H_{\rm MKO}$, and finally become indistinguishable or only slight of $\lesssim$1.0 mag in $K_{\rm MKO}$, suggesting that condensate clouds alter the SEDs of young, low-gravity late-L dwarfs more significantly than old, high-gravity objects (e.g., Marley et al. 2012; Marocco et al. 2013; Hiranaka et al. 2016).

Excluding the four HR 8799 planets, we find that the bolometric luminosities of young L6−L9 dwarfs (Figure 16) are consistent with or only slightly fainter (by <0.1 dex) than old objects (e.g., Filippazzo et al. 2015; Faherty et al. 2016). While HR 8799 bcde have fainter $L_{\rm bol}$ by $\approx$0.3–0.5 dex than their older counterparts, their spectral types are only loosely determined (e.g., Bowler et al. 2010; Greenbaum et al. 2018), and thus, their positions in Figure 16 might be shifted horizontally to be more or less consistent with the old population. In addition, young L6–L9 dwarfs span a wide range in effective temperatures (mostly 1100–1300 K, with the HR 8799 b of $\approx$950 K), significantly cooler than old objects (1300–1600 K) with similar spectral types, and comparable to the temperatures of old T0–T6 dwarfs. This reinforces that the L/T transition occurs at much cooler temperatures at low surface gravities (e.g., Metchev & Hillenbrand 2006; Luhman et al. 2007; Dupuy et al. 2009; Barman et al. 2011; Marley et al. 2012; Bowler et al. 2013; Liu et al. 2013; Gagné et al. 2018).

Young T0–T5 dwarfs still possess redder $J_{\rm MKO} - K_{\rm MKO}$ colors (by 0.2–0.5 mag) than old objects, but their near-infrared absolute magnitudes are more similar to old objects than is the case for the late-L types. Compared to field objects, the five young T2–T5 dwarfs (2MASS J13243553+6358281, HN Peg B, SIMP J013656.5+093347.3, GU Psc b, and SDSS J111010.01+011613.1) have fainter absolute magnitudes by $\lesssim$0.5 mag in $J_{\rm MKO}$ and $\lesssim$0.2 mag in $H_{\rm MKO}$, and similar magnitudes in $K_{\rm MKO}$, indicating that the redder $J - K$ colors of young T dwarfs are largely due to their fainter *J*-band absolute magnitudes. Therefore, our sample suggests that infrared absolute magnitudes of low-gravity dwarfs are only slightly fainter than (if not consistent with) high-gravity dwarfs for T0–T5 spectral types (or equivalently with $J_{\rm MKO} - K_{\rm MKO}$

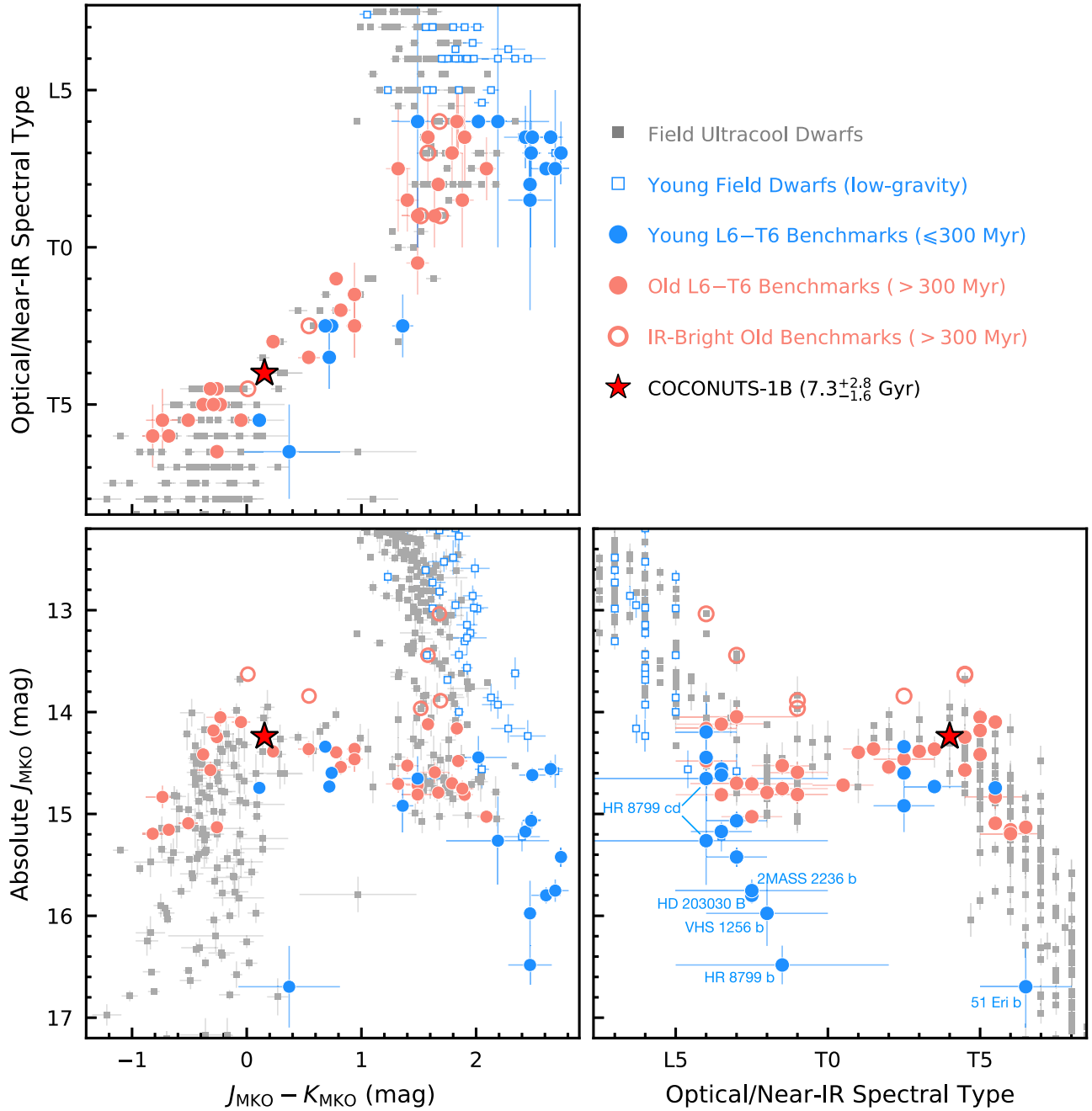

Figure 14. Infrared properties of L/T transition benchmarks, including our newly discovered high-gravity T4 companion COCONUTS-1B (red), young L6−T6 objects with ages ≲300 Myr (blue solid circles), seven infrared-bright old benchmarks (orange open circles; Section 6.1.2), and the normal old benchmarks (>300 Myr; orange solid circles). We use gray squares to show known field dwarfs (W. M. J. Best et al. 2020, in preparation) that have infrared absolute magnitudes with S/N > 5 and are not young, binaries, or subdwarfs. We use blue open squares to show young moving group members or low-gravity field dwarfs. The upper left and lower right panels show the objects' absolute J_{MKO} magnitudes and $J_{MKO} - K_{MKO}$ colors as a function of spectral type, and the lower left panel displays the corresponding color–magnitude diagram. We do not show error bars for spectral types if they are smaller than one subtype. Young L6−T6 objects have fainter infrared absolute magnitudes and redder colors than their older counterparts, although such differences between the two populations appear greater for late-L dwarfs than for early-/mid-T dwarfs. In addition, young objects become brighter in the J band by ≈1.5 mag as they evolve from late-L to T types, significantly larger than the ≈0.5 mag J-band brightening seen in field L/T objects (Dupuy & Liu 2012).

from 1.5 to −0.5 mag). This behavior is the opposite of that in the Saumon & Marley (2008) hybrid evolutionary models, which predict young early-T dwarfs to be brighter than old objects. The Marley et al. (2012) evolutionary models added a gravity dependence in the L/T transition to their group's models when analyzing the HR 8799 planets and suggested that the K-band absolute magnitudes become fainter toward lower surface gravities. However, our sample finds such a K-band magnitude difference is very subtle between young and old objects. In addition, we note that the color–magnitude diagram locus of young and old T dwarfs is mostly similar or differs only slightly different (as suggested by Liu et al. 2016 with a smaller sample of objects), again in contrast to the Marley et al. (2012) models.

Unlike late-L dwarfs, bolometric luminosities of young T0–T5 benchmarks are more similar to the old benchmarks and

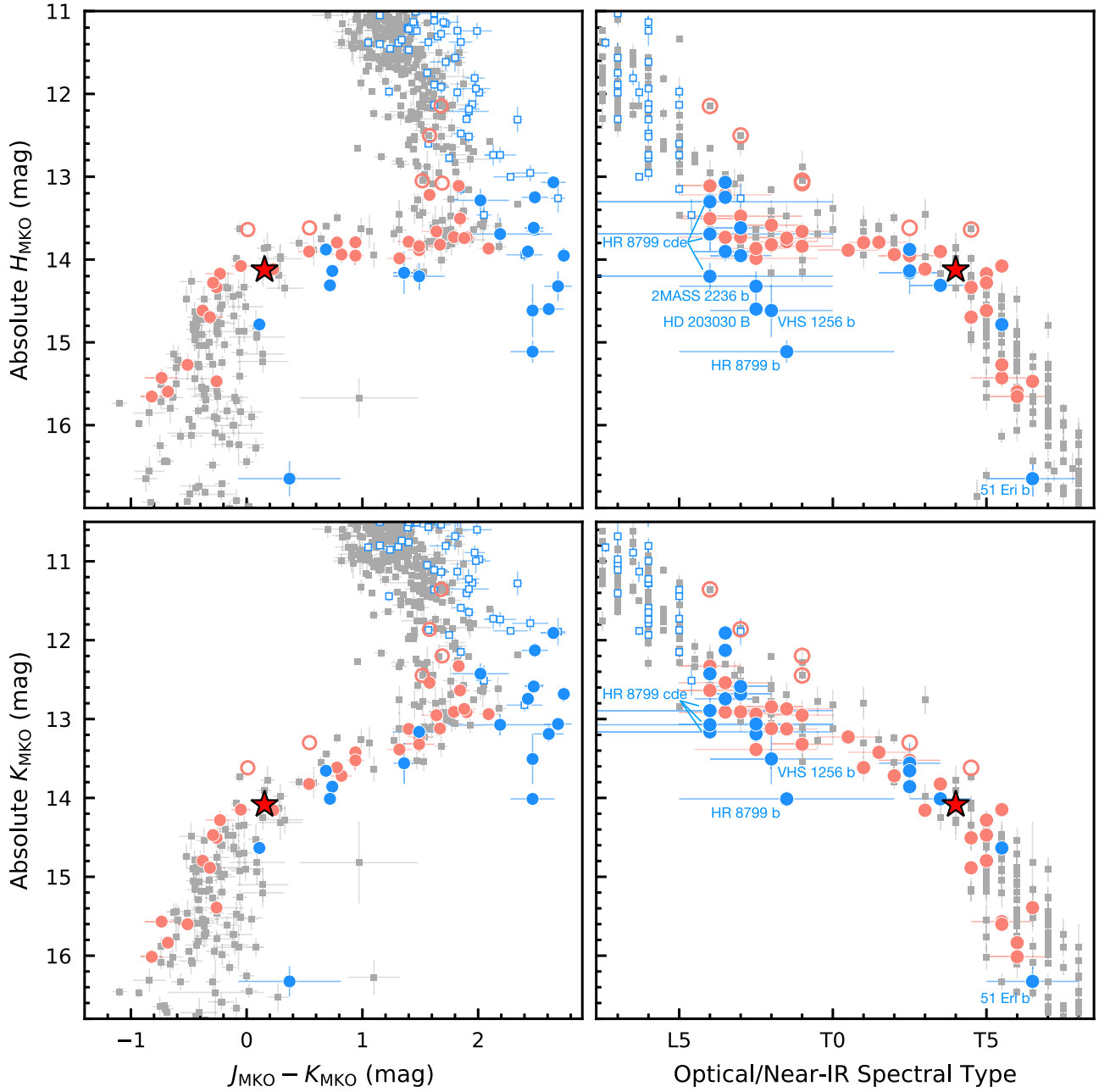

Figure 15. Same format as Figure 14 but with absolute H_{MKO} and K_{MKO} magnitudes. Combined with Figure 14, these figures show that the difference in infrared absolute magnitudes between young and old populations is a function of wavelength, being most pronounced in the *J* band and decreasing for the *H* and *K* bands. In addition, young objects show the ≈0.6 mag *H*-band brightening as they evolve from late-L to T types, and the evolution in the *K*-band photometry between young and old L/T dwarfs is nearly identical as a function of spectral type.

field population[16] (Figure 16). As a consequence, effective temperatures of young objects are cooler by ≈100 K than old objects, given that their radii are still in the process of contraction (e.g., Burrows et al. 2001). In comparison, COCONUTS-1B has contracted to a very small radii (0.79 R_{Jup}; Table 2) given its very old age of $7.3^{+2.8}_{-1.6}$ Gyr, thereby resulting in a relatively high temperature for its spectral type.

In addition, field dwarfs are known to exhibit the *J*-band brightening phenomenon, as their *J*-band absolute magnitudes become brighter by ≈0.5 mag when they evolve from late-L to mid-T types, and then resume with fainter absolute magnitudes for later spectral types (e.g., Dahn et al. 2002; Tinney et al. 2003; Vrba et al. 2004; Liu et al. 2006; Dupuy & Liu 2012). No such brightening is clearly seen at the *H* and *K* bands for field objects. The phenomenon is likely a hallmark of cloud

[16] In Figure 16, we compare bolometric luminosities of our L/T benchmarks with the field-age dwarfs in Filippazzo et al. (2015), who also provided a polynomial describing the L_{bol} versus SpT relation for field dwarfs. We note that the precision of the polynomial coefficients reported in their Table 10 produces an offset between their sample and the constructed polynomial. Such offset is insignificant in L types, but the polynomial is systematically brighter compared to the data by 0.05 dex at T0, 0.15 dex at T5, and 0.33 dex at T9. We have therefore used the same data from Filippazzo et al. (2015) and performed a sixth-order polynomial fit for M6–T9, namely $L_{bol} = \sum_{i=0}^{n=6} c_i\,(\mathrm{SpT})^i$, where SpT = 6 for M6, = 10 for L0, etc. Our coefficients are $c_0 = 1.355808e+01$, $c_1 = -6.988722e+00$, $c_2 = 1.173746e+00$, $c_3 = -1.013430e-01$, $c_4 = 4.653312e-03$, $c_5 = -1.077500e-04$, $c_6 = 9.858614e-07$, with a rms of 0.137 dex. The round-off error from our coefficients is 0.001 dex.

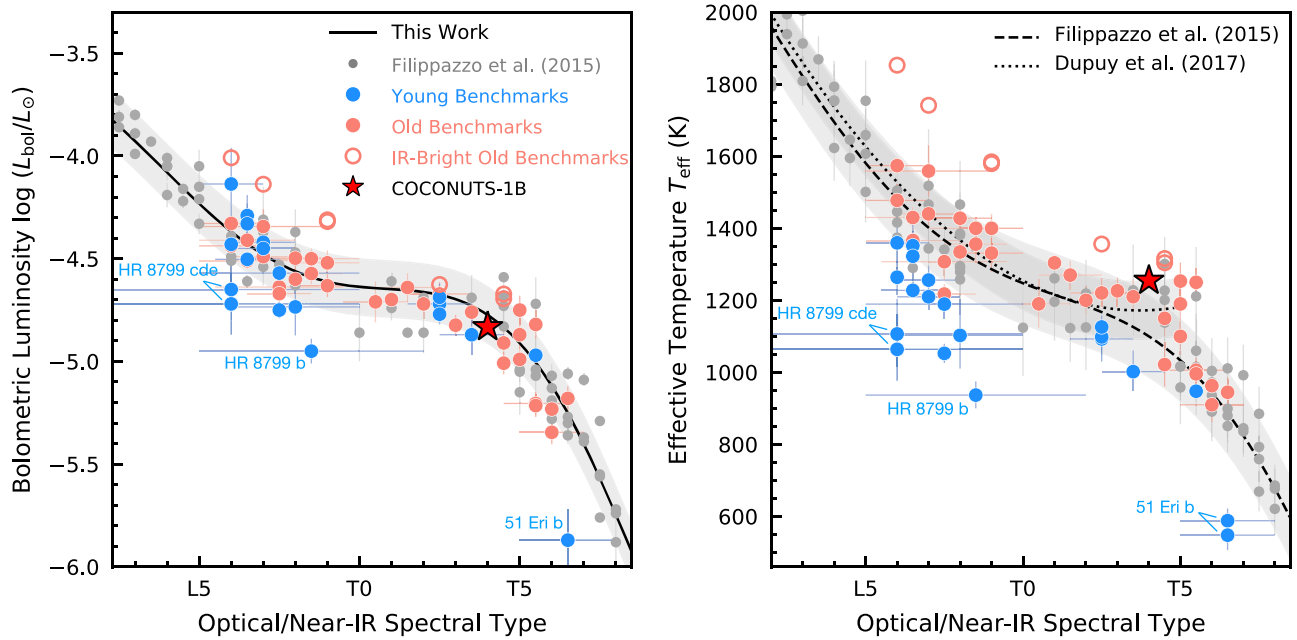

Figure 16. Bolometric luminosities and effective temperatures of our sample, overlaid with field dwarfs (gray circles) from Filippazzo et al. (2015). In the left panel, we also overlay the polynomial of the L_{bol} vs. SpT relation derived in this work, using the Filippazzo et al. (2015) sample (see our footnote 16 for details), and in the right panel, we show the polynomial relation from both Filippazzo et al. (2015) and Dupuy & Liu (2017). While luminosities of young objects are consistent with or only slightly fainter than the old objects at same spectral types, the former has cooler temperatures across the entire L/T transition, reinforcing that the L/T transition is gravity dependent. The young benchmark sample is very sparse near T0, primarily because of their rarity (e.g., Day-Jones et al. 2013; Marocco et al. 2015).

evolution in the L/T transition, with the dominant opacity source in 1.0–1.3 μm region being condensate opacity rather than gas opacity (e.g., Ackerman & Marley 2001; Burrows et al. 2006). Our benchmark sample shows that for young objects, the *J*-band brightening has a significantly larger amplitude ($\approx$1.5 mag) than the $\approx$0.5 mag seen in the old population. Moreover, young objects appear to also undergo a $\approx$1 mag brightening in the *H* band as they evolve through the L/T transition. This longer wavelength brightening is broadly consistent with the notion that the atmospheres of young L dwarfs have a lower sedimentation efficiency (e.g., Marley et al. 2012; see also Figure 22 of Liu et al. 2016), leading to a more vertically extended cloud (which apparently can influence the flux in both the *J*- and *H*-band molecular opacity windows) as well as smaller particle sizes (which leads to an increase in condensate opacity for a given mass of condensates). Systematic modeling of cloud opacity evolution will be required to tease out such effects.

As an alternative modeling approach for ultracool atmospheres, Tremblin et al. (2016) have proposed the thermal-chemical instability to explain the spectrophotometric evolution of brown dwarfs across the L/T transition (also the T/Y transition; Tremblin et al. 2015) without invoking condensate clouds. For late-L dwarfs, such instability triggers local compositional convection that drives the abundance of CO and CH_4 out of chemical equilibrium and reduces the temperature gradient in the atmosphere, leading to the objects' observed fainter and redder near-infrared photometry. For early-T dwarfs, such CO/CH_4-related instability dissipates, warming up the deep layers of the atmosphere and leading to the observed *J*-band brightening phenomenon. The Tremblin et al. models have been tested to reproduce properties of several L/T dwarfs of different temperatures and gravities (e.g., Tremblin et al. 2016, 2017). These models should be further tested to account for the gravity-dependent *J*-band brightening and the *H*-band brightening of young objects as seen from our sample of L6–T6 benchmarks.

In summary, we find that the *K*-band absolute magnitudes and L_{bol} among different ages are nearly identical as a function of spectral type, but the effective temperatures of young L/T dwarfs are notably cooler than in old dwarfs. The difference in the *J*- and *H*-band absolute magnitudes between young ($\leqslant$300 Myr) and old (>300 Myr) populations changes from being substantial in late-L dwarfs to being nearly negligible in early-T dwarfs, indicating that the magnitude of the gravity dependence becomes weaker with later spectral types across the L/T transition. Finally, the brightening of near-infrared magnitudes across the transition is larger in both amplitude and wavelength range for young objects as compared to old ones.

7. Summary

We have reported the first discovery from our COol Companions ON Ultrawide orbiTS (COCONUTS) program, a large-scale survey for wide-orbit planetary and substellar companions within 100 pc. We have discovered the comoving system COCONUTS-1, which is located at 31.51 pc and composed of a DA white dwarf primary and a T4 companion with a projected separation of 41″ (1280 au). Our photometric analysis of the white dwarf suggests that it has a cool effective temperature (5115 K) and low mass (0.548 $M_\odot$). Combining the white dwarf cooling age with its progenitor's main-sequence lifetime, we estimate the system's age as $7.3^{+2.8}_{-1.6}$ Gyr.

The multiwavelength photometry and near-infrared spectrum of COCONUTS-1B both support its common distance with the white dwarf. We estimate an extremely low contamination probability by field interlopers, further supporting the physical association between the T dwarf and the white dwarf.

We fit the cloudless Sonora atmospheric models to the near-infrared spectrum of COCONUTS-1B to study its physical

Table 5
Directly Imaged L, T, Y Companions to White Dwarfs

Companion					White Dwarf Primary			
Companion Name	Other Name	Spectral Type	Projected Separation (″)	Discovery References	Spectral Type	*Gaia* DR2 Distance (pc)	Estimated Age (Gyr)	Age References
LSPM J0241+2553B	2MASS J02415153+2553452	L1	31.2	(1)	…[a]	72.7 ± 1.0	<10[b]	(1)
GD 165B	2MASS J14243909+0917104	L4	4	(2)	DA	33.41 ± 0.06	1.2−5.5	(3)
PHL 5038B	SDSS J222030.68-004107.3B	L8	0.94	(4)	DA	72.9 ± 1.2	1.9−2.7	(4)
COCONUTS-1B	PSO J058.9869+45.4296	T4	40.61	This Work	DA	31.51 ± 0.09	$7.3^{+2.8}_{-1.6}$	This Work
LSPM J1459+0857B	ULAS J145935.25+085751.2	T4.5	385	(5)	DA	72.5 ± 1.8	>4.8	(5)
Wolf 1130C[c]	WISE J200520.38+542433.9	T8	188.5	(6)	…[a]	16.559 ± 0.009	>10[d]	(7)
WD 0806-661B	L 97−3B	Y1[e]	130.2	(8)	DQ	19.255 ± 0.007	2 ± 0.5	(9)

Notes. The estimated ages of white dwarfs are derived from the cooling age and the evolutionary time of their progenitors unless otherwise noted.
[a] Deacon et al. (2014) and Mace et al. (2018) did not have spectra of the white dwarf primary for LSPM J0241+2553B and Wolf 1130C, respectively.
[b] The maximum age of the white dwarf is estimated based on its disk-like kinematics.
[c] This companion is in a multiple system with the primary being a binary composed of an M3 subdwarf and a white dwarf (Gizis 1998).
[d] The white dwarf age is estimated using the metallicity and kinematics of the M3 subdwarf Wolf 1130A, which forms a binary with the white dwarf Wolf 1130B. The white dwarf is not detected in 0.2−2.5 μm, providing an age constraint as >3.4 Gyr (Mace et al. 2018).
[e] The companion's spectral type is assigned by Leggett et al. (2015) based on photometry.
References. (1) Deacon et al. (2014), (2) Becklin & Zuckerman (1988), (3) Kirkpatrick et al. (1999), (4) Steele et al. (2009), (5) Day-Jones et al. (2011), (6) Mace et al. (2013), (7) Mace et al. (2018), (8) Luhman et al. (2011), (9) Luhman et al. (2012).

properties. The best-fit Sonora model spectra generally match the observed spectrum but mismatch occurs at the blue wing of the *Y* band, which is sensitive to the potassium abundance and the pressure-broadened red wing of the potassium doublet. We note that mismatches near the peaks of the *J* and *H* bands suggest a deep cloud deck in the atmospheres, which is not included in our set of model atmospheres.

We also use the cloudless Sonora evolutionary models to estimate the companion's physical properties, based on the companion's bolometric luminosity and the system's age from the white dwarf. Both the atmospheric and evolutionary models predict consistent effective temperatures and radii, but the atmospheric models imply a much smaller surface gravity and, thus, a very young age of ≈380 Myr, in contradiction to the age of the white dwarf. The unphysically young age of the brown dwarf companion reflects shortcomings of the cloudless model atmospheres. We therefore adopt the evolutionary model parameters as the characteristics of the companion. The companion's $\log g$ from the evolutionary models ($5.44^{+0.02}_{-0.03}$ dex) is among the highest surface gravity that brown dwarfs can reach over the cosmic time.

In order to understand the shortcomings of the cloudless atmospheric models, we interpolate the model spectra at the $\{T_{\rm eff}, \log g\}$ values derived from the evolutionary models. The resulting model atmospheres have a relatively bluer near-infrared color and more emergent flux in the *Y* and *J* bands as compared to the observed spectrum. Adding silicate clouds or adopting different potassium line profiles into the model atmospheres may help to relieve the discrepancies. We also note that the observed *W*2-band flux of COCONUTS-1B is fainter than that of the model spectra, which might be explained by the non-equilibrium abundances of CO.

For planetary and substellar benchmarks, white dwarf primaries can provide among the most precise ages for companions. Thus far, only a handful binaries composed of white dwarfs and resolved substellar companions have been found, and COCONUTS-1 is among the oldest in this sample (Table 5), thereby probing the high surface-gravity regime of the L/T transition.

In order to better understand the gravity dependence in the L/T transition, we have compiled all 60 known L6–T6 benchmarks, including members of nearby associations, companions to stars or white dwarfs, and substellar binary components. Many of these benchmarks now have precise parallaxes thanks to *Gaia* DR2. We have also (re-)computed bolometric luminosities, effective temperatures, surface gravities, and masses for most of these L/T benchmarks for a more uniform comparison.

We find that infrared photometry of young (⩽300 Myr) late-L dwarfs is significantly fainter (by 0.8–2.0 mag in *J*-band absolute magnitude) and redder (by 0.5–1.0 mag in $J-K$) than that of their older (>300 Myr) counterparts, as has already been well-noted (e.g., Faherty et al. 2016; Liu et al. 2016). Also, young late-L's have consistent or only slightly fainter bolometric luminosities than old objects, with their effective temperatures ≈200–300 K cooler than the latter at same spectral types.

Our large benchmark sample shows that the gravity dependence appears weaker for T dwarfs. While young T0–T5 benchmarks still possess redder $J-K$ colors (by 0.2–0.5 mag) than old objects, their near-infrared absolute magnitudes are more similar to field objects, especially in the *H* and *K* bands, than is the case for the late-L dwarfs. The redder $J-K$ colors of young T dwarfs are largely due to their fainter *J*-band absolute magnitudes. The observed behavior is the opposite of the Saumon & Marley (2008) hybrid evolutionary models, which predict young early-T dwarfs to be brighter than old objects. The Marley et al. (2012) evolutionary models with a gravity-dependent L/T transition suggest that *K*-band absolute magnitudes become notably fainter toward lower surface gravities, but our sample finds that such a *K*-band magnitude difference is subtle between young and old objects. In addition, bolometric luminosities of young T dwarfs agree well with the old population, resulting in cooler effective temperatures (by ≈100 K) given that they are still in process of contraction.

In summary, our sample shows that ultracool dwarfs with different ages have vastly different photometric properties in late-L dwarfs but similar near-infrared absolute magnitudes and

bolometric luminosities as they evolve to early-T dwarfs. Notably, our sample reveals that young L/T objects exhibit the *J*-band brightening phenomenon with a significantly larger amplitude (≈1.5 mag) as compared to the ≈0.5 mag brightening seen in field L/T objects (e.g., Dupuy & Liu 2012), and also extending to the *H* band in the young objects.

Finally, we note that more discoveries of young T0–T1 benchmarks would bridge the observed properties of late-L and T dwarfs, establishing a more comprehensive understanding of the L/T evolution. These objects are very rare, so deep imaging surveys like UHS and VHS exploring a larger volume in the solar neighborhood would be very helpful. Also, a uniform spectroscopic analysis of planetary-mass and substellar benchmarks will help us to better understand the wavelength ranges where atmospheric models cannot explain the data. Such work will provide useful suggestions to improve contemporary model atmospheres.

We thank the anonymous referee for helpful comments. We thank Didier Saumon, Caroline Morley, Paul Mollière, William Best, and Jennifer van Saders for insightful discussions and comments. We thank Ian Czekala for discussions about the Starfish package, and thank Michael Gully-Santiago for implementing Starfish for IRTF/SpeX prism data. We thank Michael Cushing for discussions about the IRTF/SpeX wavelength calibration and thank Trent Dupuy for discussions about the Hawaii Infrared Parallax Program. This work benefited from the Exoplanet Summer Program in the Other Worlds Laboratory (OWL) at the University of California, Santa Cruz, a program funded by the Heising-Simons Foundation. M.C.L. acknowledges National Science Foundation (NSF) grant AST-1518339. M.A.T. acknowledges support from the DOE CSGF through grant DE-SC0019323. The advanced computing resources from the University of Hawaii Information Technology Services—Cyberinfrastructure and the technical support from Curt Dodds are gratefully acknowledged. This work presents results from the European Space Agency (ESA) space mission *Gaia*. *Gaia* data are being processed by the *Gaia* Data Processing and Analysis Consortium (DPAC). Funding for the DPAC is provided by national institutions, in particular the institutions participating in the *Gaia* MultiLateral Agreement (MLA). The *Gaia* mission website is https://www.cosmos.esa.int/gaia. The *Gaia* archive website is https://archives.esac.esa.int/gaia. The Pan-STARRS1 Surveys (PS1) have been made possible through contributions of the Institute for Astronomy, the University of Hawaii, the Pan-STARRS Project Office, the Max-Planck Society and its participating institutes, the Max Planck Institute for Astronomy, Heidelberg and the Max Planck Institute for Extraterrestrial Physics, Garching, The Johns Hopkins University, Durham University, the University of Edinburgh, Queen's University Belfast, the Harvard-Smithsonian Center for Astrophysics, the Las Cumbres Observatory Global Telescope Network Incorporated, the National Central University of Taiwan, the Space Telescope Science Institute, the National Aeronautics and Space Administration under grant No. NNX08AR22G issued through the Planetary Science Division of the NASA Science Mission Directorate, the National Science Foundation under grant No. AST-1238877, the University of Maryland, and Eotvos Lorand University (ELTE). This publication makes use of data products from the Two Micron All Sky Survey, which is a joint project of the University of Massachusetts and the Infrared Processing and Analysis Center/California Institute of Technology, funded by the National Aeronautics and Space Administration and the National Science Foundation. This work is based in part on data obtained as part of the UKIRT Infrared Deep Sky Survey. The UHS is a partnership between the UK STFC, The University of Hawaii, The University of Arizona, Lockheed Martin and NASA. This publication makes use of data products from the *Wide-field Infrared Survey Explorer*, which is a joint project of the University of California, Los Angeles, and the Jet Propulsion Laboratory/California Institute of Technology, and NEOWISE, which is a project of the Jet Propulsion Laboratory/California Institute of Technology. *WISE* and NEOWISE are funded by the National Aeronautics and Space Administration. This research has made use of the SIMBAD database and the VizieR catalog access tool developed and operated at CDS, Strasbourg, France. This work was greatly facilitated by the TOPCAT software written by Mark Taylor (http://www.starlink.ac.uk/topcat/). Finally, the authors wish to recognize and acknowledge the very significant cultural role and reverence that the summit of Maunakea has always had within the indigenous Hawaiian community. We are most fortunate to have the opportunity to conduct observations from this mountain.

Facilities: UH 2.2 m (SNIFS), IRTF (SpeX), Pan-STARRS, 2MASS, UKIRT, *WISE*.

Software: emcee (Foreman-Mackey et al. 2013), Starfish (Czekala et al. 2015), TOPCAT (Taylor 2005), Spextool (v4.1; Cushing et al. 2004), Astropy (Astropy Collaboration et al. 2013, 2018), IPython (Pérez & Granger 2007), Numpy (Oliphant 2006), Scipy (Jones et al. 2001), Matplotlib (Hunter 2007).

ORCID iDs

Zhoujian Zhang (张周健) https://orcid.org/0000-0002-3726-4881
Michael C. Liu https://orcid.org/0000-0003-2232-7664
Eugene A. Magnier https://orcid.org/0000-0002-7965-2815
Mark S. Marley https://orcid.org/0000-0002-5251-2943
Pier-Emmanuel Tremblay https://orcid.org/0000-0001-9873-0121
Michael A. Tucker https://orcid.org/0000-0002-2471-8442
Aaron Do https://orcid.org/0000-0003-3429-7845
Benjamin J. Shappee https://orcid.org/0000-0003-4631-1149

References

Abt, H. A. 2009, ApJS, 180, 117
Abt, H. A., & Morrell, N. I. 1995, ApJS, 99, 135
Ackerman, A. S., & Marley, M. S. 2001, ApJ, 556, 872
Albert, L., Artigau, É, Delorme, P., et al. 2011, AJ, 141, 203
Aldering, G., Adam, G., Antilogus, P., et al. 2002, Proc. SPIE, 4836, 61
Allard, F. 2014, in IAU Symp. 299, Exploring the Formation and Evolution of Planetary Systems, ed. M. Booth, B. C. Matthews, & J. R. Graham, 271
Allard, F., Allard, N. F., Homeier, D., et al. 2007a, A&A, 474, L21
Allard, F., Hauschildt, P. H., Alexander, D. R., Tamanai, A., & Schweitzer, A. 2001, ApJ, 556, 357
Allard, F., Homeier, D., & Freytag, B. 2011, in ASP Conf. Ser. 448, Model Atmospheres From Very Low Mass Stars to Brown Dwarfs, ed. C. Johns-Krull, M. K. Browning, & A. A. West (San Francisco, CA: ASP), 91
Allard, F., Homeier, D., & Freytag, B. 2012, RSPTA, 370, 2765
Allard, F., Homeier, D., Freytag, B., et al. 2013, MSAIS, 24, 128
Allard, N. F., Spiegelman, F., & Kielkopf, J. F. 2007b, A&A, 465, 1085
Allard, N. F., Spiegelman, F., & Kielkopf, J. F. 2016, A&A, 589, A21
Allers, K. N., & Liu, M. C. 2013, ApJ, 772, 79

Alonso-Floriano, F. J., Morales, J. C., Caballero, J. A., et al. 2015, A&A, 577, A128
Anderson, E., & Francis, C. 2012, AstL, 38, 331
Artigau, É, Doyon, R., Lafrenière, D., et al. 2006, ApJL, 651, L57
Astropy Collaboration, Price-Whelan, A. M., Sipőcz, B. M., et al. 2018, AJ, 156, 123
Astropy Collaboration, Robitaille, T. P., Tollerud, E. J., et al. 2013, A&A, 558, A33
Bacon, R., Copin, Y., Monnet, G., et al. 2001, MNRAS, 326, 23
Bailer-Jones, C. A. L., Rybizki, J., Fouesneau, M., Mantelet, G., & Andrae, R. 2018, AJ, 156, 58
Baraffe, I., Chabrier, G., Allard, F., & Hauschildt, P. H. 1998, A&A, 337, 403
Baraffe, I., Chabrier, G., Barman, T. S., Allard, F., & Hauschildt, P. H. 2003, A&A, 402, 701
Baraffe, I., Homeier, D., Allard, F., & Chabrier, G. 2015, A&A, 577, A42
Barman, T. S., Macintosh, B., Konopacky, Q. M., & Marois, C. 2011, ApJ, 733, 65
Barnaby, D., Spillar, E., Christou, J. C., & Drummond, J. D. 2000, AJ, 119, 378
Barnes, J. W., & Fortney, J. J. 2003, ApJ, 588, 545
Barnes, S. A. 2007, ApJ, 669, 1167
Becklin, E. E., & Zuckerman, B. 1988, Natur, 336, 656
Bédard, A., Bergeron, P., & Fontaine, G. 2017, ApJ, 848, 11
Bell, C. P. M., Mamajek, E. E., & Naylor, T. 2015, MNRAS, 454, 593
Bergeron, P., Dufour, P., Fontaine, G., et al. 2019, ApJ, 876, 67
Bergeron, P., Ruiz, M. T., & Leggett, S. K. 1997, ApJS, 108, 339
Bergeron, P., Saffer, R. A., & Liebert, J. 1992, ApJ, 394, 228
Bergeron, P., Wesemael, F., Lamontagne, R., et al. 1995, ApJ, 449, 258
Best, W. M. J. 2018, PhD thesis, Univ. Hawai'i at Manoa
Best, W. M. J., Liu, M. C., Magnier, E. A., et al. 2015, ApJ, 814, 118
Best, W. M. J., Magnier, E. A., Liu, M. C., et al. 2018, ApJS, 234, 1
Biller, B. A., Vos, J., Bonavita, M., et al. 2015, ApJL, 813, L23
Blouin, S., Dufour, P., Thibeault, C., & Allard, N. F. 2019, ApJ, 878, 63
Bouvier, J., Kendall, T., Meeus, G., et al. 2008, A&A, 481, 661
Bowler, B. P. 2016, PASP, 128, 102001
Bowler, B. P., Liu, M. C., Dupuy, T. J., & Cushing, M. C. 2010, ApJ, 723, 850
Bowler, B. P., Liu, M. C., Mawet, D., et al. 2017, AJ, 153, 18
Bowler, B. P., Liu, M. C., Shkolnik, E. L., & Dupuy, T. J. 2013, ApJ, 774, 55
Brandt, T. D., & Huang, C. X. 2015, ApJ, 807, 24
Brandt, T. D., McElwain, M. W., Turner, E. L., et al. 2014, ApJ, 794, 159
Burgasser, A. J. 2007, ApJ, 659, 655
Burgasser, A. J., Cruz, K. L., Cushing, M., et al. 2010, ApJ, 710, 1142
Burgasser, A. J., Geballe, T. R., Leggett, S. K., Kirkpatrick, J. D., & Golimowski, D. A. 2006a, ApJ, 637, 1067
Burgasser, A. J., Kirkpatrick, J. D., Brown, M. E., et al. 2002, ApJ, 564, 421
Burgasser, A. J., Kirkpatrick, J. D., Cruz, K. L., et al. 2006b, ApJS, 166, 585
Burgasser, A. J., Kirkpatrick, J. D., Cutri, R. M., et al. 2000, ApJL, 531, L57
Burgasser, A. J., Kirkpatrick, J. D., & Lowrance, P. J. 2005a, AJ, 129, 2849
Burgasser, A. J., Kirkpatrick, J. D., Reid, I. N., et al. 2003, ApJ, 586, 512
Burgasser, A. J., Melis, C., Todd, J., et al. 2015, AJ, 150, 180
Burgasser, A. J., Reid, I. N., Leggett, S. K., et al. 2005b, ApJL, 634, L177
Burgasser, A. J., Sheppard, S. S., & Luhman, K. L. 2013, ApJ, 772, 129
Burningham, B., Cardoso, C. V., Smith, L., et al. 2013, MNRAS, 433, 457
Burningham, B., Pinfield, D. J., Lucas, P. W., et al. 2010, MNRAS, 406, 1885
Burrows, A., Hubbard, W. B., Lunine, J. I., & Liebert, J. 2001, RvMP, 73, 719
Burrows, A., & Liebert, J. 1993, RvMP, 65, 301
Burrows, A., Marley, M., Hubbard, W. B., et al. 1997, ApJ, 491, 856
Burrows, A., Marley, M. S., & Sharp, C. M. 2000, ApJ, 531, 438
Burrows, A., Sudarsky, D., & Hubeny, I. 2006, ApJ, 640, 1063
Burrows, A., & Volobuyev, M. 2003, ApJ, 583, 985
Casagrande, L., Schönrich, R., Asplund, M., et al. 2011, A&A, 530, A138
Casewell, S. L., Dobbie, P. D., Napiwotzki, R., et al. 2009, MNRAS, 395, 1795
Chabrier, G., Baraffe, I., Allard, F., & Hauschildt, P. 2000, ApJ, 542, 464
Chambers, K. C., Magnier, E. A., Metcalfe, N., et al. 2016, arXiv:1612.05560
Chandrasekhar, S. 1939, An Introduction to the Study of Stellar Structure (Chicago, IL: Univ. Chicago Press)
Chaplin, W. J., & Miglio, A. 2013, ARA&A, 51, 353
Chauvin, G., Desidera, S., Lagrange, A. M., et al. 2017, A&A, 605, L9
Chiu, K., Fan, X., Leggett, S. K., et al. 2006, AJ, 131, 2722
Choi, J., Dotter, A., Conroy, C., et al. 2016, ApJ, 823, 102
Ciddor, P. E. 1996, ApOpt, 35, 1566
Cottaar, M., Covey, K. R., Meyer, M. R., et al. 2014, ApJ, 794, 125
Crepp, J. R., Johnson, J. A., Howard, A. W., et al. 2014, ApJ, 781, 29
Crepp, J. R., Rice, E. L., Veicht, A., et al. 2015, ApJL, 798, L43
Cruz, K. L., Reid, I. N., Kirkpatrick, J. D., et al. 2007, AJ, 133, 439
Cushing, M. C., Vacca, W. D., & Rayner, J. T. 2004, PASP, 116, 362
Cutri, R. M., Skrutskie, M. F., van Dyk, S., et al. 2003, yCat, 2246, 0
Cutri, R. M., et al. 2014, yCat, 2328, 0
Czekala, I., Andrews, S. M., Mandel, K. S., Hogg, D. W., & Green, G. M. 2015, ApJ, 812, 128
Dahm, S. E. 2015, ApJ, 813, 108
Dahn, C. C., Harris, H. C., Vrba, F. J., et al. 2002, AJ, 124, 1170
Day-Jones, A. C., Marocco, F., Pinfield, D. J., et al. 2013, MNRAS, 430, 1171
Day-Jones, A. C., Pinfield, D. J., Ruiz, M. T., et al. 2011, MNRAS, 410, 705
Deacon, N. R., Liu, M. C., Magnier, E. A., et al. 2012a, ApJ, 755, 94
Deacon, N. R., Liu, M. C., Magnier, E. A., et al. 2012b, ApJ, 757, 100
Deacon, N. R., Liu, M. C., Magnier, E. A., et al. 2014, ApJ, 792, 119
Deacon, N. R., Magnier, E. A., Liu, M. C., et al. 2017, MNRAS, 467, 1126
Desidera, S., & Barbieri, M. 2007, A&A, 462, 345
Dhital, S., Burgasser, A. J., Looper, D. L., & Stassun, K. G. 2011, AJ, 141, 7
Dupuy, T. J., & Liu, M. C. 2012, ApJS, 201, 19
Dupuy, T. J., & Liu, M. C. 2017, ApJS, 231, 15
Dupuy, T. J., Liu, M. C., Allers, K. N., et al. 2018, AJ, 156, 57
Dupuy, T. J., Liu, M. C., Best, W. M. J., et al. 2019, AJ, 158, 174
Dupuy, T. J., Liu, M. C., & Ireland, M. J. 2009, ApJ, 699, 168
Dupuy, T. J., Liu, M. C., Leggett, S. K., et al. 2015, ApJ, 805, 56
Dye, S., Lawrence, A., Read, M. A., et al. 2018, MNRAS, 473, 5113
Edge, A., Sutherland, W. & Viking Team 2016, yCat, 2343, 0
Edwards, T. W. 1976, AJ, 81, 245
Eisenstein, D. J., Liebert, J., Harris, H. C., et al. 2006, ApJS, 167, 40
Emerson, J. P., Sutherland, W. J., McPherson, A. M., et al. 2004, Msngr, 117, 27
Evans, D. W., Riello, M., De Angeli, F., et al. 2018, A&A, 616, A4
Faherty, J. K., Beletsky, Y., Burgasser, A. J., et al. 2014, ApJ, 790, 90
Faherty, J. K., Burgasser, A. J., Walter, F. M., et al. 2012, ApJ, 752, 56
Faherty, J. K., Burgasser, A. J., West, A. A., et al. 2010, AJ, 139, 176
Faherty, J. K., Rice, E. L., Cruz, K. L., Mamajek, E. E., & Núñez, A. 2013, AJ, 145, 2
Faherty, J. K., Riedel, A. R., Cruz, K. L., et al. 2016, ApJS, 225, 10
Feigelson, E. D., Lawson, W. A., Stark, M., Townsley, L., & Garmire, G. P. 2006, AJ, 131, 1730
Fields, C. E., Farmer, R., Petermann, I., Iliadis, C., & Timmes, F. X. 2016, ApJ, 823, 46
Filippazzo, J. C., Rice, E. L., Faherty, J., et al. 2015, ApJ, 810, 158
Fontaine, G., Brassard, P., & Bergeron, P. 2001, PASP, 113, 409
Foreman-Mackey, D., Hogg, D. W., Lang, D., & Goodman, J. 2013, PASP, 125, 306
Fortney, J. J., Marley, M. S., Saumon, D., & Lodders, K. 2008, ApJ, 683, 1104
Gagné, J., Allers, K. N., Theissen, C. A., et al. 2018, ApJL, 854, L27
Gagné, J., Burgasser, A. J., Faherty, J. K., et al. 2015, ApJL, 808, L20
Gagné, J., Faherty, J. K., Burgasser, A. J., et al. 2017, ApJL, 841, L1
Gaia Collaboration, Brown, A. G. A., Vallenari, A., et al. 2018, A&A, 616, A1
Gaia Collaboration, Prusti, T., de Bruijne, J. H. J., et al. 2016, A&A, 595, A1
Garcia, E. V., Ammons, S. M., Salama, M., et al. 2017, ApJ, 846, 97
Gauza, B., Béjar, V. J. S., Pérez-Garrido, A., et al. 2015, ApJ, 804, 96
Gauza, B., Béjar, V. J. S., Pérez-Garrido, A., et al. 2019, MNRAS, 487, 1149
Geballe, T. R., Knapp, G. R., Leggett, S. K., et al. 2002, ApJ, 564, 466
Gentile Fusillo, N. P., Tremblay, P.-E., Gänsicke, B. T., et al. 2019, MNRAS, 482, 4570
Giammichele, N., Bergeron, P., & Dufour, P. 2012, ApJS, 199, 29
Gizis, J. E. 1998, AJ, 115, 2053
Gizis, J. E., Allers, K. N., Liu, M. C., et al. 2015, ApJ, 799, 203
Gizis, J. E., Faherty, J. K., Liu, M. C., et al. 2012, AJ, 144, 94
Gizis, J. E., Reid, I. N., Knapp, G. R., et al. 2003, AJ, 125, 3302
Golimowski, D. A., Leggett, S. K., Marley, M. S., et al. 2004, AJ, 127, 3516
González-Fernández, C., Hodgkin, S. T., Irwin, M. J., et al. 2018, MNRAS, 474, 5459
Goodman, J., & Weare, J. 2010, CAMCS, 5, 65
Gray, R. O., Corbally, C. J., Garrison, R. F., et al. 2006, AJ, 132, 161
Gray, R. O., Corbally, C. J., Garrison, R. F., McFadden, M. T., & Robinson, P. E. 2003, AJ, 126, 2048
Gray, R. O., Napier, M. G., & Winkler, L. I. 2001, AJ, 121, 2148
Greenbaum, A. Z., Pueyo, L., Ruffio, J.-B., et al. 2018, AJ, 155, 226
Hewett, P. C., Warren, S. J., Leggett, S. K., & Hodgkin, S. T. 2006, MNRAS, 367, 454
Hiranaka, K., Cruz, K. L., Douglas, S. T., Marley, M. S., & Baldassare, V. F. 2016, ApJ, 830, 96
Hollands, M. A., Tremblay, P. E., Gänsicke, B. T., Gentile-Fusillo, N. P., & Toonen, S. 2018, MNRAS, 480, 3942

Houk, N. 1978, Michigan Catalog of Two-dimensional Spectral Types for the HD Stars (Ann Arbor, MI: Univ. Michigan)
Houk, N., & Smith-Moore, M. 1988, Michigan Catalogue of Two-dimensional Spectral Types for the HD Stars, Vol. 4 (Ann Arbor, MI: Univ. Michigan)
Houk, N., & Swift, C. 1999, Michigan Spectral Survey, Vol. 5 (Ann Arbor, MI: Univ. Michigan), 0
Hunter, J. D. 2007, CSE, 9, 90
James, R. A. 1964, ApJ, 140, 552
Janson, M., Bergfors, C., Brandner, W., et al. 2014, ApJS, 214, 17
Janson, M., Hormuth, F., Bergfors, C., et al. 2012, ApJ, 754, 44
Jarrett, T. H., Cohen, M., Masci, F., et al. 2011, ApJ, 735, 112
Jaschek, M. 1978, BICDS, 15, 121
Jeffries, R. D., & Stevens, I. R. 1996, MNRAS, 279, 180
Jones, E., Oliphant, T., Peterson, P., et al. 2001, SciPy: Open Source Scientific Tools for Python, http://www.scipy.org/
Kalirai, J. S., Hansen, B. M. S., Kelson, D. D., et al. 2008, ApJ, 676, 594
Karovska, M., Hack, W., Raymond, J., & Guinan, E. 1997, ApJL, 482, L175
Kendall, T. R., Delfosse, X., Martín, E. L., & Forveille, T. 2004, A&A, 416, L17
King, R. R., McCaughrean, M. J., Homeier, D., et al. 2010, A&A, 510, A99
Kirkpatrick, J. D. 2005, ARA&A, 43, 195
Kirkpatrick, J. D., Allard, F., Bida, T., et al. 1999, ApJ, 519, 834
Kirkpatrick, J. D., Cruz, K. L., Barman, T. S., et al. 2008, ApJ, 689, 1295
Kirkpatrick, J. D., Dahn, C. C., Monet, D. G., et al. 2001, AJ, 121, 3235
Kirkpatrick, J. D., Looper, D. L., Burgasser, A. J., et al. 2010, ApJS, 190, 100
Kirkpatrick, J. D., Reid, I. N., Liebert, J., et al. 2000, AJ, 120, 447
Knapp, G. R., Leggett, S. K., Fan, X., et al. 2004, AJ, 127, 3553
Koen, C., Kilkenny, D., van Wyk, F., & Marang, F. 2010, MNRAS, 403, 1949
Lagrange, A. M., Beust, H., Udry, S., Chauvin, G., & Mayor, M. 2006, A&A, 459, 955
Lantz, B., Aldering, G., Antilogus, P., et al. 2004, Proc. SPIE, 5249, 146
Lawrence, A., Warren, S. J., Almaini, O., et al. 2007, MNRAS, 379, 1599
Lawrence, A., Warren, S. J., Almaini, O., et al. 2012, yCat, 2314, 0
Leggett, S. K., Morley, C. V., Marley, M. S., & Saumon, D. 2015, ApJ, 799, 37
Liebert, J., Bergeron, P., & Holberg, J. B. 2005, ApJS, 156, 47
Lindegren, L. 2018, Gaia Technical Note: GAIA-C3-TN-LU-LL-124-01, https://www.cosmos.esa.int/web/gaia/public-dpac-documents
Lindegren, L., Hernández, J., Bombrun, A., et al. 2018, A&A, 616, A2
Liu, M. C., Dupuy, T. J., & Allers, K. N. 2016, ApJ, 833, 96
Liu, M. C., Dupuy, T. J., & Ireland, M. J. 2008, ApJ, 689, 436
Liu, M. C., Dupuy, T. J., & Leggett, S. K. 2010, ApJ, 722, 311
Liu, M. C., Leggett, S. K., & Chiu, K. 2007, ApJ, 660, 1507
Liu, M. C., Leggett, S. K., Golimowski, D. A., et al. 2006, ApJ, 647, 1393
Liu, M. C., Magnier, E. A., Deacon, N. R., et al. 2013, ApJL, 777, L20
Lodieu, N., Pérez-Garrido, A., Béjar, V. J. S., et al. 2014, A&A, 569, A120
Looper, D. L., Gelino, C. R., Burgasser, A. J., & Kirkpatrick, J. D. 2008a, ApJ, 685, 1183
Looper, D. L., Kirkpatrick, J. D., & Burgasser, A. J. 2007, AJ, 134, 1162
Looper, D. L., Kirkpatrick, J. D., Cutri, R. M., et al. 2008b, ApJ, 686, 528
Loutrel, N. P., Luhman, K. L., Lowrance, P. J., & Bochanski, J. J. 2011, ApJ, 739, 81
Luhman, K. L. 2013, ApJL, 767, L1
Luhman, K. L., Burgasser, A. J., & Bochanski, J. J. 2011, ApJL, 730, L9
Luhman, K. L., Burgasser, A. J., Labbé, I., et al. 2012, ApJ, 744, 135
Luhman, K. L., Patten, B. M., Marengo, M., et al. 2007, ApJ, 654, 570
Mace, G. N., Kirkpatrick, J. D., Cushing, M. C., et al. 2013, ApJ, 777, 36
Mace, G. N., Mann, A. W., Skiff, B. A., et al. 2018, ApJ, 854, 145
Macintosh, B., Graham, J. R., Barman, T., et al. 2015, Sci, 350, 64
Magnier, E. A., & Cuillandre, J.-C. 2004, PASP, 116, 449
Magnier, E. A., Schlafly, E. F., Finkbeiner, D. P., et al. 2016, arXiv:1612.05242
Marley, M. S., Ackerman, A. S., Cuzzi, J. N., & Kitzmann, D. 2013, in Clouds and Hazes in Exoplanet Atmospheres, ed. S. J. Mackwell et al. (Tucson, AZ: Univ. Arizona Press), 367
Marley, M. S., & Robinson, T. D. 2015, ARA&A, 53, 279
Marley, M. S., Saumon, D., Cushing, M., et al. 2012, ApJ, 754, 135
Marley, M. S., Saumon, D., Fortney, J. J., et al. 2017, AAS Meeting, 230, 315.07
Marley, M. S., Saumon, D., & Goldblatt, C. 2010, ApJL, 723, L117
Marley, M. S., Seager, S., Saumon, D., et al. 2002, ApJ, 568, 335
Marley, M. S., & Sengupta, S. 2011, MNRAS, 417, 2874
Marocco, F., Andrei, A. H., Smart, R. L., et al. 2013, AJ, 146, 161
Marocco, F., Jones, H. R. A., Day-Jones, A. C., et al. 2015, MNRAS, 449, 3651
Marois, C., Macintosh, B., Barman, T., et al. 2008, Sci, 322, 1348
Marois, C., Zuckerman, B., Konopacky, Q. M., Macintosh, B., & Barman, T. 2010, Natur, 468, 1080
Mason, B. D. 1996, AJ, 112, 2260
Matthews, C. T., Crepp, J. R., Skemer, A., et al. 2014, ApJL, 783, L25
McCaughrean, M. J., Close, L. M., Scholz, R. D., et al. 2004, A&A, 413, 1029
McMahon, R. G., Banerji, M., Gonzalez, E., et al. 2013, Msngr, 154, 35
Melis, C., Reid, M. J., Mioduszewski, A. J., Stauffer, J. R., & Bower, G. C. 2014, Sci, 345, 1029
Metchev, S. A., & Hillenbrand, L. A. 2006, ApJ, 651, 1166
Miles-Páez, P. A., Metchev, S., Luhman, K. L., Marengo, M., & Hulsebus, A. 2017, AJ, 154, 262
Minniti, D., Lucas, P. W., Emerson, J. P., et al. 2010, NewA, 15, 433
Morley, C. V., Fortney, J. J., Marley, M. S., et al. 2012, ApJ, 756, 172
Murray, D. N., Burningham, B., Jones, H. R. A., et al. 2011, MNRAS, 414, 575
Naud, M.-E., Artigau, É, Malo, L., et al. 2014, ApJ, 787, 5
Nielsen, E. L., De Rosa, R. J., Macintosh, B., et al. 2019, AJ, 158, 44
Oliphant, T. 2006, NumPy: A Guide to NumPy (Trelgol Publishing), http://www.numpy.org/
Pérez, F., & Granger, B. E. 2007, CSE, 9, 21
Pinfield, D. J., Jones, H. R. A., Lucas, P. W., et al. 2006, MNRAS, 368, 1281
Press, W. H., Teukolsky, S. A., Vetterling, W. T., & Flannery, B. P. 1992, Numerical Recipes in FORTRAN. The Art of Scientific Computing (Cambridge: Cambridge Univ. Press)
Rajan, A., Rameau, J., De Rosa, R. J., et al. 2017, AJ, 154, 10
Rayner, J. T., Toomey, D. W., Onaka, P. M., et al. 2003, PASP, 115, 362
Reid, I. N., Cruz, K. L., Kirkpatrick, J. D., et al. 2008, AJ, 136, 1290
Reid, I. N., Lewitus, E., Allen, P. R., Cruz, K. L., & Burgasser, A. J. 2006a, AJ, 132, 891
Reid, I. N., Lewitus, E., Burgasser, A. J., & Cruz, K. L. 2006b, ApJ, 639, 1114
Reid, I. N., & Walkowicz, L. M. 2006, PASP, 118, 671
Reylé, C., Delorme, P., Artigau, E., et al. 2014, A&A, 561, A66
Reylé, C., Delorme, P., Willott, C. J., et al. 2010, A&A, 522, A112
Riaz, B., Gizis, J. E., & Harvin, J. 2006, AJ, 132, 866
Richichi, A., Ragland, S., Calamai, G., Richter, S., & Stecklum, B. 2000, A&A, 361, 594
Sahlmann, J., & Lazorenko, P. F. 2015, MNRAS, 453, L103
Salaris, M., Serenelli, A., Weiss, A., & Miller Bertolami, M. 2009, ApJ, 692, 1013
Samland, M., Mollière, P., Bonnefoy, M., et al. 2017, A&A, 603, A57
Saumon, D., & Marley, M. S. 2008, ApJ, 689, 1327
Saumon, D., Marley, M. S., Cushing, M. C., et al. 2006, ApJ, 647, 552
Scholz, R.-D. 2010, A&A, 515, A92
Scholz, R. D. 2014, A&A, 561, A113
Scholz, R. D., McCaughrean, M. J., Lodieu, N., & Kuhlbrodt, B. 2003, A&A, 398, L29
Ségransan, D., Mayor, M., Udry, S., et al. 2011, A&A, 535, A54
Shkolnik, E., Liu, M. C., & Reid, I. N. 2009, ApJ, 699, 649
Siegler, N., Close, L. M., Burgasser, A. J., et al. 2007, AJ, 133, 2320
Skrutskie, M. F., Cutri, R. M., Stiening, R., et al. 2006, AJ, 131, 1163
Smith, L. C., Lucas, P. W., Kurtev, R., et al. 2018, MNRAS, 474, 1826
Steele, P. R., Burleigh, M. R., Farihi, J., et al. 2009, A&A, 500, 1207
Stephens, D. C., Leggett, S. K., Cushing, M. C., et al. 2009, ApJ, 702, 154
Stone, J. M., Skemer, A. J., Kratter, K. M., et al. 2016, ApJL, 818, L12
Struve, O., & Franklin, K. L. 1955, ApJ, 121, 337
Sutherland, W., Emerson, J., Dalton, G., et al. 2015, A&A, 575, A25
Taylor, M. B. 2005, in ASP Conf. Ser. 347, TOPCAT & STIL: Starlink Table/VOTable Processing Software, ed. P. Shopbell, M. Britton, & R. Ebert (San Francisco, CA: ASP), 29
Tinney, C. G., Burgasser, A. J., & Kirkpatrick, J. D. 2003, AJ, 126, 975
Tonry, J. L., Stubbs, C. W., Lykke, K. R., et al. 2012, ApJ, 750, 99
Torres, C. A. O., Quast, G. R., da Silva, L., et al. 2006, A&A, 460, 695
Tremblay, P. E., Bergeron, P., & Gianninas, A. 2011, ApJ, 730, 128
Tremblin, P., Amundsen, D. S., Chabrier, G., et al. 2016, ApJL, 817, L19
Tremblin, P., Amundsen, D. S., Mourier, P., et al. 2015, ApJL, 804, L17
Tremblin, P., Chabrier, G., Baraffe, I., et al. 2017, ApJ, 850, 46
Tsuji, T., Ohnaka, K., & Aoki, W. 1999, ApJL, 520, L119
Valenti, J. A., & Fischer, D. A. 2005, ApJS, 159, 141
van Leeuwen, F. 2007, A&A, 474, 653
Vos, J. M., Biller, B. A., Bonavita, M., et al. 2019, MNRAS, 483, 480
Vrba, F. J., Henden, A. A., Luginbuhl, C. B., et al. 2004, AJ, 127, 2948
Williams, K. A., Bolte, M., & Koester, D. 2009, ApJ, 693, 355
Wilson, J. C., Kirkpatrick, J. D., Gizis, J. E., et al. 2001, AJ, 122, 1989

Wright, E. L., Eisenhardt, P. R. M., Mainzer, A. K., et al. 2010, AJ, 140, 1868
Zahnle, K. J., & Marley, M. S. 2014, ApJ, 797, 41
Zapatero Osorio, M. R., Béjar, V. J. S., Lodieu, N., & Manjavacas, E. 2018, MNRAS, 475, 139
Zapatero Osorio, M. R., Gálvez Ortiz, M. C., Bihain, G., et al. 2014, A&A, 568, A77
Zuckerman, B., Bessell, M. S., Song, I., & Kim, S. 2006, ApJL, 649, L115
Zuckerman, B., Rhee, J. H., Song, I., & Bessell, M. S. 2011, ApJ, 732, 61
Zuckerman, B., Song, I., Bessell, M. S., & Webb, R. A. 2001, ApJL, 562, L87
Zurlo, A., Vigan, A., Hagelberg, J., et al. 2013, A&A, 554, A21